Alma Mater Studiorum - Università di Bologna

DOTTORATO DI RICERCA IN

INGEGNERIA CIVILE, CHIMICA, AMBIENTALE E DEI MATERIALI

Ciclo 34

Settore Concorsuale: 08/B2 - SCIENZA DELLE COSTRUZIONI

Settore Scientifico Disciplinare: ICAR/08 - SCIENZA DELLE COSTRUZIONI

THE AERODYNAMIC BEHAVIOR OF POROUS ELEMENTS IN EXTERNAL FLOWS: MODELING APPROACHES IN COMPUTATIONAL FLUID DYNAMICS BASED SIMULATIONS

Presentata da: Mao Xu

Coordinatore Dottorato

Alessandro Tugnoli

Supervisore

Stefano de Miranda

Co-supervisore

Luca Patruno

Esame finale anno 2022

First and foremost, I would like to thank Prof. Stefano de Miranda and Prof. Luca Patruno for their invaluable advice and patience during these years.

I would also like to express my gratitude to Prof. Yuan-lung Lo, from the National Taipei University of Technology, who provides great help for my researches.

At this point, I want to thank all my workmates in DICAM: Prof. Francesco Ubertini, Marija Bervida, Jin Xing, Weilin Li, Giorgio Cortelli, Antonio Maria D'Altri, Giovanni Castellazzi, Gregorio Bertani, Xingbo Pu, Farhad Zeighami, and Chiara Brighenti. Thank you for all your supports during these years.

Last but not least, sincerely thanks to everyone who has fought with the COVID-19.

Abstract

In the last decades, porous surfaces became increasingly popular in modern architecture due to their aesthetic value, the possibility to be used in energy efficient cladding solutions and their ability to maintain ventilation. From the aerodynamic point of view, porous structures can be fruitfully used in order to decrease wind loads compared to fully solid ones, especially with respect to vortex shedding. Additionally, porous elements are commonly found as secondary structures (e.g. wind shields) on bridge decks to protect traffic against strong cross wind.

Nevertheless, due to the remarkable length scale separation existing between the overall structure and the pores, usually in the range of two or three orders of magnitude, it is extremely difficult to study structures presenting porous surfaces in wind tunnel tests. In particular, the installation of the pressure taps and the piping system including pressure scanners is challenging in many situations. Additionally, due to these difficulties, only a small number of pressure taps can be well arranged, while pressures must be scanned on both sides of the surface. This inevitably leads to poor sampling of the pressure field so that measurements using balances are usually preferred, although the obtained information is restricted to global forces.

Computational Fluid Dynamics (CFD) has been rapidly expanding in the last decades for Wind Engineering applications and might provide substantial benefits in the study of porous structures. In fact, it completely eliminates all problems related to the installation of measurement systems and allows to provide very fine space sampling of the obtained results.

However, when the geometry of porous surfaces is explicitly modeled, computations rapidly become intractable due to the large number of cells required to represent the pores. This leads to prohibitive computational costs in the majority of the cases. An alternative approach is to model the presence of porous surfaces by means of appropriate homogenized models and ignore the flow details, being the usually adopted one so-called pressure-jump approach. When pressure jumps are adopted, two main hypotheses are introduced. Firstly, pores are of vanishing size, so that details of the flow in their surroundings do not affect the overall flow. Secondly, only the forces normal to porous barrier are accounted for. This means that shearing effects due to the presence of the barrier are disregarded. Currently, this modeling approach has been fairly validated for internal aerodynamics (e.g. flows through porous filters), which generally provides good results, but it is not widely validated for external aerodynamics problems.

Within this framework, this thesis focuses on the use of pressure jumps for external aerodynamics problems. For this purpose, firstly, the flow through porous grid was analyzed in detail and a new model able to predict the pressure jumps based on porosity was derived. Then, the proposed model was preliminary assessed by comparing itself with several simulated and experimental results.

To further evaluate the performance of pressure-jump approach in CFD-based simulation, the results obtained using explicit and pressure-jump models of the porous surfaces geometry were compared considering cases of increasing complexity, namely a forward facing step, an hollow porous 5:1 rectangular cylinder, bridge decks with wind shields and a ground mounted porous prism exposed to both smooth and turbulent flow. For all cases, a systematic comparison was carried out between the two aforementioned modeling strategies. Moreover, to identify the potential influences on its accuracy, mesh resolutions, turbulence models, surface thickness, pore shapes and size were respectively investigated for most cases.

Results show that the overall external flow arrangement of these two modeling strategies are usually found to be in good agreement, at least in the limits of the proposed investigations. This agreement is possible to be affected by numerous factors, in which the pore arrangement is remarkable, especially when only a few pores are studied. Moreover, taking the few available experimental results as a reference, the accuracy of these modeling strategies for the porous cases appears to be lower than that for fully solid cases, but overall trends are respected. In summary, considering the convenience given by the adoption of homogenized models and the scarce influence from this simplification, the use of pressure-jump approach is a viable solution.

Contents

Chapter 1

Introduction

1.1 Motivation

Over the years, porous surfaces have been increasingly adopted in modern architecture (see for instance [1, 2, 3]), which is mainly because of several coexisting properties. In particular, porous surfaces allow to provide spatial separation while keeping ventilation. Additionally, they provide protection against sunlight, allow for innovative energy-efficient cladding solutions and reduce wind loads. Important application of porous elements are also routinely found in wind shields positioned on bridge decks in order to protect vehicular traffic against cross-winds. However, compared to completely solid structures, the aerodynamic behavior of porous ones received relatively little attention from the scientific community. Consequently, the aerodynamic behavior of structures partially or entirely composed of porous surfaces currently represents a problem of growing technical interest.

Several theoretical and experimental researches regarding porous surface have been reported for both internal flows (the porous surface located in a confined flow field) and external flows (the porous surface located in a open flow field). In these studies, a wide range of aerodynamic problems were discussed, e.g. the wind loading ([4, 5, 6, 7], ESDU item 72009 and 80025), characteristics of wake flow [8, 9, 10, 11, 12] and turbulence generating [13]. A systematic review of the literatures is reported in Section 1.2. Surely, it can be concluded that in all the considered applications, the presence of small-scale porosity introduces peculiar features to the flow field that render arduous its simulation with reduced-scale physical models, as well computational simulations.

In particular, the usual experimental strategy for completely solid structure, for which the pressure field is characterized by means of pressure taps on the external side of the considered geometry, is hard to be performed for scaled porous surfaces. The interference of the piping system on the flow fields is difficult to be avoided, because the diameter of such pipes might be similar or even larger than that of the pores. Additionally, allocating the numerous pipes usually necessary to connect the taps to the pressure scanners becomes often impossible when the building interior is part of the flow field. This can be sometimes avoided by embedding the piping system in the reduced-scale model walls (see Fig. 1.1), but such solution is impractical and severely limits the number of pressure taps which can be installed. Moreover, for porous surfaces, pressure shall be measured on both sides so doubling the number of pressure probes which need to be installed, which together with previous comments, make the installation of pressure taps subastantially impossible in many circumstances. Moreover, if the pores are irregularly distributed on the porous surface, the physical meaning of the measured pressure needs to be carefully assessed, because it might not represent the effective pressure which globally acts on the surface. In particular, for the pressure difference measured as the difference between the two sides of porous surface, the obtained value might not be easily related to the integral forces acting on the surface as a whole.

(a) (b)

Figure 1.1: A scaled model of building façades [14] composed of porous surfaces and its piping system for pressure measurement.

In such context, Computational Fluid Dynamics (CFD) might represent an approach able to overcome the aforementioned difficulties. The possibility of obtaining flow characteristics without installing physical measuring equipment avoids its interaction with the flow. With the continuous increment of available computing power [15], the popularity of numerical simulations is continuously growing in wind engineering and porous surfaces have been analyzed, for instance, in [16, 17, 18, 19, 20, 21, 22, 23]. In particular, the comparison between experimental and computational results often indicates good performances of numerical simulations when the main intent is to represent the interaction between the porous surface and the fluid in terms of its resistance to the flow [24, 25, 26]. The details of the numerical techniques (Finite Volume Method) and models adopted in this thesis are well-known. The reader can refer to [27, 28, 29, 30] for additional information and details.

Due to the fact that the pore size is usually much smaller than the whole structure, numerical simulations based on the explicit geometrical modeling of the pores require a huge number of cells, which consequently leads to extremely high computational costs. Figure 1.2 provides a pictorial example of the difficulties found in obtaining an adequate mesh for the study of bodies composed by porous surfaces, even in an extremely simple case. As it can be noticed, the mesh is probably adequate for providing a good resolution of the flow field if the structure was solid. However, each pore is only roughly meshed and the pore thickness is model by only one cell, thus, the results are hard to be independent from mesh resolution.

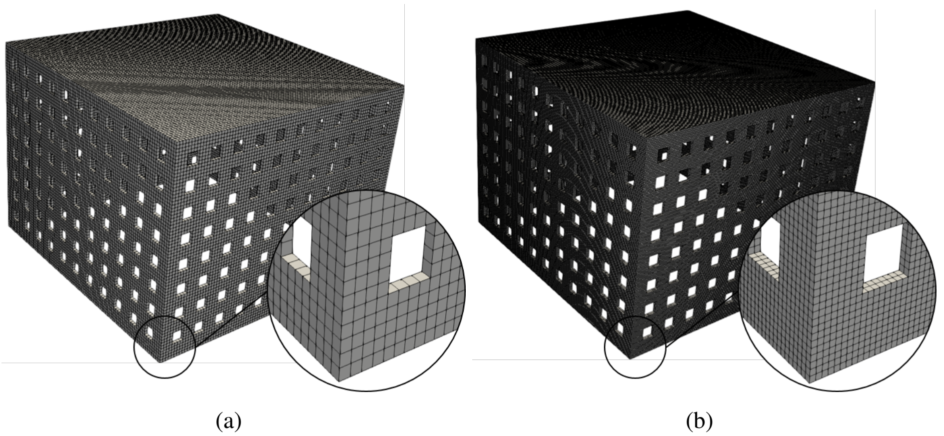
(a) (b)

Figure 1.2: The mesh of porous surfaces when (a): coarse mesh resolution and (b): finer mesh resolution are adopted.

For reducing the computational costs, a well-known and convenient alternative to the explicit modeling of the pores geometry is to model the presence of the porous surface by means of appropriate pressure jumps (Δp) [31, 32, 33]. In such context, the modeling effort on pores and computational resource for simulating the bleed flows can be saved. A rigorous approach to the subject would require to frame it in the theory of asymptotic homogenization [34]. In essence, the presence of the pores induces variations in the flow field characterized by small space and time scales which can be averaged out, so allowing to study the flow behavior at the macro-scale by providing a simplified model of its behavior at the micro-scale.

Currently, such a modeling approach is fairly validated for internal aerodynamics (e.g. flows trough porous filters), but it is not widely validated for external aerodynamics problems. Considering the remarkable convenience of using pressure jumps, a deep assessment of their accuracy appears to be necessary application in the engineering practice.

1.2 State of the art and open problems

To the best knowledge of the author, the resistance of porous surfaces to the air flow has been initially studied considering the flow through screens in confined flow fields (see Fig. 1.3 [35]). For example, a quantitative relation is derived to link the screen porosity to the pressure jump measured on the two sides of the screen, or equivalently to the drag force acting on the screen, was derived by [36]. Previous studies investigated numerous parameters which might affect such pressure difference, such as the Reynolds number, fluid compressibility and pores arrangement. For instance, the effect of the Reynolds number and the incidence of the incoming flow with respect to the screen normal has been considered in the seminal paper by [37], which proposes a relation between the surface porosity, the Reynolds number, the incidence angle and the measured pressure jump. In this case, also the damping effect operated by the grid on the incoming turbulence has been analyzed and compared to previous evaluations proposed in several contributions [38, 39, 40, 41].

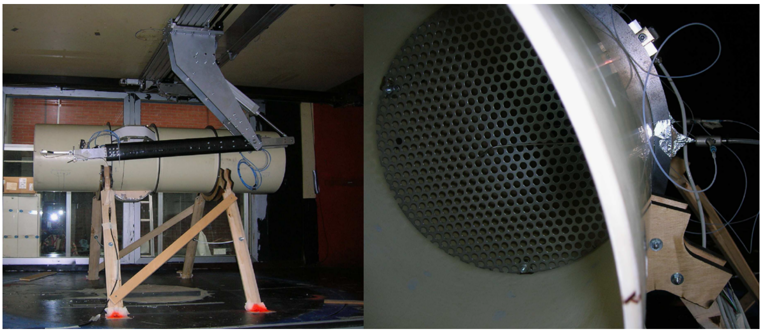

Figure 1.3: The porous surface in confined wind tunnel [35].

In the field of external aerodynamics, the simplest and more common case with is characterized by the presence of a porous surface is represented by ground mounted fences, see for instance Fig. 1.4 [13]. For fences, the relationship between drag force and porosity has been studied by [42]. In these studies, a boundary layer flow is considered and, consequently, the ratio between the fence height and the thickness of the boundary layer is analyzed, taking also into consideration the flow arrangement downstream of the porous fence. The elongation of the vortex in the wake with the increase of the fence porosity has been reported, for instance, by [43]. As regard applications, simple ground mounted fences are often applied as wind shields [44, 45] and for the moderation of dust emissions [46, 47]. For instance, the velocity field and pressure distribution around a model fence of finite length upstream of a dust source has been studied by [48].

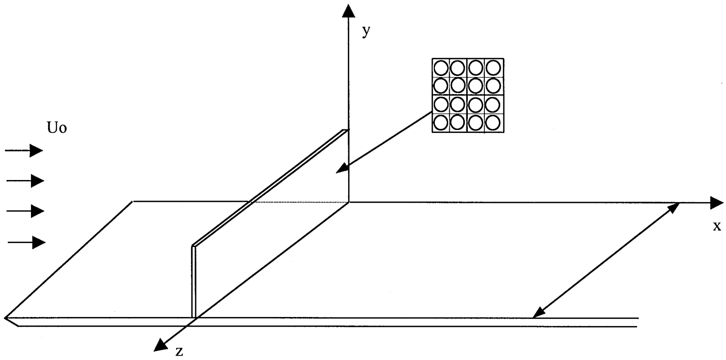

Figure 1.4: The model ground mounted fence [13].

A remarkable complication of the simple case mentioned above, is observed when the porous barrier is positioned above a bluff body. In this case, due to the well-known sensitivity of the flow to geometric details and the incoming flow turbulence, the overall flow arrangement can be potentially affected by the barrier and its geometrical details, even when it is characterized by very high porosity. This is the case of wind-shields over bridge decks, which are commonly used to protect traffic against strong cross wind [49]. Lately, for instance, the effect of porous barrier on the flutter derivatives of three model bridge deck sections has been experimentally studied in [2] (see Fig. 1.5).

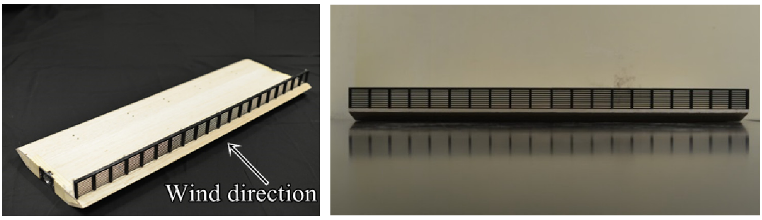

Figure 1.5: The porous barrier on long-span bridge [2].

As previously mentioned, the aerodynamic behaviors of bluff bodies is well-known to be extremely sensitive to geometrical details as well as the incoming flow conditions. This is due to the presence of separation bubbles whose scale is comparable to the immersed body size. The shape, organization and dynamics of those bubbles strongly depends on the stability conditions of shear layers detached from the body, often in correspondence of sharp edges. While such phenomena has been widely studied for solid bodies, structures obtained as an assemblage of porous surfaces (usually metal plates) have not been deeply studied yet. Generally speaking, it is known that the ventilation through the porous walls prevents the accumulation of vorticity, so having a favorable effect over the wind loading, in terms of both time-averaged and fluctuating components. This is the case commonly encountered in the cladding of reticular structures applied for aesthetic reasons and an emblematic example is the case of the antenna of the UniCredit building located in Milan, Italy [1] (see Fig. 1.6).

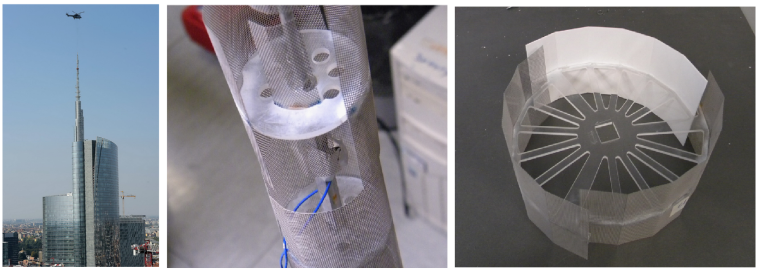

Figure 1.6: The porous surface on UniCredit building and its scaled model [2].

Porous surfaces can be also used to wrap solid structures in order to protect them from the direct action of the wind. A well-known example is the shrouded cylinders [50, 51, 52, 53], which have been repetitively studied aiming at suppressing Vortex Induced Vibrations, VIV. The advantage mainly comes, analogously to the previously mentioned case, by the ventilation through the external layer which prevents the accumulation of vorticity in the proximity of the body.

Finally, in recent years, porous surfaces are becoming increasingly used as external layer of double skin facades (see Fig. 1.7). Numerous studies, which are outside the scope of this short review, are dedicated to assess their efficiency in enhancing comfort and decreasing energy consumption [54, 14]. As regards their aerodynamic behavior, few studies have been presented at the moment. Among these studies, a common conclusion is that the porous external skin reduce the fluctuating pressure on the side faces and global forces [55].

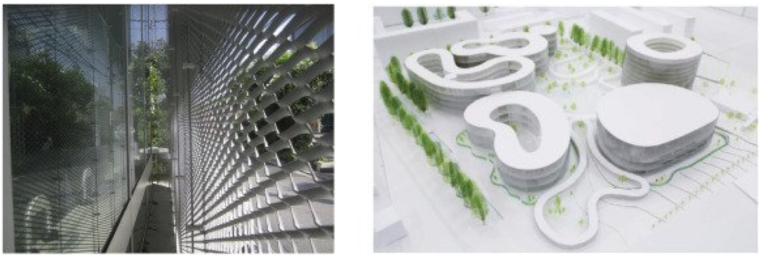

Figure 1.7: The building with porous external skin [3].

As regard CFD, due to the aforementioned difficulties, homogenization techniques appears to be a more practical alternative with respect to the explicit modeling of the geometry. A common way to describe the aerodynamic effect on such porous surfaces is to consider their resistance to the flow, i.e. the pressure loss coefficients, K [56, 57]. In such context,the aforementioned relations between pressure jump and surface porosity can be adopted. Such approaches for internal flows are well-established: for instance, by using two of such models [58, 59], [60] reports the comparison between computed pressure drop and experimental results, finding reasonably good agreement.

With respect to the use of such approach for simulating external flows, fewer studies are currently available. A well-known example is the actuator disc used to model the drag force over wind turbines [61]. In particular, such approach with several turbulence models is adopted by [62], which compares the velocity, turbulence intensity and shear stress in the turbine wake. It is found that the porous disk approach leads to acceptable results in the far wake but accuracy decreases just downstream the blades. Other similar application of porous media can be found, for instance, in the reproduction of the flow over forest canopies [63, 64], for which the explicit reproduction of the geometry is extremely difficult.

Summarizing, the use of homogenized modes to represent the effect of porous surfaces is still far from being well-established for external flows. In particular, numerous aspects would merit careful consideration. For instance, homogenized models assume vanishing pore size compared to the overall immersed body size. It is currently not clear how severe this limitation is in practice. Secondarily, empirical lows deduced for confined screens are usually valid for null or moderate attack angles. In the case of bluff bodies, the flow might be often almost tangential to the porous surfaces, so that evaluating the forces acting on them would require additional research. Finally, the pressure jump approach only considers forces exchanged from the fluid to the porous surface in the normal direction, so disregarding shearing effects.

Despite these potential disadvantages, the pressure jump approach still represents the most convenient and adopted method to represent porous surfaces at a reasonable computational cost [65, 66] and so, its validation appears to be fundamental in order to clarify the limits of its applicability.

1.3 Structure of the thesis

This thesis is organized as follows. After the introduction, Chapter 2 firstly reviews existing relations that links the pressure jump to the surface porosity. Then, a new model for the pressure jump calculation is proposed. After that, two modeling approaches are adopted to simulate the flow through a forward facing step (composed by a porous plate normal to the inflow and a solid plate parallel to the inflow): in the first one, the pores are explicitly modeled, so providing a detailed representation of the flow. In the second one, the porous surfaces are modeled by means of pressure jumps, which allow to take into account the presence of pores without reproducing the flow details. Consequently, the performance of such pressure-jump approach can be evaluated by comparing the obtained results.

Based on the above study, Chapter 3 and Chapter 4 evaluate the accuracy of pressure-jump based models by investigating the flow through more complex geometry: a hollow rectangular 5:1 cylinder composed by four porous plates. In these studies, the influences of surface porosity, angle of attack, turbulence model, local geometric features, pore number and size are considered.

Afterwards, in Chapter 5, the simulation of wind shields positioned on bridge decks is investigated, mainly with the intention to assess the use of simplified models based on pressure jumps for bridge decks optimization, for which the reduced computational cost of such models appears to be particularly attractive. In this case, results obtained by explicitly modeling the pores and using calibrated pressure jumps are compared to experimental values in terms of global forces and PIV measurements available in the literature.

Then, in Chapter 6 the case of a porous ground-mounted parallelepiped is considered taking into account different incoming flow conditions. In such case, wind tunnel tests have been appositely designed and performed in the wind tunnel in Tamkang University.

Finally, conclusions are drawn in Chapter 7.

The core of this thesis is composed by articles that have been published or submitted to international peer-reviewed journals. For this reason, the contents are provided without changes, while several additional results are added as appendixes.

Chapter 2

On the use of the pressure jump approach for the simulation of separated external flows around porous structures: a forward facing step

In this chapter, a new pressure-jump model is proposed for the high-Reynolds flow. The brief comparison of such new model and previous ones is also reported. Then, in order to evaluate the accuracy of the proposed relation, two modeling approaches are adopted to simulate the flow over a forward facing step, which is composed by a vertical porous surface and an horizontal solid surface: in the first one the pores are explicitly modeled. This approach provides a detailed representation of the flow through the pores, but requires remarkable computational resources. In the second approach, the pores are not modeled and the surfaces are simulated by means of pressure jumps, which allows to take into account the presence of pores without reproducing the flow details.

This chapter has been published as:

On the use of the pressure jump approach for the simulation of separated external flows around porous structures: A forward facing step. M. Xu, L. Patruno, Y.L. Lo, S. de Miranda, *Journal of wind engineering & industrial aerodynamics*, 207 (2020): 104377.

2.1 Introduction

Porous surfaces are becoming increasingly popular in architecture due to their well-known interesting combination of properties and functions: they allow to provide spatial separation yet keeping ventilation and partial sunlight penetration. In other circumstances, they are used in order to visually emphasize the architectural volumes while guaranteeing lightness and reduction of wind loading, see for instance the antenna of the UniCredit tower located in Milan, Italy [1]. Recently, the use of porous cladding is further increasing also due to the popularity gained by double skin facades, which often involve the use of highly porous elements which, nevertheless, remarkably affect the wind flow organization in the proximity of the building [3]. Other applications in the context of structural engineering can be found in the mitigation of bridge cables vibrations [67].

When such structures are exposed to the wind action, it becomes fundamental to be able to characterize their aerodynamic behavior. However, due to the presence of small pores, the measurement of pressures around such bodies is not easily accomplished by means of standard pressure taps in wind tunnel experiments. In fact, the need to install pressure taps on both sides of the surface, the impossibility to embed the piping system within the surface itself and the difficulties found in avoiding local flow disturbances, render the study of bodies partially or entirely composed of porous surfaces a difficult task. Due to such difficulties, studies of bluff bodies composed of porous surfaces are still scarce in the literature with the notable exception of simple geometries such as fences and plates (see for instance [12, 10, 13, 68]) and cylinders surrounded by a porous shelter [69, 70, 71, 72, 73].

In such context, Computational Fluid Dynamics, CFD, might represent an approach able to overcome many of the aforementioned difficulties. The possibility to obtain a detailed characterization of the flow without the need to install a measurement system and, thus, avoiding also its interaction with the flow itself, surely represents a great advantage when considering porous surfaces. Unfortunately, taking into account the presence of pores by explicitly simulating their geometry usually leads to prohibitive computational costs. For structures in which the number and size of the holes still allow their explicit modelling, uncertainties regarding how fine the computational mesh should be in the holes often arises.

For structures in which the size of the holes vanishes with respect to the overall dimensions, a well-known and convenient alternative is to model the presence of the surface by means of appropriate pressure jumps, Δp, which can represent the porous surfaces without simulating the details of the flow. A rigorous approach to the subject would require to frame it in the theory of asymptotic homogenization

[34]. In essence, the presence of the pores induces variations in the flow field characterized by small space and time scales which can be averaged out, so allowing to study the flow behaviour at the macro-scale by providing a simplified model of its behaviour at the micro-scale.

Currently, such a modelling approach is well established for internal aerodynamics (e.g. flows trough porous screens and filters) but it is not widely validated for external aerodynamics problems, although interesting contributions can be found in [74, 31, 19]. It is worth to mention that, on the other side, research work has been already performed as regards the aerodynamic behaviour of solid bluff bodies internally made of porous materials which allow filtration (see for instance [21, 20] and attempts have been also made to control the body aerodynamic behaviour by modifying their geometry with porous appendices and layers [75, 76].

When it is necessary to simulate the flow through a porous surface, a fundamental aspect is represented by the relationship existing between Δp and the surface porosity, β. A quantitative prediction of Δp as a function of β has been provided by [36]. Then, a number of studies have been proposed, aiming at obtaining such relations from a theoretical point of view. As an example, a particularly simple and effective one consists in assimilating the grid to an array of objects immersed in a uniform velocity field, whose velocity is increased with respect to the free-stream one in order to consider the blockage effect [77].

Other evaluations of the relation between $\beta - \Delta p$ can be found in [78] and [79], while a review paper has been recently presented by [80], showing varying degree of accuracy of the proposed laws. Finally, a fifth-order polynomial fitting of the data presented in [81, 82, 83] has been proposed by [84].

In this paper, firstly the flow through porous surfaces is studied in detail at the micro-scale by means of Large Eddy Simulations (LES). Based on the obtained results and supported by the experimental observations reported in [35], a new $\beta - \Delta p$ relationship is proposed. The advantage of the new relation is represented by the fact that the quantities appearing in the model are all easily identifiable and provide an accurate description of the flow in the proximity of the porous surface.

Then, with the aim of validating the use of simulations based on the pressure jump approach for external detached flows, a forward facing step is considered. The vertical surface of the step is assumed to be porous while the horizontal surface is assumed to be solid. The model is built in such a way that it can be considered representative of the flow detached from the leading edge of an elongated bluff body with a porous frontal face, at null angle of attack. The problem is solved by explicitly modelling the geometry of the pores as well as using the pressure jump approach, so allowing to compare the obtained results.

The chapter is organised as follows. A review of the available $\beta - \Delta p$ relations is provided in Section 2.2. Large-eddy simulations of the flow past a representative element of an infinitely extended porous surface are shown in Section 2.3. In Section 2.4, the new $\beta - \Delta p$ relation is described. The forward facing step between a porous and a solid surface is analysed in Section 2.5. Finally, conclusions are drawn in Section 2.6.

2.2 Review of $\beta - \Delta p$ models

In this section, three well-known models for the prediction of the $\beta - \Delta p$ relationship are described. Figure 2.1 shows a section of a representative sample of an infinitely extended porous surface, also called grid screen in the following. The domain is subdivided into two parts (*Part I* and *Part II*). In particular, *Part I* is defined as the zone from the inlet to the front surface of the grid screen, while *Part II* is defined as the zone from the front surface of grid screen to the outlet. In the same figure, three planes, whose intersection with the domain identify three slices, are shown. *Slice 0* corresponds to the free-stream upstream the porous grid, *Slice 1* is located just upstream the porous surface while *Slice 2* is located far downstream the porous surface. In practice, *Slice 0* and *Slice 2* must be located at a distance from the porous screen which is high compared to the pores characteristic dimension.

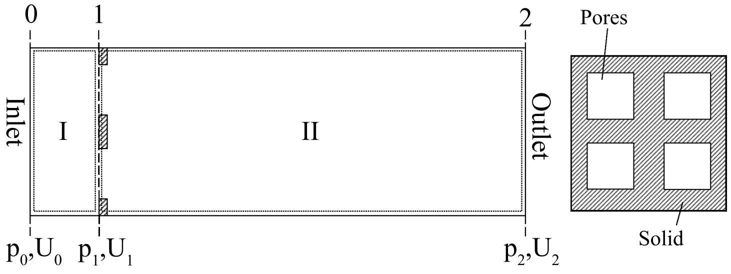

(a) (b)

Figure 2.1: Overview of a representative sample of an infinitely extended porous surface: (a) side view and (b) frontal view.

We define the homogenized pressure over the surface S_i through the following well-known equivalence

$$p_i A_i = \int_{S_i} p \, \mathrm{d}S_i, \tag{2.1}$$

where p_i is the homogenized pressure, p is pressure and A_i is the area of the surface S_i, which includes fluid as well as solid parts, if present.

With reference to Fig. 2.1, the homogenized values coincide with the punctual values for the surfaces identified by *Slice 0* and *Slice 2* while, for *Slice 1*, punctual values vary from point to point due to the presence of the pores. Additionally, a discontinuity Δp is present in the homogenized pressure when it is measured just upwind or downwind the porous surface.

Defining the porosity, β, as the ratio between the pores area over the total area, Δp can be expressed in terms of the pressure loss coefficient, K, as

$$\Delta p = \frac{1}{2}\rho U_0^2 K(\beta), \tag{2.2}$$

where ρ is the fluid density and U_0 is the free-stream velocity. In the following, some of the formulations available in the literature for the estimation of $K(\beta)$ are described.

2.2.1 Wieghardt's model

The basic idea underlying this model is to match the drag force provided by Δp with that expected on the grid screen. Firstly, it is noticed that, for incompressible fluids, mass continuity requires the fluid velocity through the holes in *Slice 1* to be U_0/β. Thus, [77] assumed that the grid screen is completely immersed in a flow with velocity equal to U_0/β. On the one hand, the drag force experienced by the grid is calculated as

$$F_D = \Delta p A = \frac{1}{2}\rho U_0^2 A K(\beta). \tag{2.3}$$

On the other hand, the same drag force might be also evaluated as

$$F_D = \frac{1}{2}\rho \left(\frac{U_0}{\beta}\right)^2 (1-\beta) A c, \tag{2.4}$$

where c is a constant (i.e. the drag coefficient of the objects composing the grid). Taking into account the experimental results of [85], the constant c has been evaluated to be $c \approx 1$. Therefore, equating Eq. (2.3) and Eq. (2.4), the following expression can be obtained

$$K(\beta) = \frac{1-\beta}{\beta^2}. \tag{2.5}$$

It should be noticed that such model, and thus the value of the calibrated c constant, have been initially obtained for a porous grid composed of wires characterized by a round section.

2.2.2 Eckert's model

We again start by considering a constant mass flow rate through all slices. Continuity will thus require

$$\rho U_0 A = \rho U_1 \beta A = \rho U_2 A, \tag{2.6}$$

where, with a little abuse of notation, U_1 represents the velocity in the holes and not the homogenized velocity at *Slice 1*.

Considering *Slice 1* and *Slice 2*, the following assumption as regards the hydraulic head is considered by [36]

$$p_1 + \frac{1}{2}\rho U_1^2 = (p_2 + \Delta p) + \frac{1}{2}\rho U_2^2, \tag{2.7}$$

which states that the pressure jump through the screen, equal to the drag force on the grid per unit area, is equal to the jump of the hydraulic head. In such formula it must be noticed that the pressure p_1 indicates the homogenized pressure just upstream the porous surface while, as previously clarified, the velocity U_1 does not represent an homogenized velocity. Such equation can be rewritten as

$$(p_1 - p_2) = \Delta p - \frac{1}{2}\rho\left(U_1^2 - \rho U_2^2\right). \tag{2.8}$$

Next, considering that the mass flux is constant in all slices and equal to $\rho U_2 A$, the momentum balance of *Part II* can be given as

$$\rho U_2 A \left(U_1 - U_2\right) + \left(p_1 - p_2\right) A = 0. \tag{2.9}$$

The substitution of Eq. (2.8) into Eq. (2.9) leads to

$$\Delta p = \frac{1}{2}\rho\left(U_1^2 - U_2^2\right) - \rho U_2 \left(U_1 - U_2\right). \tag{2.10}$$

Furthermore, using Eq. (2.6), Eq. (2.10) can be written as

$$\Delta p = \frac{1}{2}\rho U_0^2 \left(\frac{U_1}{U_0} - 1\right)^2. \tag{2.11}$$

Finally, using again Eq. (2.6) and considering $U_0 = U_1\beta$, the pressure loss coefficient can be evaluated as

$$K(\beta) = \frac{(1-\beta)^2}{\beta^2}. \tag{2.12}$$

Notice that, the pressure jump Δp is measured from *Slice 1* to *Slice 2* which means that the pressure jump will be accurately predicted only if measured far downstream the porous surface, the actual distance being sufficiently higher than the dimension of the pores.

2.2.3 Annand's model

It has been shown that Eckert's model obtains the $\beta - \Delta p$ by assuming Δp to be equal to the jump in the hydraulic head through the grid screen. In general, it has been shown by [78] that

$$K(\beta, \delta) = \frac{1-\delta}{\beta^2} - 1, \tag{2.13}$$

where δ is the fraction of the hydraulic head lost in passing through the porous surface. Starting from this point of view, [79] suggested the following expansion into powers of β

$$K(\beta) = \frac{f_1\left(1 + f_2\beta + f_3\beta^2\right)}{\beta^2}, \tag{2.14}$$

where the f_1, f_2 and f_3 are three constants.

Considering that Eq. (2.14) should give $K(1) = 0$, the numerator must contain a factor $(1 - \beta)$. Consequently, Eq. (2.14) can be written as

$$K(\beta) = \frac{f_1(1-\beta)\,(1-f_4\beta)}{\beta^2}, \tag{2.15}$$

where f_4 is a constant.

After calibration on the experimental measurements of low-Reynolds-number flow, the following expression has been proposed

$$K(\beta) = \frac{0.68(1-\beta)\,(1+1.1\beta)}{\beta^2}. \tag{2.16}$$

Then, considering that $(1-\beta)(1+\beta) = 1-\beta^2$, a simplified version of Eq. (2.16) can be obtained as

$$K(\beta) = \frac{0.71(1-\beta^2)}{\beta^2}, \tag{2.17}$$

which proves to be almost identical to the previous one for $\beta > 0.27$.

2.2.4 Summary

A comparison of the models introduced in the previous sections is provided in Figure 2.2. In addition, the figure shows experimental results provided by [35] and the $5th$ order polynomial fitting reported in [84] (notice that such last law is an interpolation of experimental data and, in fact, it does not show the correct asymptotic behaviour for β approaching 1).

In particular, [35] investigated the flow through gird screens (perforated metal sheets) characterized by different porosities. Such experiments have been performed on a wide set of grids characterized by different t/D_h ratios, being t the porous grid thickness and D_h the pores hydraulic diameter (defined as $D_h = A_h/L_h$ where A_h is the pore area and L_h is the pore semi-perimeter). The ratio t/D_h ranged from 0.125 to 1.5. Such information has been qualitatively reported in Fig. 2.2 by adopting for experimental data a marker size proportional to t/D_h. The Reynolds number is calculated based on D_h to ignore the shapes of pores, which ranged from 3000 to 15000.

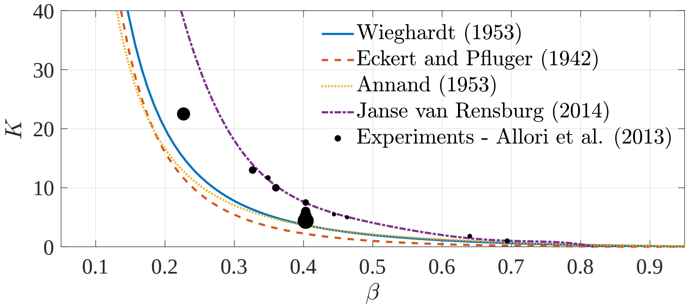

Figure 2.2: Comparison between $\beta - \Delta p$ models and experimental measurements reported in [35]. For [35] the marker size is proportional to t/D_h which ranges from 3000 to 15000.

On such regard, the different nature of the experiments used to calibrate the previously presented models and the experiments reported in [35] should be highlighted. While in the fist ones the grid was composed by wires, in the second one perforated metal sheets were considered. Indeed, curves are in reasonable agreement with experimental results if scaled by a factor approximately equal to 2.0, which is close to the ratio between the drag of a cylinder and that of a flat plate perpendicular to the flow.

In order to improve the predictive accuracy of the aforementioned models, a number of corrections aimed, for example, at taking into account the Reynolds number, have been proposed, mainly based on the fitting of experimental data. The readers can refer to [79, 77, 86, 87, 88, 89, 90, 91, 86, 92] while a review paper has been presented in [80].

2.3 Flow through a porous surface

In this section, LES are performed on an elementary geometry, representative of an infinitely extended porous surface. In particular, as shown in Fig. 2.3, an array of 2x2 square holes is considered: it is reminded that it is well known from experimental results given by [35] and [25] that the shape of the holes has very small influence on the obtained results, so that the investigation can be limited to such simple geometry.

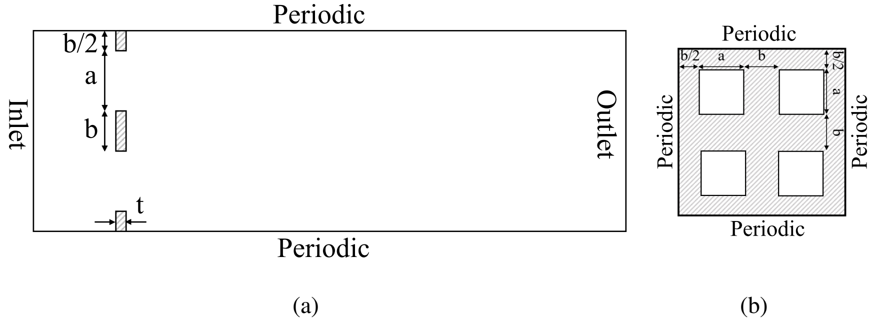

Figure 2.3: Overview of the considered geometry: (a) side view and (b) front view.

Three porosities are analysed, namely $\beta = 16\%, 25\%, 64\%$. Such different porosities are obtained by keeping the size of the holes constant and changing their spacing. In particular, the side of the holes is denoted as a while the spacing between the holes is denoted as b. The ratio t/D_h as well as the Reynolds number based on D_h are kept constant for all geometries and equal to 0.125 and 6000, respectively. A summary of the geometrical properties used in the analyses is provided in Table 2.1.

Table 2.1: Summary of the geometrical parameters used in the numerical analyses.

β	a/D_h	b/D_h	t/D_h
16 %	0.5	0.75	0.125
25 %	0.5	0.5	0.125
64 %	0.5	0.125	0.125

2.3.1 Numerical models

Structured meshes composed of hexahedral elements with non-conforming transitions between refinement levels are adopted as shown in Fig. 2.4. In order to study the effect of the mesh sizing in the proximity of the holes, three mesh refinements are adopted, denoted as *Coarse*, *Middle* and *Fine*. Such refinement levels correspond to a cell size in the proximity of the pores equal to $1/16D_h$, $1/32D_h$ and $1/64D_h$, respectively. The total number of cells for the meshes used to simulate $\beta = 16\%$ amounts to $0.32M$, $2.15M$ and $4.91M$ cells.

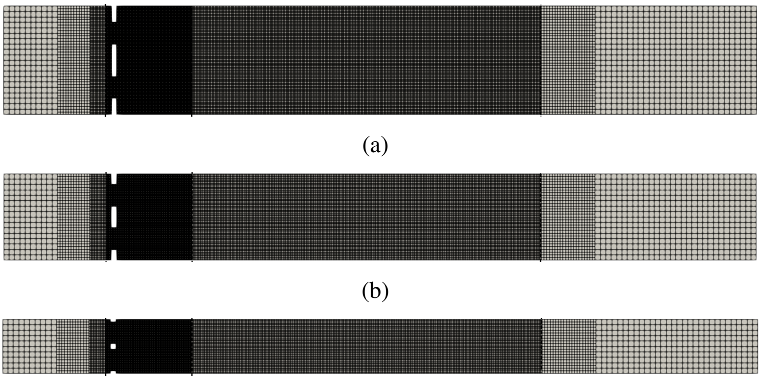

(a)

(b)

(c)

Figure 2.4: Overview of the adopted *Fine* meshes: (a) $\beta = 16\%$, (b) $\beta = 25\%$ and (c) $\beta = 64\%$.

In particular, the detailed illustration of the mesh around the pores are shown in Fig. 2.5, where the case characterised by $\beta = 16\%$ is adopted as an example. It can be seen that each edge of the pores are respectively meshed by 2, 4 and 8 cells.

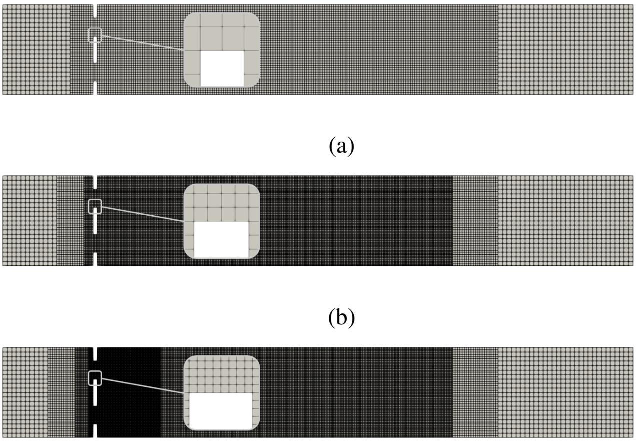

(a)

(b)

(c)

Figure 2.5: Illustration of the adopted meshes around pores for: (a) *Coarse*, (b) *Middle* and (c) *Fine* that characterised by $\beta = 16\%$.

As indicated in Fig. 2.3, periodic boundary conditions are adopted for all lateral faces. The upwind and downwind surfaces of the grid are considered as walls while the surfaces surrounding the holes are set as slip in order to simulate an high Re number and minimize as much as possible the role played by viscous forces on the pore sides. As usual, null pressure is imposed at the outlet while null pressure gradient is imposed at the inlet. In the current simulation it is thus expected that the pressure measured at the inlet will coincide with Δp.

As regards the subgrid-scale model, the well known one equation eddy-viscosity model is adopted.

The LUST scheme is used for advective terms, time integration is performed by using the Crank-Nicolson scheme while pressure-velocity coupling is obtained using the Pressure Implicit with Splitting of Operator (PISO) algorithm. The non-dimensional time step based on D_h is equal to 5.0×10^{-3} for the *Coarse* and *Middle* meshes, while it is equal to 2.0×10^{-3} for *Fine* meshes. The maximum Courant number is approximately 1.3.

The open source finite volume software OpenFOAM version 7 is used for all simulations. The cases with the highest mesh resolution are performed with 68 cores on the Marconi cluster at CINECA (68 Intel Xeon Phi7250 1.4GHz processors and 16+96GB RAM per node).

2.3.2 Results

The qualitative representation of the velocity fields obtained is provided in Figure 2.6 by means of Line Integral Convolution. By comparing the cases characterized by the same porosity, it can be noticed that the lengths of the recirculation zones behind the grid screen (marked with light blue shadows) are longer when the coarser meshes are adopted. The length of the recirculation bubble is approximately halved when passing from the *Middle* to the *Fine* meshes. Considering that in this case only an elementary portion of the grid is simulated and that the adopted meshes are already of considerable size, such result emphasizes the difficulties encountered in accurately simulating the flow through the pores, so highlighting the necessity to use an homogenized model whenever possible.

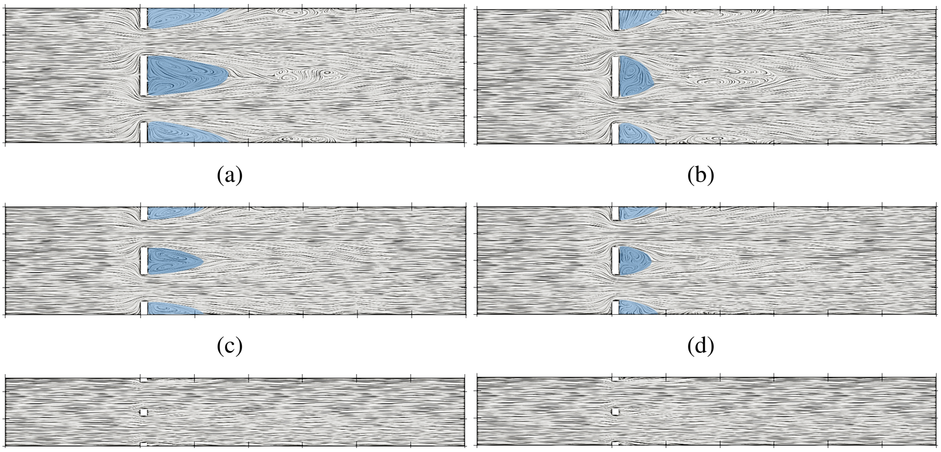

(a) (b)

(c) (d)

(e) (f)

Figure 2.6: Line Integral Convolution of time-averaged velocity field: (a) *Middle* $\beta = 16\%$, (b) *Fine* $\beta = 16\%$, (c) *Middle* $\beta = 25\%$, (d) *Fine* $\beta = 25\%$, (e) *Middle* $\beta = 64\%$, (f) *Fine* $\beta = 64\%$. The recirculation zones are marked by light blue contours.

Such mesh sensitivity around pores can be also found in the turbulence structures, which is shown in Fig. 2.7 by means of the contours Q. When a fine mesh is adopted, the length of the complex turbulence structures become shorter on wind direction.

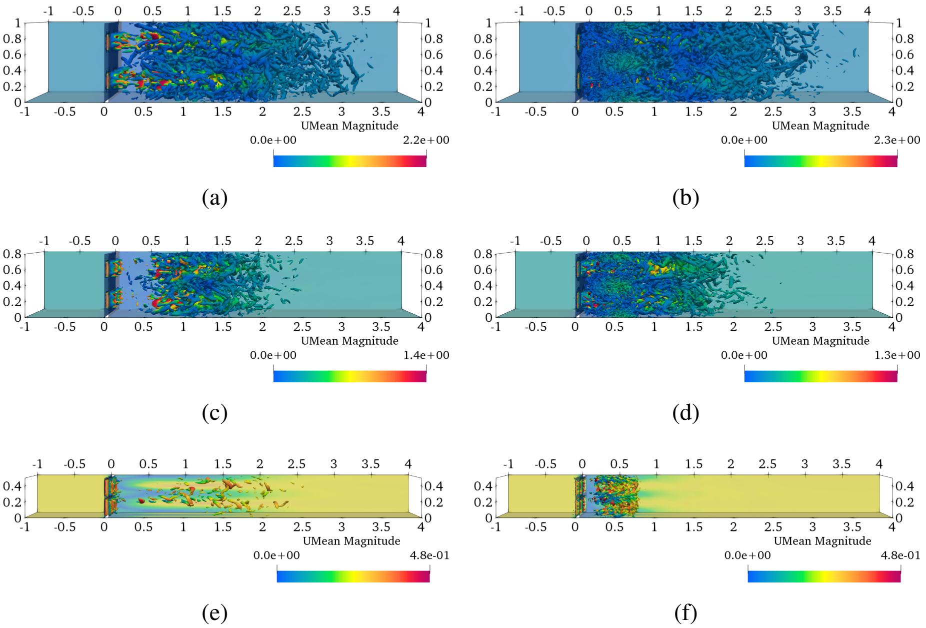

(a) (b) (c) (d) (e) (f)

Figure 2.7: The contours of Q for: (a) *Middle* $\beta = 16\%$, (b) *Fine* $\beta = 16\%$, (c) *Middle* $\beta = 25\%$, (d) *Fine* $\beta = 25\%$, (e) *Middle* $\beta = 64\%$, (f) *Fine* $\beta = 64\%$, which are also colored by the time-averaged velocity.

The time-averaged pressure distributions are shown in Figure 2.8 for the *Middle* meshes, for all porosities.

Negative pressure is observed for all cases, just downstream the grid. Such negative pressure is recovered far downstream, finally stabilizing to the null value imposed by the outlet boundary condition. The pressure recovery, associated to the fluid vein expansion downwind the grid screen, appears to be completed at a distance approximately equal to $2D_h$, being finer meshes characterized by a lower peak suction and a shorter pressure recovery zone, in agreement with other results obtained for bluff bodies, as well documented for instance in [93].

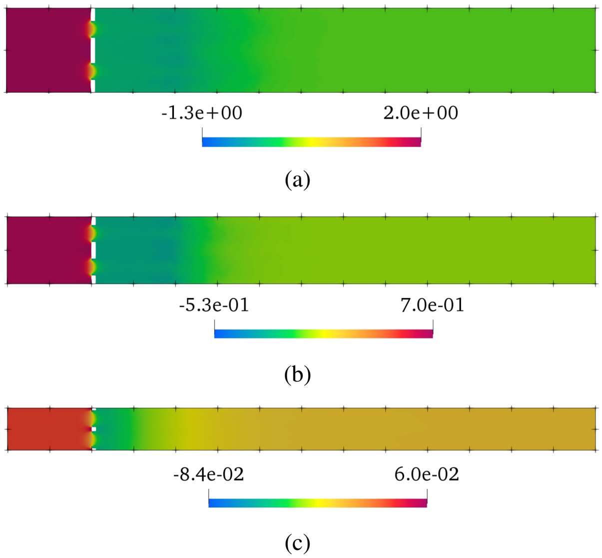

(a)

(b)

(c)

Figure 2.8: Time-averaged pressure field for the *Middle* mesh: (a) $\beta = 16\%$, (b) $\beta = 25\%$ and (c) $\beta = 64\%$.

Finally, the evolution of the homogenized pressure coefficient, C_{ph}, in the along wind direction is shown in Fig. 2.9. C_{ph} is calculated from the homogenized pressure, p_h, calculated on a series of planes located at different along-wind positions by means of Eq. (2.1) and normalizing it using the dynamic pressure calculated based on the free-stream velocity. Also in this figure, the strong pressure drop at the grid back face and the subsequent pressure recovery can be clearly observed.

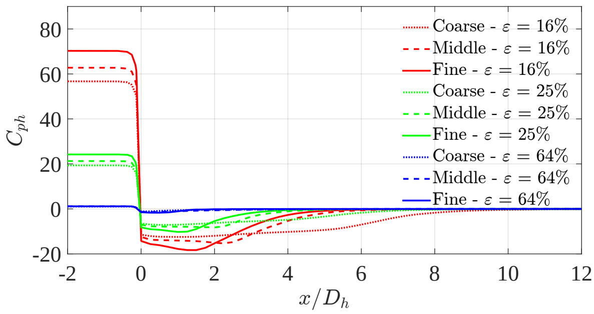

Figure 2.9: Homogenized pressure coefficient along the wind direction. The origin is located in correspondence of the back surface of grid screen.

Summarizing, the flow past porous surfaces is characterized by strong suctions after the grid, followed by a pressure recovery at a distance approximately equal to $2D_h$, which is equal to $4a$ in the case of grids with square holes. In essence, the grid contracts the fluid vein and, then, allows its complete expansion after the recirculation zone: the actual geometry of the grid is represented by the solid part and the recirculation zones downstream the grid. When pores are very small compared to the structure under consideration, the pressure recovery zone is so short to be negligible, while, when pores are numerous but not of vanishing size compared to the immersed body, results obtained using a pressure jump approach might be affected by inaccuracies due to such effect.

2.4 A new $\beta - \Delta p$ relationship

We now proceed at developing a novel $\beta - \Delta p$ relationship, which can be considered a detailed version of the ones reported in Sec. 2.2. Attention is devoted to link the model parameters to well-defined quantities which can be easily measured in experiments or CFD analyses. Such an approach has the advantage to provide a clear overview of the flow arrangement.

In particular, with reference to Fig. 2.10 (a), the domain is subdivided into three parts. *Part I* extends from the upstream undisturbed flow to an infinitesimal distance upstream the grid. *Part II* extends upstream and downstream the grid for an infinitesimal distance while *Part III* extends from the end of *Part II* to the downstream undisturbed flow. All quantities in the following shall be intended as calculated for unit area of the porous surface.

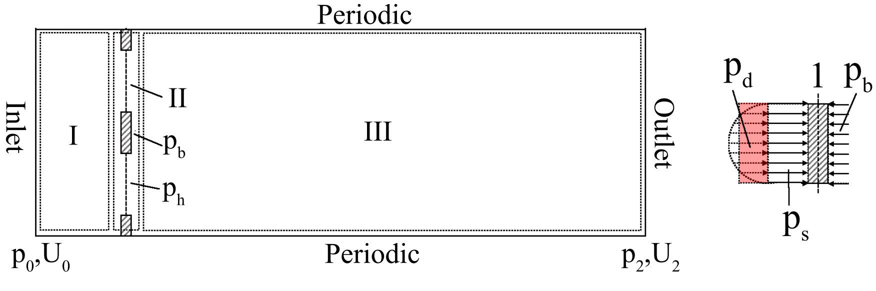

(a)

(b)

Figure 2.10: Schemes used to derive the proposed model: (a) subdivision in zones and (b) detail of the pressure distribution over the solid part.

Considering that at *Slice 0* and *Slice 2* (see Fig. 2.10) the momentum flux given by the mass flow is equal and opposite, the equilibrium of $I + II + III$ requires

$$F_D = p_0 - p_2, \tag{2.18}$$

where F_D is the drag force on the porous surface. Starting from the pressure distribution over the grid screen, F_D can be expressed as

$$F_D = \left(\frac{1}{2}\rho\alpha U_0^2 + p_0 - p_b\right)(1-\beta), \tag{2.19}$$

where p_b is the average pressure measured at the back of the grid. The first two terms on the right hand side should be interpreted as follows. The streamline starting from far upwind and impinging at the centre of the solid part conserves its energy so that, thanks to Bernoulli's theorem, the pressure at the centre of the solid face can be evaluated as the sum of the static and the dynamic pressure, as shown in Fig. 2.10 (b). Actually, the static pressure, $p_s = p_0$, is uniformly distributed while the dynamic pressure, p_d, is distributed in a parabolic way. The coefficient α appearing in Eq. (2.19) thus represents the ratio between the integral of a parabolic distribution and that of a uniform distribution of equal area (reported in red in Fig. 2.10 (b)). In a two-dimensional case such coefficient is equal to $2/3$, as can be deduced for instance from the Gauss-Lobatto integration rule. For rectangular solid areas, α would be equal to $(2/3)^2$. As it can be seen, the range of variability is extremely small, so that $\alpha \approx 0.5$ can be adopted.

Next, the momentum balance of *Part III* is written as

$$\rho\beta U_1^2 + \beta p_h + (1-\beta)p_b = p_2 + \rho U_2^2. \tag{2.20}$$

where p_h is a measure of the pressure in correspondence of the holes, just after the grid. We further assume

$$p_h = p_2 + \beta\left(p_0 - p_2\right), \tag{2.21}$$

where β is a constant to be calibrated based on experimental and/or numerical data.

By solving the system composed by Eq. (2.18)-(2.21), we obtain

$$F_D = \frac{1}{2}\rho U_0^2 \frac{(\alpha\beta + 2)(\beta - 1)}{\beta^2(\beta - 1)}. \tag{2.22}$$

Then, by virtue of Eq. (2.18), which allows to identify $F_D = \Delta p$, we obtain

$$K(\beta) = \frac{(\alpha\beta + 2)(\beta - 1)}{\beta^2(\beta - 1)}. \tag{2.23}$$

As anticipated, $\alpha \approx 0.5$ while, by best fit of the experimental data from [35], $\beta \approx -0.1$ has been obtained.

Finally, it is possible to calculate

$$p_b = p_2 + \frac{1}{2}\rho U_0^2 K_b = p_2 + \frac{1}{2}\rho U_0^2 \frac{2 + \alpha\beta\beta}{\beta(\beta - 1)}, \tag{2.24}$$

where K_b represents the average non-dimensional pressure on the back of the grid with respect to the far-downstream pressure. Notice that the second term composing K_b is actually very small and that K_b is not a vanishing quantity for β approaching 1 but, nevertheless, the force over the grid does vanish due to the vanishing of the solid area.

A comparison between the proposed model, the results obtained from LES and available experimental results is reported in Fig. 2.11. As in the previous figure, markers used to represent experimental results reported in [35] are proportional to the t/D_h ratio. In particular, Fig. 2.11 (a) reports K showing very good agreement between the proposed law and experimental results, especially when low values of t/D_h are considered. Figure 2.11 (b) reports K_b obtained by means of the proposed model and the one measured averaging pressures on the back of the solid part of the grid screen in LES. Here the accuracy of the proposed model appears to be less marked although, overall, results appear to be well acceptable in terms of trends and orders of magnitude. It can be also seen that, despite the fact that the *Fine* meshes are of considerable size with respect to the problem geometric complexity, results still show a marked mesh dependency, with *Fine* meshes generally providing higher resistance with respect to *Coarse* meshes. This might be due to the organization of the flow inside the hole in which *Coarse* meshes do not allow to model the vein contraction inside the hole in an accurate way.

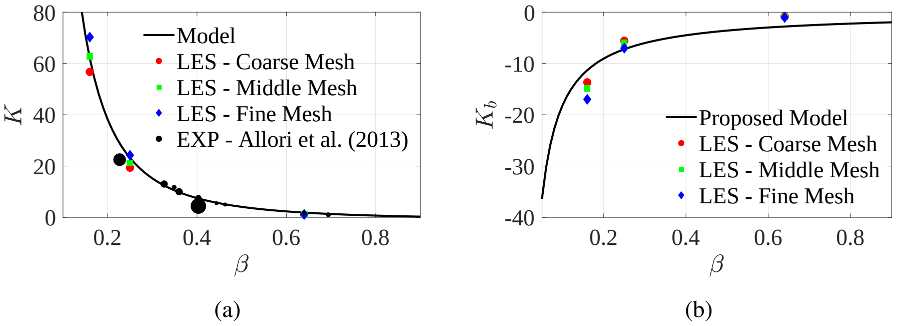

Figure 2.11: Results obtained by means of the proposed model and comparison with experimental results: (a) K and (b) K_b. Markers used for [35] are proportional to the t/D_h ratio.

Summarising, the proposed model allows to evaluate the $\beta - \Delta p$ relationship for porous surfaces at high Reynolds number with high accuracy. The model provides a more detailed description of the flow organization in the proximity of the grid with respect to previously available ones. Obtaining an accurate and mesh independent prediction of the resistance of the grid by modelling explicitly the pores geometry proved to be very cumbersome from the computational point of view, with fine meshes generally providing higher resistance with respect to coarse ones. The proposed model, thanks to its detailed point of view, might be also amenable to further extensions aimed at modelling grids whose geometry induce a directionality to the flow [3].

2.4.1 Effect of incidence angle

An important aspect which needs consideration in order to adopt a $\beta - \Delta p$ relationship to model porous surfaces is represented by the dependency of Δp with the angle of attack. This is of great importance for porous bluff bodies aerodynamics in which it is not possible to predict in advance the wind angle with respect the porous surface. The subject has been already studied in the literature and the reader can refer to [94, 95] and to [25] for a more recent investigation.

One frequently referred prediction model in this case is given by [96], which reads

$$K(\beta, \theta) = K(\beta) \cos^2 \theta, \tag{2.25}$$

where θ is the angle between the porous surface normal and the approaching flow. This corresponds to calculating the pressure jump by considering only the velocity component normal to the inflow. A series of numerical simulations have been thus performed by using the same models previously described and applying a skew incoming velocity. Due to the adopted periodic boundary conditions, no other change needed to be made. In order to limit the computational effort, only *Middle* meshes are here considered.

Figure 2.12 reports a comparison of the results obtained by using the proposed model and LES. In particular, Fig. 2.12 (a), (b) and (c) report the distribution of the homogenized time-averaged pressure coefficient, C_{ph}, as a function of the along wind position in LES (the back of the porous surface is assumed to be positioned at $x = 0$). In Fig. 2.12, results are further normalized by means of $K(\beta, \theta)$ so that values located far upstream the grid are expected to be equal to unity. Considering Fig. 2.12 (a), which corresponds to $\beta = 16\%$, we can observe that values very close to unity are observed for $x/D_h = -2$, being the only exception the flow at 80°, which shows a higher resistance than expected. This effect should be probably associated to the thickness of the pores which was not taken into account neither in deriving the proposed $\beta - \Delta p$ relationship, nor in Eq. (2.25). Corrections able to take such effect into account can be found in [84]. Such aspect has been here disregarded also by noticing that, although emphasized in the plot, it is not expected to change results substantially for thin grids: actually the plotted values span many orders of magnitude and their relative size is well captured by the model, as it can be seen in Fig. 2.12 (d) where the function $K(\beta, \theta)$ is compared with results from LES.

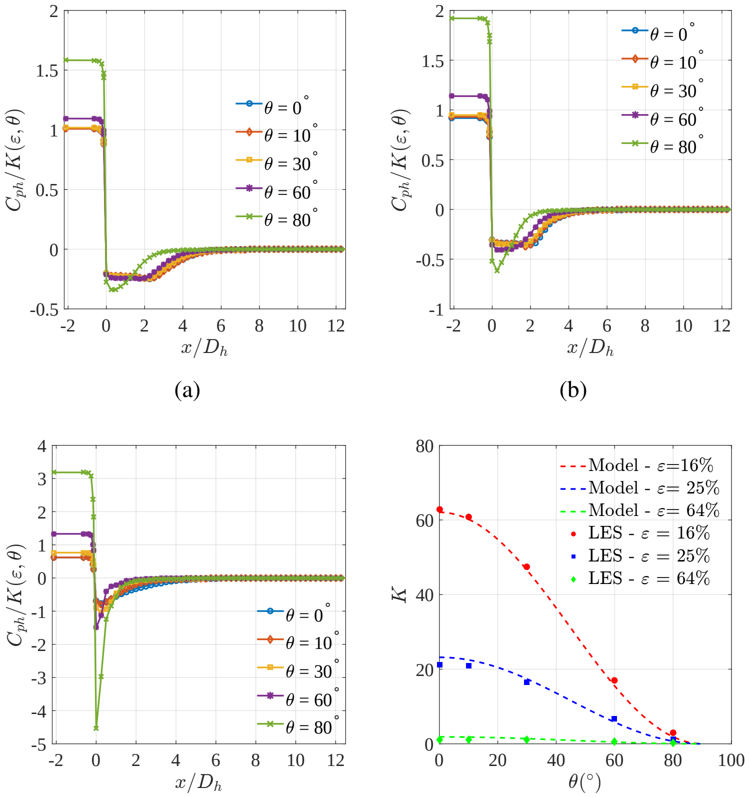

(a) (b) (c) (d)

Figure 2.12: Distribution of C_{ph} with respect to the along wind position and angle of incidence of the incoming flow: (a) $\beta = 16\%$, (b) $\beta = 25\%$, (c) $\beta = 64\%$, (d) overview of $K(\beta, \theta)$.

The consideration reported above for Fig. 2.12 (a) apply also to Fig. 2.12 (b) and Fig. 2.12 (c). We finally notice that the numerical simulations indicate that the pressure recovery is completed at a distance from the grid equal to $2D_h - 4D_h$, which, in this case, corresponds to $4 - 8$ hole side lengths. This is thus the distance after which the inhomogeneities of the flow induced by the pores can be considered extinguished.

The comparisons between the proposed model and previous ones are shown in Fig. 2.13. Satisfying agreements are noticed between the proposed model and experimental results, especially when the adopted porosity is larger than 35%. Meanwhile, it should be noticed that the previous models of [36, 77, 79] are proposed for low-Reynolds flow, which therefore give discrepancies in this comparison.

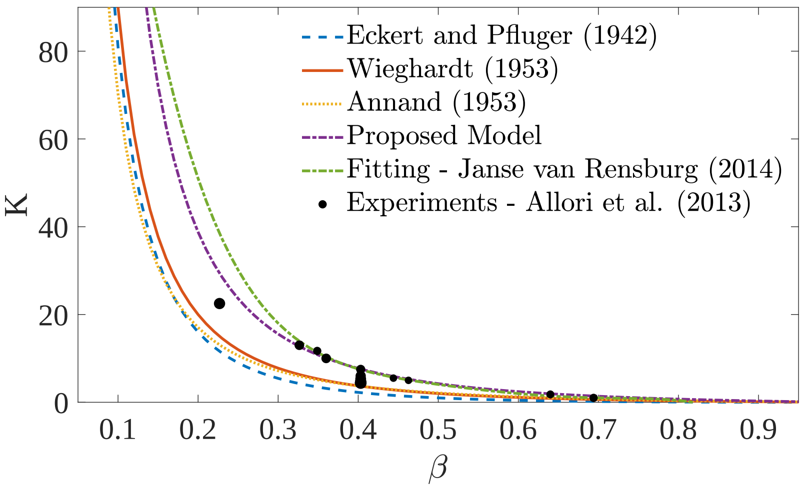

Figure 2.13: The $K - \beta$ relations of the proposed and previous models.

2.5 Porous forward facing step

We now apply the developed $\beta - \Delta p$ relationship to study the flow over a forward facing step between a porous and a solid surface. The case can be considered one of the simplest example of separated flow at a sharp edge and, thus its study is fundamental in order to validate the performance of the pressure jump modelling approach in the case of porous bluff body aerodynamics. In Fig. 2.14 the geometry of the analysed cases are reported. In particular, symmetry conditions are adopted at the bottom and top of the domain. The face of the step normal to the incoming flow is porous with $\beta = 25\%$ while the surface parallel to the incoming flow is modelled as a wall. The height of the step is denoted as B. Periodic conditions are adopted on the sides, so simulating a step infinitely extended in the span-wise direction. Such geometry, due to symmetry, can be considered representative of half of the frontal part of an elongated prism at null angle of attack.

Three cases are analysed: in the first one porosity is provided by means of two rows of 1.5 square pores on the frontal face of the prism (if the symmetric body is considered this leads to 3 pores on the frontal face). Such case is denoted as *1.5 Pores* in the following. The second case is similar to the *1.5 Pores* one but 3 pores are used and it is denoted as *3 Pores* in the following. Finally, the pressure jump approach is used, theoretically equivalent to an infinite number of pores. Such last case is denoted as *Baffle* in the following.

Meshes are created in analogy to those used in Section 2.3 and using 16x16 cells to mesh each pore and 4 cells along the pores thickness. The cell size in the zone in which the flow separates and recirculates is kept equal to $B/48$ in all cases. An overview of the adopted meshes, which count approximately 3M cells, is provided in Fig. 2.15. Also numerical settings follow the same criteria adopted in Section 2.3.

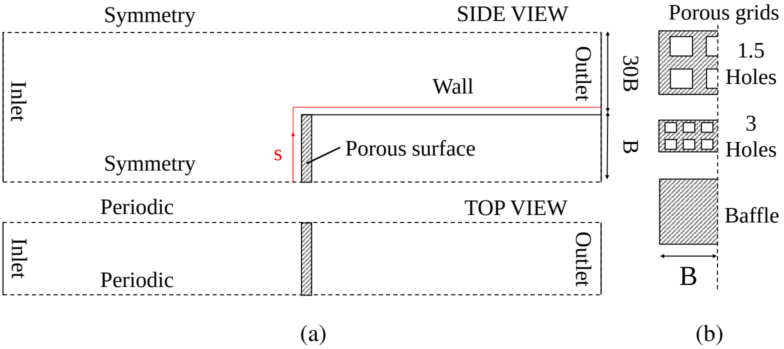

Figure 2.14: Overview of the simulated geometry: (a) computational domain, (b) details of the porous surfaces models.

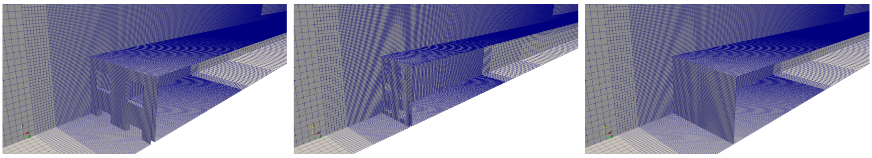

(a) (b) (c)

Figure 2.15: Adopted computational meshes: (a) *1.5 Pores*, (b) *3 Pores* and (c) *Baffle*.

An overview of the obtained instantaneous velocity fields is reported in Fig. 2.16. The strong flow separation induced by the forward facing step can be clearly observed. Overall, a very good agreement between the three cases is observed, so highlighting that the use of the pressure jumps is a viable solution not only in the case of internal flows, as classically done, but also in the case of external ones.

Furthermore, it appears that even with a small number of large pores, reasonable results can be obtained by using the pressure jump approach for this case.

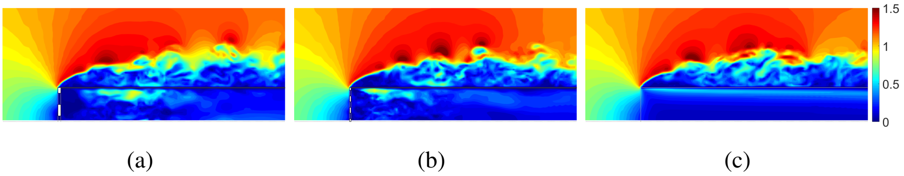

(a) (b) (c)

Figure 2.16: Contours of the non-dimensional instantaneous velocity magnitude: (a) *1.5 Pores*, (b) *3 Pores* and (c) *Baffle*.

We now proceed at characterizing the averaged fields in order to provide a direct comparison between averaged quantities in the case of *1.5 Pores* and *3 Pores* and in the *Baffle* case. In particular, time averaged quantities are denoted by means of an over-bar while averaging in the span-wise direction (the one normal to the periodic boundaries), is denoted by a subscript $,z$. The two aforementioned averaging are adopted at the same time, in order to provide quantities which are directly comparable between all considered approaches. As an example, the symbol $\bar{U}_{,z}$ indicates the time averaged velocity field, further averaged in the span-wise direction.

Still indicating with U_0 the free-stream velocity magnitude, Fig. 2.17 reports contours of $\bar{U}_{,z}/U_0$. A good correspondence between the results obtained in the three cases can be observed. Surprisingly, the recirculation region length for *1.5 Pores* appears to be more similar to the *Baffle* one than the *3 Pores* one.

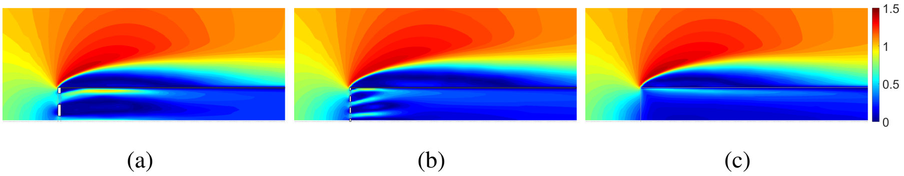

(a) (b) (c)

Figure 2.17: Contours of $\bar{U}_{,z}/U_0$ magnitude: (a) *1.5 Pores*, (b) *3 Pores* and (c) *Baffle*.

Figure 2.18 reports streamlines of $\bar{U}_{,z}/U_0$. Despite the similarity between the separation bubble length observed in *1.5 Pores* and *Baffle*, its internal organization appears to be different. In the *1.5 Pores* case, only a vortex core is clearly visible and it is followed by an elongation of the streamlines which hints to the possibility to create a second, much smaller core just downstream the first one. Conversely, in the *Baffle* case two vortex cores are clearly visible. Interestingly, the presence of an elongation of the vortex core in the horizontal direction can be seen also in the *3 Pores* case but here, despite a remarkable size difference, the two vortex cores can be clearly observed.

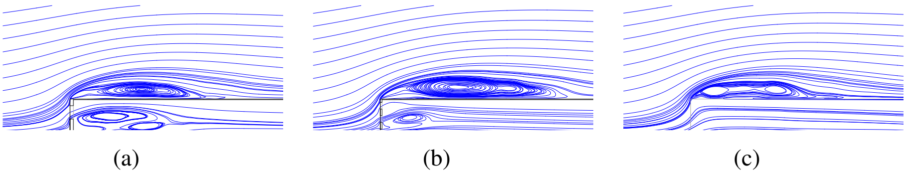
(a) (b) (c)

Figure 2.18: Streamlines of $\bar{U}_{,z}$: (a) *1.5 Pores*, (b) *3 Pores* and (c) *Baffle*.

Figure 2.19 reports contours of $\bar{C}_{p,z}$, being C_p the pressure coefficient calculated based on the free-stream velocity magnitude. The similarity in the obtained pressure fields can be clearly observed, still confirming a slightly larger separation zone for *3 Pores* with respect to the others. The pressure recovery after the grid can be once more clearly observed and, in agreement with previously presented results, appears to be completed only some holes characteristic dimensions downstream the porous grid. As expected the *Baffle* case, being representative of an infinite number of holes of vanishing size, leads to the final pressure value just downstream the porous grid.

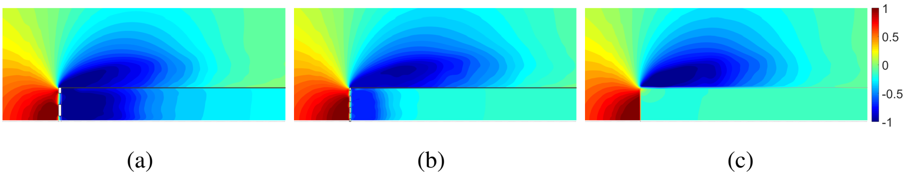

(a) (b) (c)

Figure 2.19: Contours of $\bar{C}_{p,z}$: (a) *1.5 Pores*, (b) *3 Pores* and (c) *Baffle*.

Finally, the distribution of $\bar{C}_{p,z}$ and $C'_{p,z}$ along a path running along the external side of the step (shown in Fig. 2.14 as a red line) is shown in Fig. 2.20, being $C'_{p,z}$ the standard deviation of the pressure coefficient, averaged along the span-wise direction. In particular, data are reported as a function of s, the distance along the path made non-dimensional with respect to B. A very good agreement between the three cases can be observed as regards $\bar{C}_{p,z}$ at all locations. When considering $C'_{p,z}$, it is noticed that remarkable pressure fluctuations are observed for the *1.5 Pores* case for $s < 1$ while almost null values are recorded for the *Baffle* case. The *3 Pores* case is intermediate between the two. Such differences are expected and are related to the presence of the pores and their local effects. After $s = 1$, despite some initial differences related the different internal organization of the recirculation bubble, the three simulations appear to be in fair agreement.

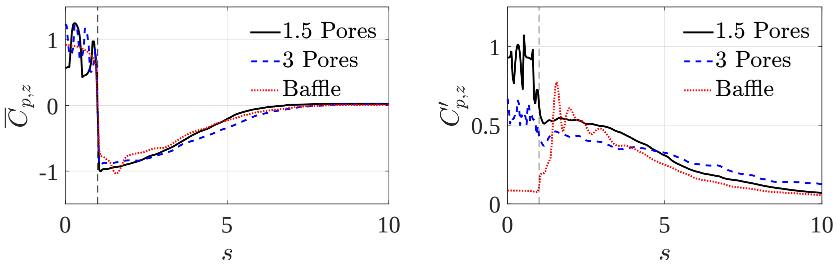

(a) (b)

Figure 2.20: Distribution of $\bar{C}_{p,z}$ and $C'_{p,z}$ along s for the three considered models.

2.6 Conclusion

In this paper, the use of the pressure jump approach for simulating the flow detachment in the proximity of a porous forward facing step has been discussed. Firstly, a brief literature review regarding existing models which can be used to relate the pressure jump to the surface porosity have been presented. Then, LES of a representative element of a porous surface has been analysed. Based on the obtained results, a new $\beta - \Delta p$ relationship, valid for thin surfaces at high Reynolds numbers, has been proposed. An investigation on the variation of the resistance offered by the grid with respect to the angle of attack has been also performed.

Finally, a forward facing step characterized by a porous frontal surface has been considered. Despite its geometrical simplicity, such case is extremely significant, as it represents the simplest of the conditions which might be found at the corners of porous bluff bodies: the flow detaches from the leading edge and reattaches along the side so creating a recirculation bubble. The pressure jump approach led to some discrepancies with respect to the cases in which the pores where explicitly simulated but, overall, reasonably good agreement between the models have been obtained, despite the fact that the considered pores were far from being of vanishing size with respect to the step height.

It must be noticed that the considered case is probably the simplest between the conditions which might be encountered in simulating the flow around porous bluff bodies, so that the present investigation actually represents only a first step toward a careful validation of the use of pressure jumps to simulate the flow around porous bluff bodies using LES.

Chapter 3

On the numerical simulation of perforated bluff-bodies: a CFD study on a hollow porous 5:1 rectangular cylinder

In this chapter, the aforementioned pressure-jump approach is evaluated by investigating the flow through a hollow porous 5:1 rectangular cylinder, where the 2D-URANS method is used. The comparisons between explicit and implicit modeling approaches are also adopted to account for the porous surfaces: in the first one the pores are explicitly modeled, so providing a detailed representation of the flow. In the second one, the porous surfaces are modeled by means of pressure jumps, which allow to take into account the presence of pores without reproducing the flow details. Then, the results obtained by using the two aforementioned techniques are compared aiming at evaluating differences and similarities, as well as identifying the main flow features which might cause discrepancies. Moreover, the influences of the turbulence model, porosity and angle of attack are considered.

This chapter has been published as:

On the numerical simulation of perforated bluff-bodies: A CFD study on a hollow porous 5:1 rectangular cylinder. M. Xu, L. Patruno, Y.L. Lo, S. de Miranda, F. Ubertini, *Wind and Structures*, 34 (2022): 1-14.

3.1 Introduction

Porous surfaces have been increasingly adopted in modern architecture over the years [1, 2, 3] (see for example Fig. 3.1). However, the aerodynamic behaviour of bluff structures composed by porous surfaces is not well-understood and it is not easily investigated by classical wind tunnel experiments, if not on relatively simple geometries [97]. An important reason is that the piping system and pressure taps are difficult to be well arranged due to the presence of the pores. In such context, Computational Fluid Dynamics, CFD, might represent an approach able to overcome the aforementioned difficulties.

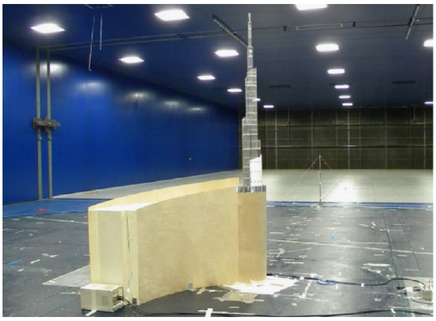

Figure 3.1: Wind tunnel test of the antenna of the Unicredit Tower performed at Politecnico di Milano. Image taken from [1].

Unfortunately, as the pore size is usually extremely small compared to the immersed porous body, performing detailed simulations of the flow through the holes leads to extremely high computational costs, which render the explicit simulation of the pores substantially impossible in the majority of the cases. A convenient alternative is to model the presence of the porous surfaces by means of appropriate pressure jumps (see for instance [31, 32]). By using such an approach, the time needed to build the numerical model and to run the simulations can be drastically reduced.

Currently, the use of pressure jumps for modelling porous surfaces is well-established for internal aerodynamics (e.g. flows through porous screens and filters). As regards external flows, similar techniques have been used to simulate the presence of actuator disks [98, 99, 100, 101, 80] and porous fences [98, 65, 31, 66]. An interesting case in which a porous medium has been adopted in order to model louvers can be found in [32]. It is noticed that the pressure-jump approach is suitable for very thin members like membranes and perforated sheets. Equivalently, for other cases in which the hydraulic head loss is distributed over the volume occupied by the permeable body, appositely defined sink terms in the momentum equation can be introduced [102, 103, 104].

However, the simulation of external flows around porous bluff-bodies by using pressure jump based simulations still requires intensive research work: the presence of flow separations and reattachments in fact renders such flows notoriously sensitive to the incoming flow characteristics and imperfections and, thus, difficult to be accurately predicted [105]. In such context, although extremely convenient in practice, the use of pressure jump based simulations should be carefully investigated before possible applications.

In this paper we aim at providing a first evaluation of the use of pressure jumps in simulating the external flow around an hollow 5:1 perforated rectangular cylinder using 2D URANS. The same case, considering solid surfaces, has been extensively studied in recent years in the context of the Benchmark on the Aerodynamics of Rectangular 5:1 Cylinder, BARC [105, 106, 107, 108, 109].

In particular, two different modeling approaches are adopted: in the first one the pores are explicitly modeled. This approach provides a detailed representation of the flow through the pores, but requires remarkable computational resources. In the second approach, the pores are not modeled and the surfaces are simulated by means of pressure jumps, which allow to take into account the presence of pores without reproducing the flow details. The agreement between the two aforementioned approaches shall not be taken for granted as the pressure jump approach represents a great simplification of the interaction between the flow and the porous element, substantially based on the matching of the drag (in analogy to many procedures used to built reduced scales models for wind tunnel experiments).

The study is thus aimed at assessing the accuracy of such second approach and qualitatively investigate the mechanisms which lead to discrepancies with respect to the first strategy. To this purpose, comparisons between such two approaches are performed considering rectangles characterized by different porosities using two turbulence models. For the case characterized by 45% porosity, different angles of attack are also considered. On such regard it should be noticed that while 2D URANS models are well-known to be sometimes inaccurate in the reproduction of the flow around bluff-bodies, the main concern here is to assess the differences between the two aforementioned approaches and to individuate the mechanisms responsible for such deviations. We furthermore notice that 2D URANS are widely used in practice (e.g. in the evaluation of the aerodynamic coefficients of bridge decks, which sometimes contain porous barriers) and that they are known to be quite successful (in the limit of their possibilities) in the prediction of the flow field around the solid 5:1 rectangular section [105].

The paper is organised as follows. The numerical setup and case geometry are illustrated in Section 3.2. The dependency of the results on the adopted mesh and on the corner geometry are investigated in Section 3.3. In Section 3.4, the aerodynamic behaviour of the rectangles characterized by several porosities are investigated at null attack angle using two turbulence models. Then, the effect of the attack angle is studied for the 45% porosity in Section 3.5. Finally, conclusions are drawn in Section 3.6.

3.2 Computational Model

In this section, the numerical setup and the geometry of the adopted porous 5:1 rectangular cylinder are reported. According to the BARC main setup and the notation introduced in Fig. 3.2, the Reynolds number based on D is set to 2.7×10^4.

As shown in Fig. 3.2 (a), the domain is such that $D_x = 40B$ and $D_y = 20B$ leading to a blockage ratio equal to 1.0%. As reported in the investigation performed by [110], very slight effects have been found when simulating the fluid flow around solid bluff-bodies if the blockage ratio ranges from 0.7% to 3.75%, which covers the value in this study. Furthermore, considering that porous bluff-bodies are investigated instead of solid ones in this work, even less remarkable influence of the blockage ratio is expected. The distance between the front surface and inlet is set to $\Lambda_x = 10B$.

As anticipated, two main approaches are used to represent the porous surfaces (also denoted as grid screens in the following), as depicted in Fig. 3.2 (b). In the first modeling approach, the geometry, which explicitly takes into account the pores is modeled. In the following, such an approach is referred as *GS*. The modelled pores are $0.05D$ wide, so trying to minimize as much as possible the ratio between their size and that of the overall rectangle. In the limit of vanishing pore size, it can be expected that the results shall be independent from the pores shape and arrangement. Different porosities are obtained by changing the pore number and, for the 65% porosity case by enlarging them to $0.125D$.

As regards to the second approach, the grid screens are replaced by homogenized baffles, i.e. the pores are not explicitly modeled and the pressure jump approach is used instead. Such modeling approach is referred as *HB* in the following sections. Additionally, a third approach is considered in which homogenized baffles are used but the corner geometry is explicitly modeled aiming at investigating the sensitivity to the corner geometry, which has been found to be of remarkable importance in the case characterized by solid surfaces [111]. Such modeling approach is referred as *SC* in the following sections. Further details on the third approach are provided in Section 3.3.

Pressure taps are arranged along the path s_0, which starts from the central point of the front surface and covers the whole rectangle, as indicated in Fig. 3.2 (a). It must be noticed that although s_0 is illustrated outside the rectangle for the sake of clarity, it is actually coincident with the surface of the rectangle. Then, in order to measure the pressure outside and inside the rectangle, pressure taps are offset in the normal direction to the path. This leads to two paths: $outside\ s_0$ and $inside\ s_0$ depending on the directions of the offset. It should be noticed that immediately downstream the porous surfaces, a pressure recovery is usually observed, as reported in [78, 112, 113]. The distance at which such pressure recovery is completed, which coincides with that required to recover an homogeneous velocity field downstream the grid, is of the order of several pore diameters. When using pressure jumps, the pore size is supposed to be a vanishing quantity, so that the pressure recovery zone dimension vanishes as well and, thus, it is not observed (for further details refer to [113]). As a consequence, in order to directly compare the *GS* and *HB* models, it is necessary to move the pressure probes away from the porous surfaces of some characteristic pore dimensions. Through a series of preliminary tests, such offsetting distance is here set to $0.15D$ (corresponding to 3 pores diameters). Such value should be regarded only as a reasonable compromise between opposing necessities: on one side it is necessary to avoid to move away from the surface where we need to evaluate the pressure field but, on the other side, we need to move out of the pressure recovery zone in order to ensure the comparability between *GS* and *HB* models [113]. We notice that P_1, P_2 and P_3 are three pressure probes located on $outside\ s_0$. Moreover, several velocity probes are arranged along s_1, s_2, s_3 and s_4, which are shown in Fig. 3.2 (b). In particular, s_3 represents the vertical midline of the rectangle.

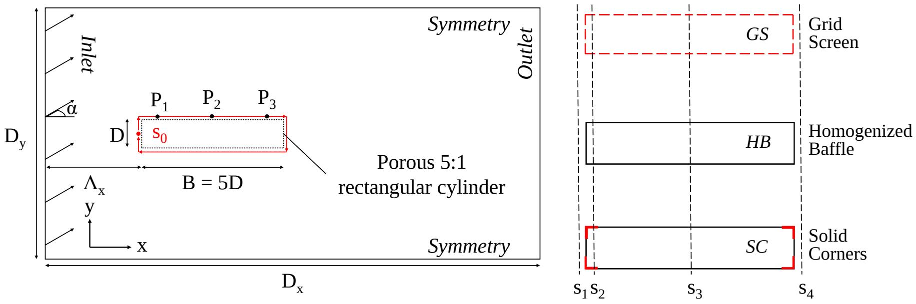

(a) (b)

Figure 3.2: Sketch of the numerical model adopted for the numerical simulations: (a) domain and (b) the porous rectangular cylinders.

As anticipated, in the modeling approaches *HB* and *SC*, the presence of the porous surfaces is described by means of pressure jumps. To this purpose, the pressure jump is calculated according to the formula provided in [113], which reads

$$\Delta p = \frac{\rho U_n^2}{2} \frac{(a_1\beta + 2)(\beta - 1)}{\beta^2(a_2 - 1)}, \tag{3.1}$$

where Δp is the pressure jump, β is the porosity defined by the pore area divided by the total surface area, ρ is the fluid density, U_n is the local velocity normal to the surface, $a_1 = 0.5$ and $a_2 = -0.1$. Such formula is valid at high Reynolds for perforated plates of vanishing thickness and has been validated against experimental and numerical data for porosities in the range 16% to 69% [113]. Other formulations and corrections able to account for different situations can be found in [79, 77, 86, 87, 88, 89, 90, 91, 92].

In this paper, two well-known URANS turbulence models are adopted. The first one is the $k-\omega$ sst model, which has been extensively used in the context of bluff-bodies aerodynamics [114, 115, 116, 117]. As reported in [118], the $k-\omega$ sst model is a blend between the $k-\omega$ model in the near-wall region and the $k-\varepsilon$ model in the far field. Such a transition is regulated by the wall distance. Unfortunately such quantity is not well defined for porous surfaces when homogenized baffles are adopted. In order to avoid such problem, the Shih's quadratic algebraic Reynolds stress $k-\varepsilon$ model is also considered, [119], because it is wall-distance-free. This characteristic appears to be an advantage in such a context. For the sake of conciseness, the aforementioned turbulence models are referred as $k-\omega$ and $k-\varepsilon$ in the following sections, respectively.

As regards to the boundary conditions, a zero pressure is imposed at the outlet boundary, while a null pressure gradient is prescribed at the inlet. A fixed velocity value, $U_0 = 2m/s$, is imposed at the inlet boundary, and a Neumann boundary condition, zero gradient, is imposed at the outlet. Symmetry boundary conditions are imposed at the top and bottom of the domain while wall-functions are used for the grid for GS models.

A centered second-order differentiation scheme is adopted for the diffusive terms, while for non-linear advective terms, the second-order linear upwind scheme is used. Time integration is performed by using the Crank-Nicolson scheme. The coupling of pressure and velocity is obtained for all simulations by using the well known Pressure-Implicit with Splitting of Operators (PISO) algorithm. The open source Finite Volume software OpenFOAM is adopted to perform the simulations.

3.3 Sensitivity to mesh and corner geometry

In this section, the dependency of results on the adopted mesh is firstly discussed. Then, the influence of the corner geometry on the fluid flow is investigated. Such assessments have been performed considering a rectangle characterized by 45% porosity.

3.3.1 Sensitivity to mesh

Two structured meshes are used in order to assess the sensitivity to the mesh. The first one, a coarse mesh, C, characterized by along and cross wind dimensions $\delta_x/B = \delta_y/B = 5\times10^{-3}$ close to the considered rectangle, is adopted and shown in Fig. 3.3. The second one, a finer mesh, F, characterized by along and cross wind dimensions $\delta_x/B = \delta_y/B = 2.5\times10^{-3}$ close to the considered rectangle, is also used. By adopting the meshes C and F for the 45%-porosity rectangle, each pore is meshed by 4 and 8 cells, respectively. We remark that each solid part for the *GS* model might be regarded as an independent bluff body, so that an accurate simulation would require thousands of cells for each of them. However, such a large effort appears to be unjustified also in view of the fact that the *HB* models only roughly approximate the presence of porous surfaces disregarding any effect other than the resistance offered in the direction normal to the porous surface (i.e. no shearing effect is taken into account, nor local pore-scale flow modifications, turbulence production, etc).

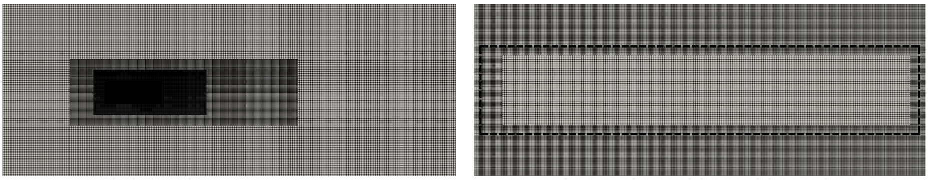

(a)

(b)

Figure 3.3: The coarse mesh adopted for the 2D RANS simulations: (a) overview and (b) the porous 5:1 rectangular cylinder used for the *GS* model.

We now proceed at comparing the time-averaged fields obtained with the meshes C and F. Firstly, the dimensionless time-averaged velocity, $\overline{U}/U_0$, along s_1, s_2, s_3 and s_4 is shown in Fig. 3.4. In particular, looking at the results of *GS* models shown Fig. 3.4, it can be seen that some differences between *GS C* and *GS F* are observed especially in correspondence of the pores of the frontal face but, overall, a good agreement is obtained. As regards the *HB* models, the distributions of $\overline{U}/U_0$ appear not to be significantly affected by the mesh resolution. We notice that the differences observed between *GS C* and *GS F* models do not allow to explain qualitative differences with respect to *HB* models. Between them, we observe a smoother distribution of the velocity in front of the rectangle (i.e. path s_1) for the *HB* model as well as different shapes of the velocity profile at the leeward edge (i.e. path s_4).

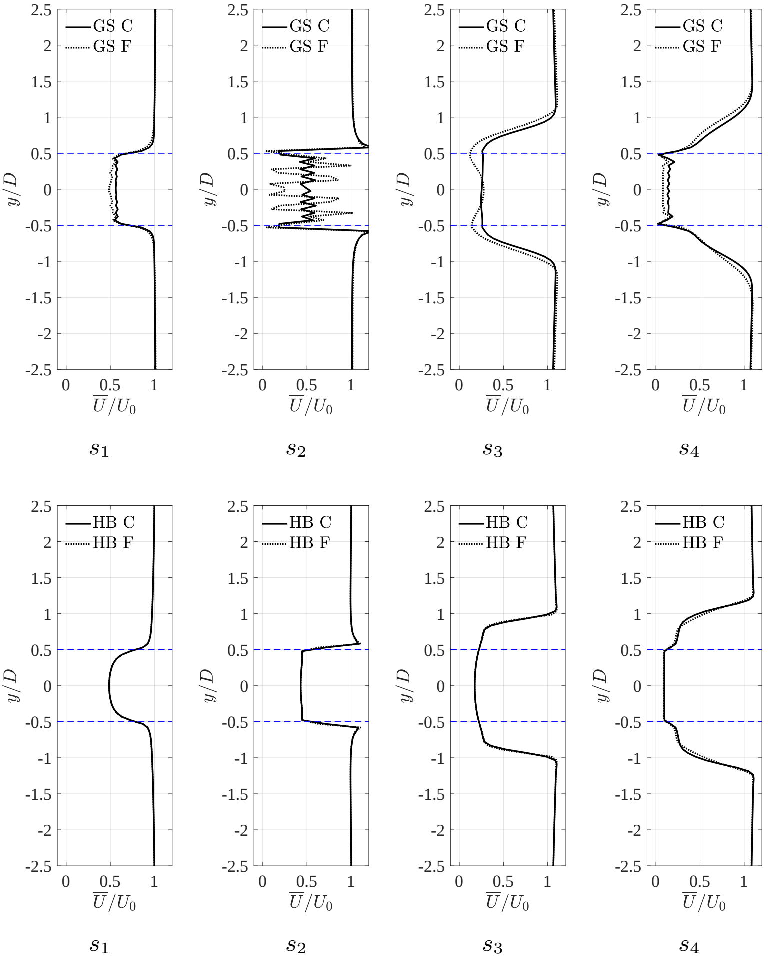

s_1 s_2 s_3 s_4

s_1 s_2 s_3 s_4

Figure 3.4: The $\overline{U}/U_0$ along the s_1, s_2, s_3 and s_4 of *GS* and *HB*, where C and F represent the coarse and finer mesh, respectively.

As usual, we define the time-averaged pressure coefficient, $\overline{C}_p = \frac{\overline{p}}{\frac{1}{2}\rho U_0^2}$, where $\overline{p}$ represents the time-averaged pressure. A reasonable agreement between $GS\ C$ and $GS\ F$ is observed, although a slight mesh sensitivity can be noticed as shown in Fig. 3.5. Actually, as already mentioned, each pore is meshed by 4 to 8 cells, so that some local mesh dependency can be expected. Indeed, this shows that even in such a simple case, obtaining a clear mesh independence when considering the pores geometry is extremely difficult, so further highlighting the importance of investigating the use of *HB* models. Nevertheless, it should be noticed that a good agreement as regards the overall flow arrangement is obtained, which suggests that the adopted mesh resolutions are adequate for the current study.

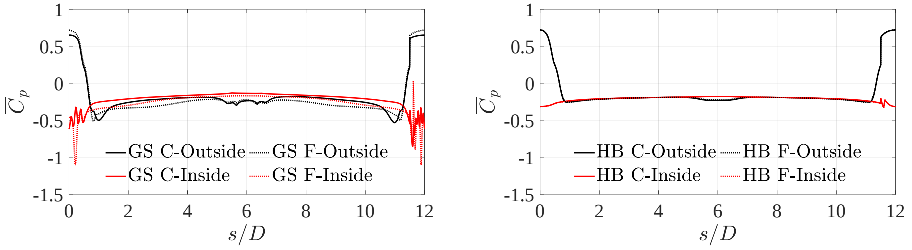

(a) (b)

Figure 3.5: Comparisons of the $\overline{C}_p$ obtained by using C and F meshes: (a) GS models and (b) HB models.

With the aim of obtaining a better insight in the slight mesh sensitivity observed for *GS* models, we now look at the instantaneous velocity field, U, reported in Fig. 3.6. In particular, it can be seen that vortical structures detached at the leading edge corners appear to be stronger when the coarse mesh is adopted. This seems to indicate that the local flow behaviour at the corner is the main cause of the differences observed between *GS C* and *GS F* models.

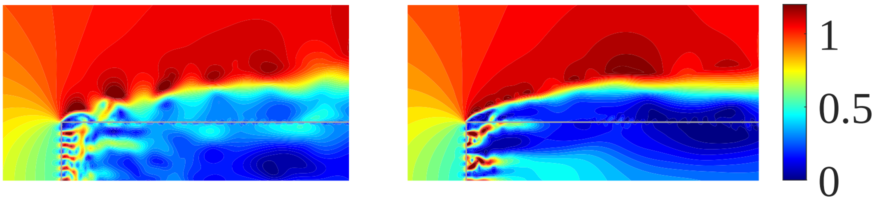

GS C *GS F*

Figure 3.6: Contours of the magnitude of U/U_0 around the top windward corner, where C and F represent the coarse and finer mesh, respectively.

The aforementioned differences become less noticeable in the distributions of time-averaged velocity magnitude, which is shown in Fig. 3.7. Such improvement indicates that although the detailed flow arrangement cannot be well reproduced, comparable patterns of the time-averaged velocity magnitude are obtained.

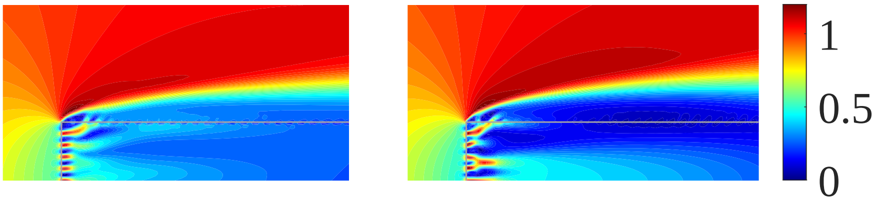

GS C *GS F*

Figure 3.7: Contours of the magnitude of $\overline{U}/U_0$ around the top windward corner, where C and F represent the coarse and finer mesh, respectively.

Also anticipated in Fig. 3.5, comparable distributions of time-averaged pressure can be observed around the windward corner as well. However, differences between *GS C* and *GS F* models are noticed downstream the windward corner.

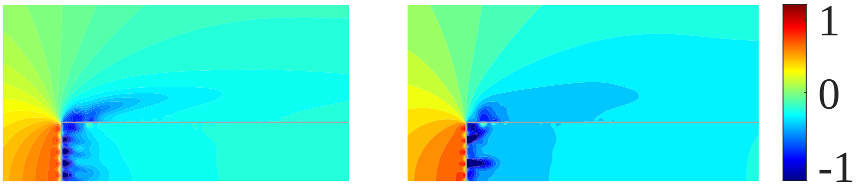

GS C *GS F*

Figure 3.8: Contours of time-averaged pressure around the top windward corner, where C and F represent the coarse and finer mesh, respectively.

The module of the Fast Fourier Transform (FFT) of the pressure measured at P_1, P_2 and P_3 is shown in Fig. 3.9. In particular, at P_1, *GS C* shows a peak at a non-dimensional frequency, $f/(B/U_0)$, equal to 10, which is not observed for *GS F*. At P_3 a peak is present at approximately 2, and the *GS C* and the *GS F* lead to comparable results. Such evidences appear to be consistent with the U field shown in Fig. 3.6, where several vortex detached at the leading edge can be observed only when the coarse mesh is adopted, but a global shedding mechanism is obtained for both models as it will be later shown.

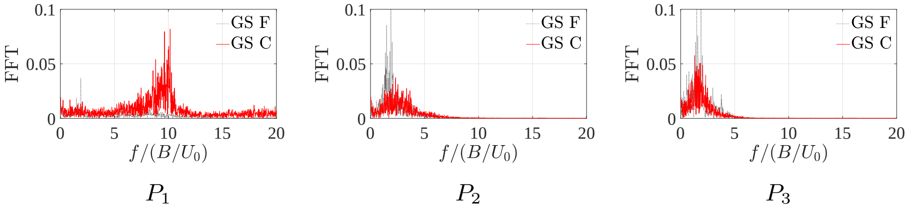

P_1 P_2 P_3

Figure 3.9: The Fast Fourier Transform (FFT) of pressure at the P_1, P_2 and P_3 of *GS* with coarse and finer mesh (C: coarse mesh, F: finer mesh). The frequency is dimensionless based on B and U_0.

Summarizing, a good agreement between *GS C* and *GS F* in terms of overall flow arrangement is observed. Differences are recorded mainly in the proximity of the holes and of the leading edge corners. Such differences, which can be considered as mainly local, are responsible for some differences in the flow arrangement and appear to be difficult to be completely eliminated.

3.3.2 Sensitivity to corner geometry

It has been observed in the previous section that the corner zone is particularly sensitive to the adopted mesh due to local effects. This indeed suggests a sensitivity also to the corner geometry. While this might not represent a major problem for pores of vanishing size, it is anyway worth to investigate such effects a little bit further. Once again the analysis is performed taking into account only the 45%-porosity rectangle, representative of intermediate porosities between the investigated ones.

In particular, in this section we analyze the possibility to build mixed *GS/HB* models. Such investigation is performed by adopting the *SC* models, which use the *HB* approach in all the body apart from the corners, where the geometry is explicitly modeled as in *GS* models. This provides a hybrid approach between *GS* and *HB*, and we here investigate the sensitivity of such model with respect to the corner geometry (in the spirit of a sensitivity study the *C* mesh has been retained). For this purpose, three types of corner geometries are simulated, which are shown in Fig. 3.10: in the first corner geometry, denoted as *SC00*, only the solid part of the corner is explicitly modeled; in the second one, *SC13*, one hole on the front surface and three holes on the sides are explicitly modeled; in the third one, *SC23*, two holes on the front surface and three holes on the sides are explicitly modeled.

The magnitude of the instantaneous velocity field obtained adopting the three aforementioned models is shown in Fig. 3.11. It can be seen that the flow detachment is affected by the corner geometry. In particular, comparing *SC13* and *SC23* shows that the geometry of the pores on the windward as well as the side surface is responsible for the flow arrangement, being the interaction between the two the cause of the observed shedding of small vortical structures.

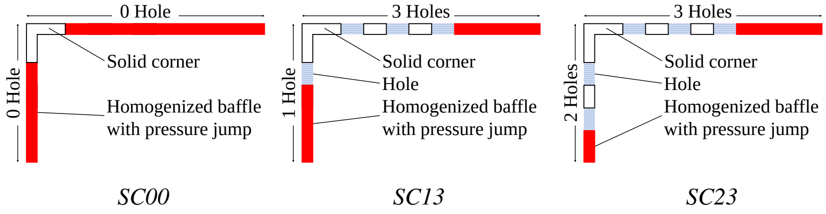

Figure 3.10: The adopted corner geometries for the *SC* modeling approach, in the sketch the thickness of the porous surface is not null but a null thickness has been used in the numerical models.

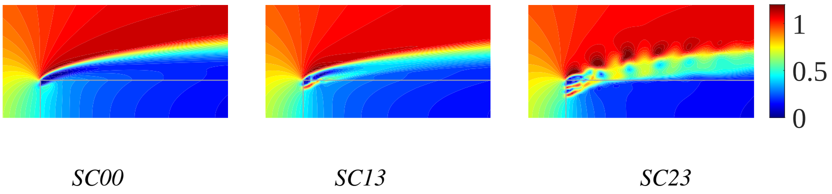

Figure 3.11: Contours of the magnitude of U/U_0 obtained by using different corner geometries.

As expected, as it can be seen in Fig. 3.12, the pressure coefficients along $outside\ s_0$ and $inside\ s_0$ are also affected by the corner geometry, although such influence is mostly concentrated in the proximity of the corners. Results obtained for the model *SC23* are indeed quite similar to the *GS* model in the proximity of the corner.

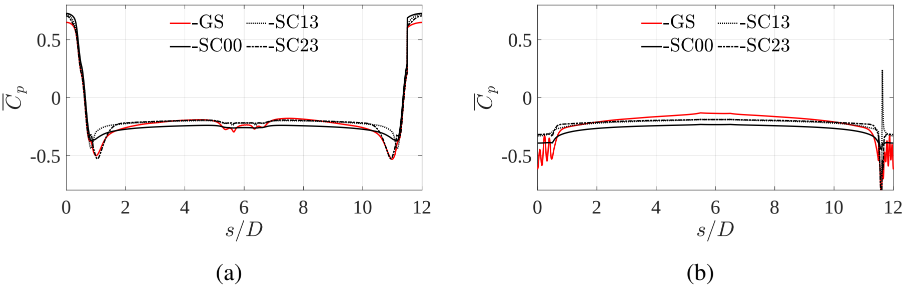

Figure 3.12: The distributions of the pressure coefficients along (a): $outside\ s_0$ and (b): $inside\ s_0$.

In a brief summary, the influence of the corner geometry might represent a limitation of the current investigation. We nevertheless assume that such differences vanish for vanishing pores dimensions with respect to the immersed body. Such aspect, worth of further investigations, remarkably complicates the direct comparison of *GS* and *HB* models when pores are not of vanishing size. It also appears that the local flow at the corner is influenced by a relative large number of pores in its proximity.

Due to the great simplifications given by the *HB* models, assessing their performances with respect to *GS* models appears to be of primary practical importance and, so, we proceed conscious of the unavoidable limitations of such comparison. We notice that a viable alternative is to compare CFD results against experimental ones obtained with pores of very small size. Unfortunately, producing such experimental results is remarkably difficult and, in addition, the comparison would not allow to properly isolate the effect of using pressure jumps instead of explicitly modelling the geometry (i.e. many other aspects concur in producing the differences observed between 2D URANS and experimental results).

3.4 The effect of porosity

In this section, the numerical results obtained with three porosities (i.e. $\beta = 25\%$, $\beta = 45\%$ and $\beta = 65\%$) and two turbulence models (i.e. $k - \varepsilon$ and $k - \omega$) are analyzed. It should be noticed that the results reported for the *GS* models are actually obtained by using the $k - \varepsilon$ turbulence model. The same simulations have been also performed by using the $k - \omega$ turbulence model obtaining very similar results. These results are not shown here for the sake of conciseness and, consequently, when the $k - \varepsilon$ and $k - \omega$ models are mentioned in the following sections, only the *HB* models are referred.

3.4.1 Flow topology

Before proceeding, for the sake of comparison, we here briefly report results obtained for the fully solid case, i.e. $\beta = 0$, presented in [117]. Such results, in analogy to the current ones for the porous cases, are obtained using 2D URANS simulations. In particular, Fig. 3.13 reports contours of the instantaneous velocity magnitude and streamlines.

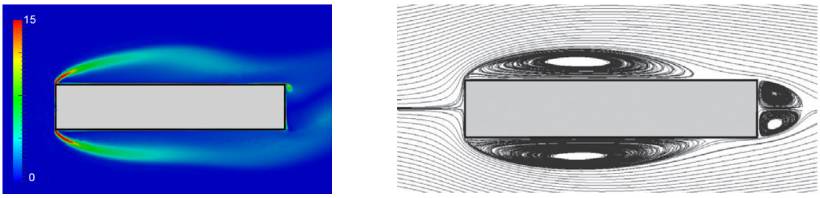

(a) (b)

Figure 3.13: The flow topology around the solid 5:1 rectangle at null angle of attack reported by [117]: (a) the contours of U and (b) time-averaged streamline.

We now proceed at comparing the instantaneous velocity fields obtained by using different porosities and turbulence models, which are shown in Fig. 3.14. Looking at the *GS* models shown in Fig. 3.14, a change of the overall flow organization is observed with increasing porosity. In particular, vortex shedding occurs for 25% porosity, while only minor shear layer instabilities are found for $\beta = 65\%$ when the *GS* model is adopted. We further notice that a reasonable agreement between $k - \varepsilon$ and $k - \omega$ turbulence models is obtained for $\beta = 25\%$ and $\beta = 65\%$. On the contrary, for the intermediate porosity, i.e. 45%, vortex shedding is observed for the GS and the *HB* $k - \varepsilon$ models, while it is not observed for the *HB* $k - \omega$ model.

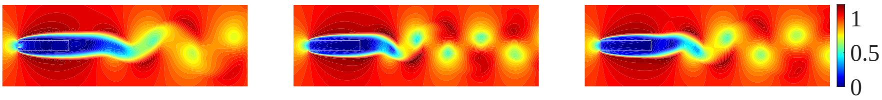

GS, $\beta = 25\%$ *HB*, $k - \varepsilon$, $\beta = 25\%$ *HB*, $k - \omega$, $\beta = 25\%$

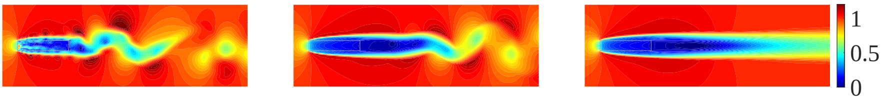

GS, $\beta = 45\%$ *HB*, $k - \varepsilon$, $\beta = 45\%$ *HB*, $k - \omega$, $\beta = 45\%$

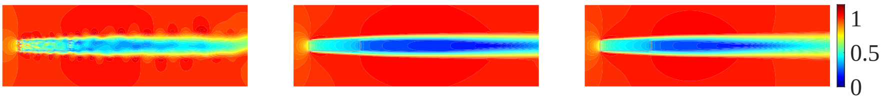

GS, $\beta = 65\%$ *HB*, $k - \varepsilon$, $\beta = 65\%$ *HB*, $k - \omega$, $\beta = 65\%$

Figure 3.14: Contours of the magnitude of U/U_0 obtained by using different modeling approaches, porosities and turbulence models.

Similar phenomena can be also found in the distributions of instantaneous pressure (3.15): when comparing the $k - \varepsilon$ and $k - \omega$ models, for the 25%- and 65%-porosity cases, comparable vortex shedding are found in the wake flow. However, for the 45%-porosity cases, the vortex street is observed only in $k - \varepsilon$ cases.

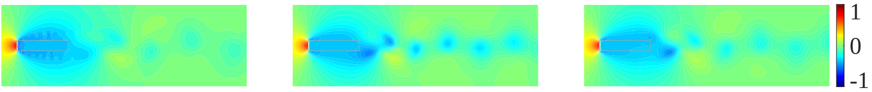

GS, $\beta = 25\%$ *HB*, $k - \varepsilon$, $\beta = 25\%$ *HB*, $k - \omega$, $\beta = 25\%$

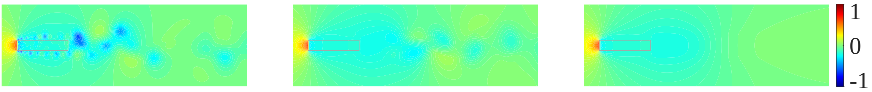

GS, $\beta = 45\%$ *HB*, $k - \varepsilon$, $\beta = 45\%$ *HB*, $k - \omega$, $\beta = 45\%$

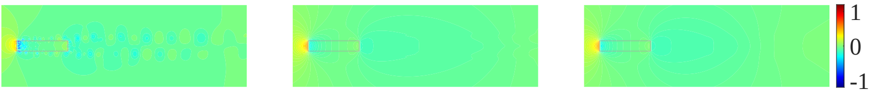

GS, $\beta = 65\%$ *HB*, $k - \varepsilon$, $\beta = 65\%$ *HB*, $k - \omega$, $\beta = 65\%$

Figure 3.15: Contours of instantaneous pressure, p/p_0, obtained by using different modeling approaches, porosities and turbulence models.

With respect to the time-averaged flow arrangements, the difference between $k-\varepsilon$ and $k - \omega$ turbulence models is even less noticeable. Moreover, such agreement is observed regardless the adopted porosity.

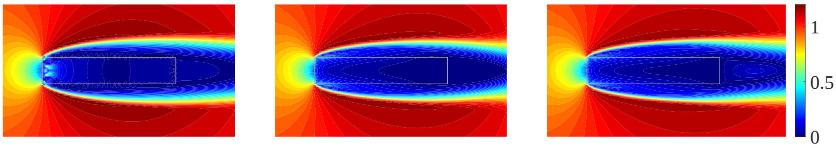

GS, $\beta = 25\%$ *HB*, $k - \varepsilon$, $\beta = 25\%$ *HB*, $k - \omega$, $\beta = 25\%$

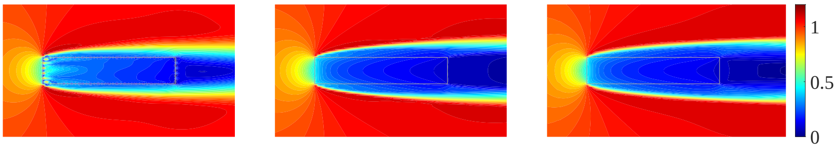

GS, $\beta = 45\%$ *HB*, $k - \varepsilon$, $\beta = 45\%$ *HB*, $k - \omega$, $\beta = 45\%$

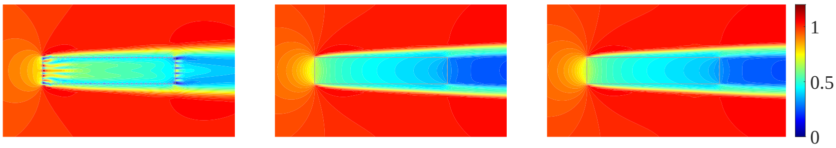

GS, $\beta = 65\%$ *HB*, $k - \varepsilon$, $\beta = 65\%$ *HB*, $k - \omega$, $\beta = 65\%$

Figure 3.16: Contours of the magnitude of $\overline{U}/U_0$ obtained by using different modeling approaches, porosities and turbulence models.

As shown in Fig. 3.17, such consistency is also found in the comparison of time-averaged pressures, where the patterns of $k - \varepsilon$ and $k - \omega$ models are particularly comparable. However, several differences between *GS* and *HB* models are noticed as well. As anticipated, the pressure recovery cannot be reproduced by using the *HB* approach, which consequently leads to different pressure distributions downstream the windward surface.

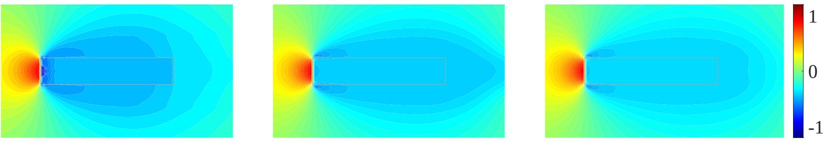

GS, $\beta = 25\%$ *HB*, $k - \varepsilon$, $\beta = 25\%$ *HB*, $k - \omega$, $\beta = 25\%$

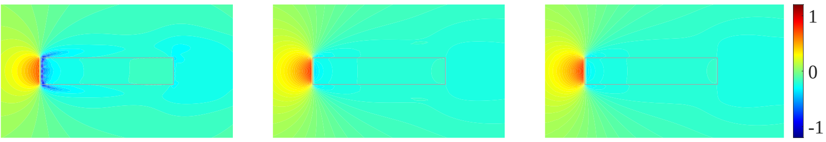

GS, $\beta = 45\%$ *HB*, $k - \varepsilon$, $\beta = 45\%$ *HB*, $k - \omega$, $\beta = 45\%$

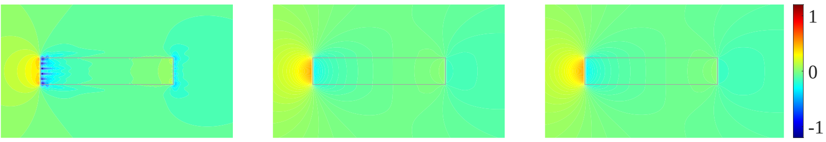

GS, $\beta = 65\%$ *HB*, $k - \varepsilon$, $\beta = 65\%$ *HB*, $k - \omega$, $\beta = 65\%$

Figure 3.17: Contours of the time-averaged pressure, $\overline{p}/p_0$, obtained by using different modeling approaches, porosities and turbulence models.

Finally, looking at the time-averaged streamlines shown in Fig. 3.18, we can notice that the recirculations in the wake zone are clearly identifiable for 25% porosity. In particular, differently from the solid case, no separation bubble is created on the sides at the leading edge, where the separation if filled by the outflow coming from the interior of the rectangle, which prevents vorticity accumulation there. Looking now at the back surfaces, the 25%-porosity *GS* model is characterized by two vortices partially included inside the rectangle, while such arrangement is not observed in either *HB* models. Despite these differences, the mean flows of the *GS* models appear to be well reproduced by the *HB* models when porosities are larger. Overall, the $k - \varepsilon$ and $k - \omega$ turbulence models provide similar mean flow regardless the porosity.

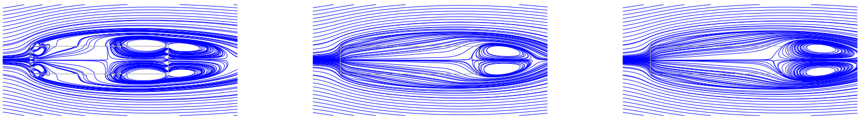

GS, $\beta = 25\%$ *HB*, $k - \varepsilon$, $\beta = 25\%$ *HB*, $k - \omega$, $\beta = 25\%$

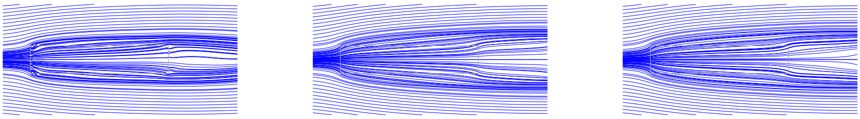

GS, $\beta = 45\%$ *HB*, $k - \varepsilon$, $\beta = 45\%$ *HB*, $k - \omega$, $\beta = 45\%$

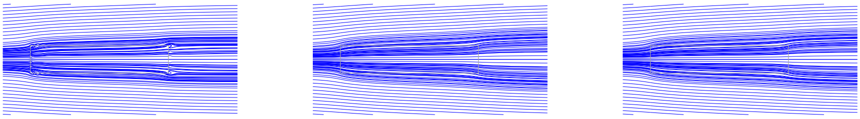

GS, $\beta = 65\%$ *HB*, $k - \varepsilon$, $\beta = 65\%$ *HB*, $k - \omega$, $\beta = 65\%$

Figure 3.18: The streamlines of $\overline{U}$ obtained by using different modeling approaches, porosities and turbulence models.

3.4.2 Statistics of velocity and pressures

Firstly, the distributions of $\overline{U}/U_0$ along s_1 to s_4 are reported in Fig. 3.19. Looking at the $\overline{U}/U_0$ along s_1, which is located just upstream the front surface, several fluctuations can be noticed in the results of the *GS* models due to the presence of the pores but a reasonable agreement is observed if those fluctuations are disregarded. Focusing on the results along s_1 and s_2, the velocities in the central point, $y/D = 0$, are approximately equal to βU_0: for *HB* models and 25% porosity, the velocity in the central point is approximately equal to 28% of the U_0; for 45% porosity, the velocity in the central point is approximately equal to 48% of the U_0; for 65% porosity, the velocity in the central point is approximately equal to 70% of U_0.

The model characterized by $\beta = 25\%$ seems to provide the best agreement between *GS* and *HB* models, while $\beta = 45\%$ and $\beta = 65\%$ show the largest discrepancies. We nevertheless observe that the widths of the zones where the $\overline{U}/U_0$ is sensibly smaller than 1.0, i.e. the zones whose velocity is shielded by the presence of the porous rectangle, are similar in cross-wind size for all the *GS* and *HB* models.

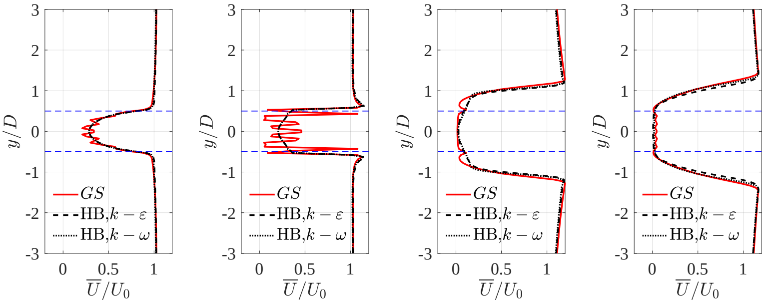

s_1 with $\beta = 25\%$ s_2 with $\beta = 25\%$ s_3 with $\beta = 25\%$ s_4 with $\beta = 25\%$

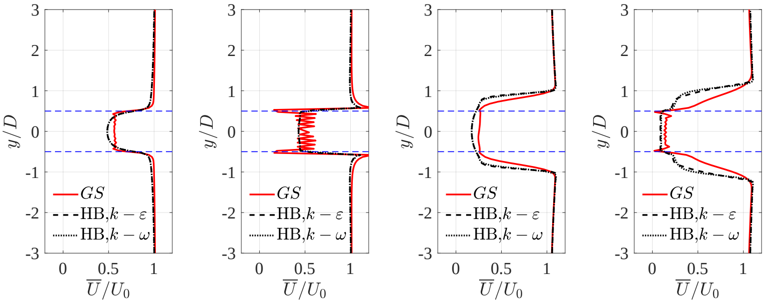

s_1 with $\beta = 45\%$ s_2 with $\beta = 45\%$ s_3 with $\beta = 45\%$ s_4 with $\beta = 45\%$

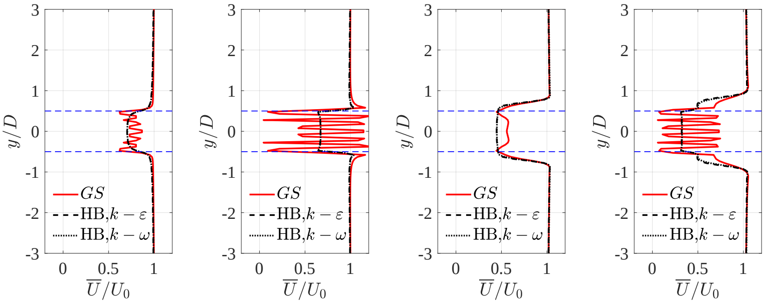

s_1 with $\beta = 65\%$ s_2 with $\beta = 65\%$ s_3 with $\beta = 65\%$ s_4 with $\beta = 65\%$

Figure 3.19: The $\overline{U}/U_0$ of the *GS* and *HB* models along s_1, s_2, s_3 and s_4.

Secondly, the pressure coefficients of the *GS* and *HB* models are reported in Fig. 3.20 where, for the sake of completeness, results for the solid cases reported in [117] are also shown. In the comparison between the solid case and the porous cases, it should be bear in mind that the solid case is measured right on the surface, while porous cases are measured at offset locations.

Observing the $\overline{C}_p$ along the $outside\ s_0$, it can be seen that the overall results are comparable, while the major discrepancies are noticed in different regions depending on the adopted porosity. When the 25% porosity is adopted the pressure outside the windward face is well captured but suctions in the inner face appear underestimated. This is at least partially due to an incomplete pressure recovery in that zone and should not be overestimated. Looking now at the outside paths, the same observation holds for the results obtained for the leeward face of the 65% porosity rectangle. The effects of the leeward corners, not accurately captured by *HB* models, appear to be particularly remarkable at intermediate porosities. Overall, it can be concluded that a good qualitative agreement is obtained by *HB* models which, anyway, struggle to catch local effects which, once amplified downstream, might lead to some differences in the overall results.

Furthermore, it can be seen that the $k - \varepsilon$ and $k - \omega$ models provide similar $\overline{C}_p$ for the *HB* models regardless the porosity. As previously explained, such result is not trivial as the wall-distance is not properly defined for *HB* models.

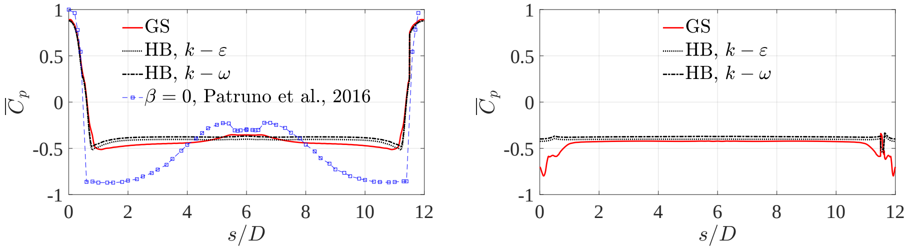

$\beta = 25\%$, *outside* s_0 $\beta = 25\%$, *inside* s_0

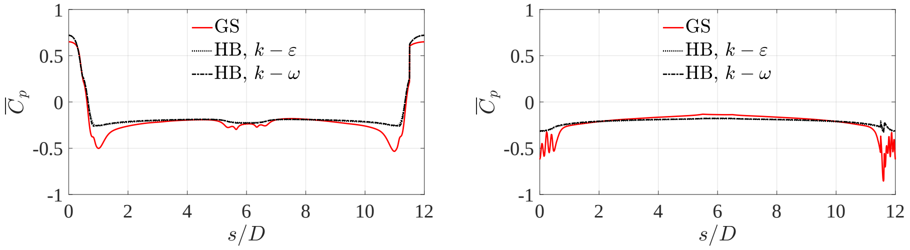

$\beta = 45\%$, *outside* s_0 $\beta = 45\%$, *inside* s_0

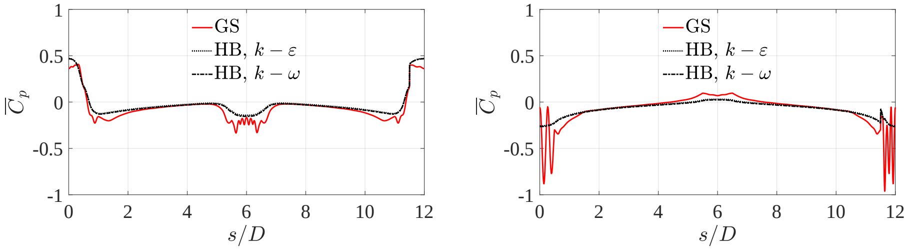

$\beta = 65\%$, *outside* s_0 $\beta = 65\%$, *inside* s_0

Figure 3.20: The $\overline{C}_p$ of the *GS* and *HB* models with offset distance $0.15D$.

In the previous discussions, as anticipated, pressures are measured offsetting the path s_0 of a distance $0.15D$. In order to highlight the influence of the pressure recovery, a distance, $0.03D$ is also considered, and the obtained results are shown in Fig. 3.21. Such distance is such that no pressure recovery can actually take place and so, stronger suctions are expected downstream the porous surfaces (i.e. the suctions of *GS* and *HB* models should not be directly compared). By comparing the results shown in Fig. 3.20 and Fig. 3.21, as expected it can be seen that differences are mainly observed downstream the front and back surfaces, where the pressure recovery occurs, which means that the pressure here is still to be recovered from the dynamic head.

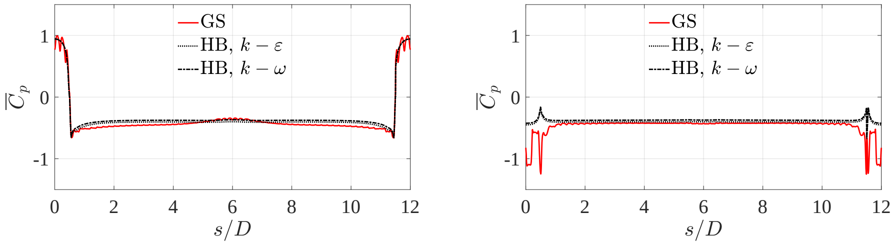

$\beta = 25\%$, *outside* s_0 $\beta = 25\%$, *inside* s_0

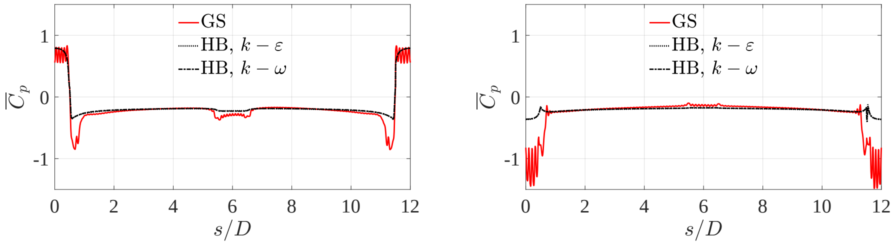

$\beta = 45\%$, *outside* s_0 $\beta = 45\%$, *inside* s_0

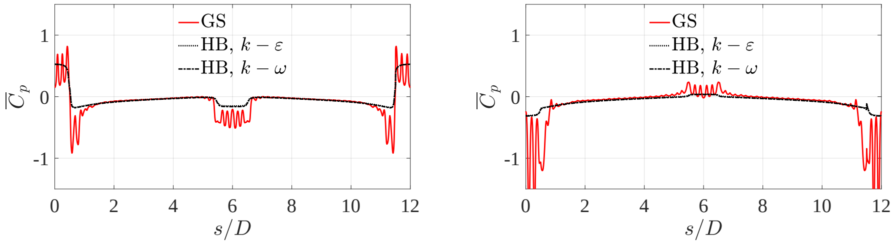

$\beta = 65\%$, *outside* s_0 $\beta = 65\%$, *inside* s_0

Figure 3.21: The $\overline{C}_p$ of the *GS* and *HB* models when a small distance from the porous surfaces, $0.03D$, is adopted to offset the path s_0.

Then, the root mean square of the pressures along *outside* s_0 and *inside* s_0 is reported in Fig. 3.22. Here differences between *GS* and *HB* models can be clearly seen. Pressure fluctuations are observed for the *HB* models only for 25% porosity. In all other cases, *HB* models are characterized by very small fluctuations. This happens also for *HB* $\beta = 45\%$ when $k-\varepsilon$ is used, which is characterized by vortex shedding. In that case, the shedding is actually observed far down in the wake and leads only to very weak fluctuations at the body surface. In making such comparisons it should be anyway recalled that in no way the local pressure fluctuations around the pores can be replicated by the adopted *HB* model. This is particularly obvious for the 65%-porosity cases shown in Fig. 3.22, which are representative of the cases in which global vortex shedding does not occur for the *GS* model with $\beta = 65\%$ (shown in Fig. 3.14), but pressure fluctuations are anyway clearly observed.

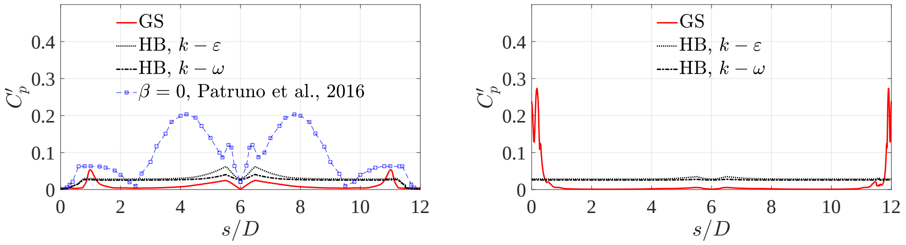

$\beta = 25\%$, *outside* s_0 $\beta = 25\%$, *inside* s_0

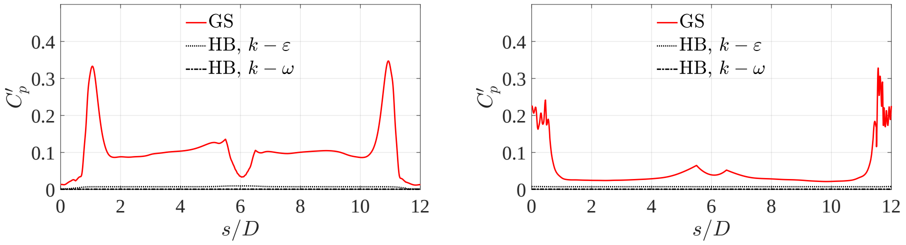

$\beta = 45\%$, *outside* s_0 $\beta = 45\%$, *inside* s_0

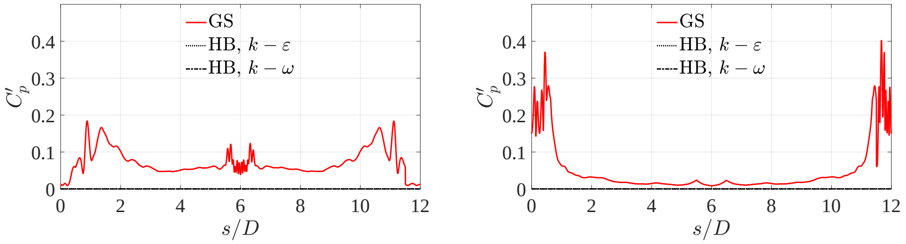

$\beta = 65\%$, *outside* s_0 $\beta = 65\%$, *inside* s_0

Figure 3.22: The C'_p of the *GS* and *HB* models when the distance, $0.15D$, is adopted to offset the path s_0.

Finally, integral force coefficients (normalized by the cylinder breadth, B) and their standard deviations are shown in Table 3.1. It can be seen that, at least in the present simulations, introducing porosity does not have a strong effect on the drag coefficient, being the *GS* and *HB* models in agreement on such point.

Strong differences instead are observed in the fluctuations of the lift coefficient, as the introduction of porosity suppresses of strongly limits the strength of vortex shedding, as already discussed.

Table 3.1: The integral force coefficients (normalized by the cylinder breadth, B) and standard deviations for the *GS* and *HB* models. A solid case, $\beta = 0$, reported by [117] is also shown.

	C_d			C'_d		
	GS	*HB*,$k-\varepsilon$	*HB*, $k-\omega$	*GS*	*HB*,$k-\varepsilon$	*HB*, $k-\omega$
$\beta = 0$, [117]	0.224	-	-	0.018	-	-
$\beta = 25\%$	0.245	0.253	0.247	0.015	0.003	0.005
$\beta = 45\%$	0.251	0.234	0.231	0.009	7.0×10^{-4}	1.5×10^{-7}
$\beta = 65\%$	0.215	0.207	0.209	0.004	5.3×10^{-7}	4.5×10^{-9}

	C_l			C'_l		
	GS	*HB*,$k-\varepsilon$	*HB*, $k-\omega$	*GS*	*HB*,$k-\varepsilon$	*HB*, $k-\omega$
$\beta = 0$, [117]	-0.02	-	-	0.81	-	-
$\beta = 25\%$	-9.2×10^{-5}	3.5×10^{-5}	9.8×10^{-6}	0.01	0.008	0.005
$\beta = 45\%$	2.0×10^{-3}	6.0×10^{-8}	-5.6×10^{-11}	0.015	1.1×10^{-5}	3.5×10^{-10}
$\beta = 65\%$	2.0×10^{-4}	3.3×10^{-10}	-4.0×10^{-11}	0.039	6.0×10^{-5}	6.7×10^{-12}

In a summary, *GS* and *HB* models appear to be comparable as regards the overall time-averaged flow organization, but may differ in many aspects related to the local flow organization. As local differences can be amplified downstream, they indeed lead to some differences in the obtained results. Local differences are mainly related to the corners and to the unavoidable presence of pressure recovery zones for *GS* models which cannot be appreciated in *HB* models. Such last aspect might not be of practical importance in many circumstances as such zones are expected to vanish in size for vanishing pore dimensions but increases the difficulties encountered in comparing *GS* and *HB* models. It should also be noticed that the C'_p appears to be hard to be well reproduced by using the *HB* models, but this can be partially attributed to the presence of the aforementioned local effects which the such models are meant to smooth out.

3.5 Effect of the attack angle

In this section, the numerical results obtained with the 45%-porosity rectangles considering two additional attack angles are analyzed (i.e. $\alpha = 30^\circ$ and $\alpha = 60^\circ$ nose-up, see Fig. 3.2). The different attack angles have been obtained rotating the inflow velocity and adopting periodic conditions on the top and bottom of the domain. Since the influence of the adopted turbulence models on the results has been found to be negligible, only the results of the $k - \varepsilon$ model are here reported for the sake of conciseness.

Firstly, the distributions of the time-averaged velocity along s_1, s_2, s_3 and s_4 are illustrated in Fig. 3.23. It should be noticed that the adopted attack angles are such to considerably change the orientation of the s_1 to s_4 with respect to the mean flow. Such paths have been anyway maintained for the sake of simplicity. Results obtained in the previous sections are mainly confirmed being the *GS* and *HB* models in reasonable agreement when the fluctuations induced by the presence of the pores are disregarded. In particular, trends appear to be well reproduced as well as the extension of the zones shielded by the presence of the porous rectangle.

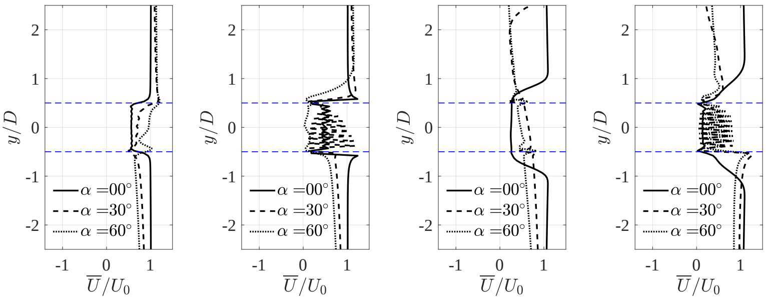

s_1 for *GS* s_2 for *GS* s_3 for *GS* s_4 for *GS*

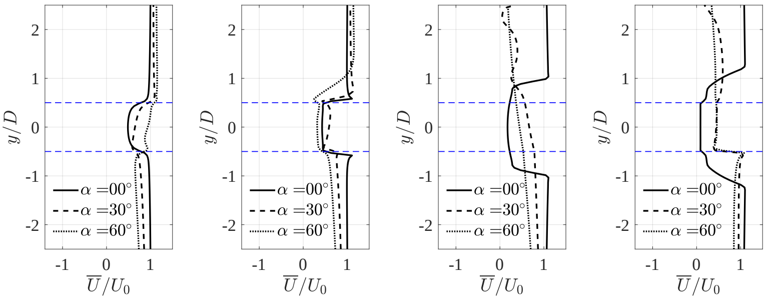

s_1 for *HB* s_2 for *HB* s_3 for *HB* s_4 for *HB*

Figure 3.23: The $\overline{U}/U_0$ of the *GS* and *HB* models obtained by using different attack angles.

The time-averaged pressure coefficients are reported in Fig. 3.24. Also in this case, although some quantitative difference is observed, results appear to be well comparable, being the time-averaged pressure distribution at $\alpha = 60°$ very well reproduced by the *HB* model.

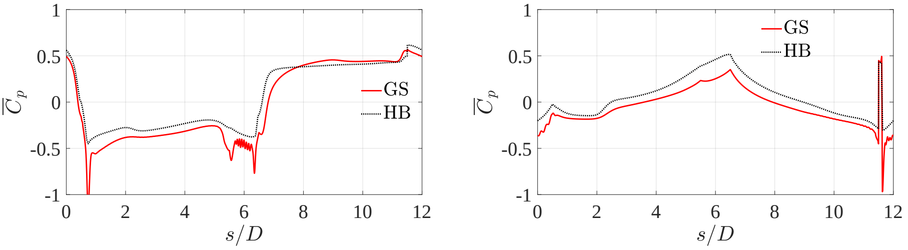

$\alpha = 30°$, *outside* s_0 $\alpha = 30°$, *inside* s_0

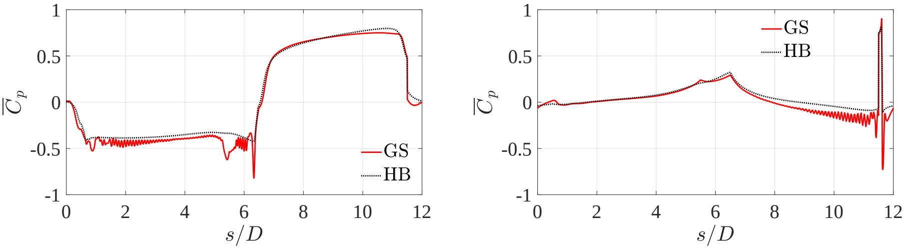

$\alpha = 60°$, *outside* s_0 $\alpha = 60°$, *inside* s_0

Figure 3.24: The $\overline{C}_p$ of the *GS* and *HB* models obtained by using different attack angles.

Unfortunately, similarly to the cases at null angle of attack, although comparable time-averaged flow arrangements are found, the C_p' is hard to be accurately reproduced as it can be seen in Fig. 3.25. We notice that, values of C_p' close to 0.1 have been found to be related to local effects in the previously presented results (see for example Fig. 3.25 where such value is recorded at $inside\ s_0$, downstream the windward surface).

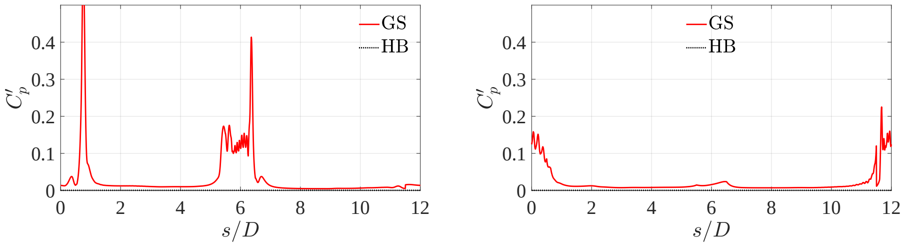

$\alpha = 30°$, *outside* s_0 $\alpha = 30°$, *inside* s_0

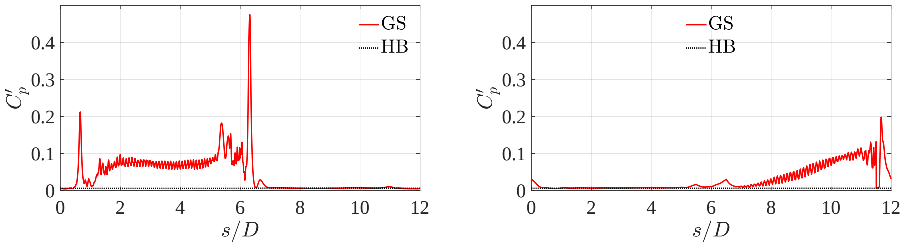

$\alpha = 60°$, *outside* s_0 $\alpha = 60°$, *inside* s_0

Figure 3.25: The C'_p of the *GS* and *HB* models obtained by using different attack angles.

Finally, in Table 3.2 we report the integral force coefficients for all the considered angles of attack. Force coefficients are all made non-dimensional with respect to B and should be intended as calculated with respect to a reference system aligned with the wind direction. It can be noticed that, despite the aforementioned difficulties, a good agreement between *GS* and *HB* models is obtained, being the largest percentage differences measured for the lift coefficient at $\alpha = 30°$, in which a discrepancy of approximately 20% is recorded (moments have net been taken into account due to their small value).

Table 3.2: Integral force coefficients at different attack angles.

	C_d			C_l			C_m		
	GS	*HB*	% diff.	*GS*	*HB*	% diff.	*GS*	*HB*	% diff.
0°	0.251	0.234	6.7%	0.002	6.04×10^{-8}	-	6.45×10^{-8}	-2.89×10^{-8}	-
30°	0.703	0.678	3.7%	0.582	0.476	18.3%	-0.077	-0.041	46.8%
60°	1.040	1.060	1.9%	0.450	0.444	1.3%	-0.045	-0.047	3.1%

3.6 Conclusions

By investigating the flow around a porous 5:1 rectangular cylinder, this paper provides an evaluation of the performance of pressure jump based simulations for the study of external flows around bluff-bodies composed of zero-thickness perforated plates. In particular, the consistency of the results obtained by explicitly modelling the geometry of the porous surface and using pressure jump based simulations have been investigated. Such point should be in fact regarded as an indispensable preliminary activity, necessary to elucidate the range of applicability of currently available techniques, as well as highlighting their critical aspects.

Results show that quantities obtained using the two approaches can be characterized by quantitative or only qualitative agreement, depending on the measured quantity and investigated case. Global forces appear to be in reasonable quantitative agreement for all the considered cases. Despite some sensitivity to the adopted turbulence model, differences appear to be mainly related to local effects which, once amplified downstream, sometimes lead to differences in the overall flow arrangement. On such regard, it is reasonable to assume that in the limit of vanishing pore thickness such effects might vanish, but the current investigation highlights that such a limit requires extremely small pores (probably at least two order of magnitude smaller than the immersed body size). Such aspect might be especially critical for 2D URANS models for which the coherent structures created by the pores are often excessively stable with respect to reality, but it is expected to be generally true.

The analyses confirm the importance of carefully considering the pressure-recovery zones, especially when comparing results obtained by explicitly modelling the pores and using pressure jumps. In fact, a fair comparison between the two modelling approaches requires to move out from such zones, which can extend several pores diameters downstream the perforated surface. As a matter of facts, the extension of pressure recovery zones poses theoretical and practical restrictions on the applicability of pressure jump based simulations. In fact, their extension should be considered as a characteristic geometrical scale of the problem which must vanish with respect to the body size. This once again substantially tightens the requirements needed to characterize a pore as effectively small.

It should be also considered that the shear provided to the flow by the porous surfaces is neglected using standard pressure jump based simulations. While for zero-thickness perforated plates this might be a minor problem, it might be an important aspect for other common configurations (e.g. thick porous surfaces or barriers composed of stacked bluff sections).

Overall, considering the advantages given by using homogenized models, such kind of modeling approach appears to be a necessary simplification when considering structures composed of porous surfaces. Nevertheless, it appears that a conspicuous amount of additional research work is still needed in order to assess their actual range of applicability and accuracy for cases other than screens in internal flows or fences. From this point of view a critical aspect is also represented by their use in conjunction with scale resolving turbulence models, essential to provide accurate predictions of the flow in the proximity of bluff-bodies.

Chapter 4

On the aerodynamics of porous bluff bodies obtained from assembled perforated plates: a numerical study

In the framework of the Benchmark on the Aerodynamics of a Rectangular 5:1 Cylinder (BARC), this paper attempts to provide a contribution to investigate the high-Reynolds flow ($Re = 27,000$ based on the cylinder depth) around hollow rectangular cylinder composed by perforated surfaces. The Large-Eddy Simulation, LES, is adopted as strategy of the turbulence model. Moreover, the effects of surface porosity and pore size on flow features are also analyzed.

This chapter has been submitted to an international peer-reviewed journal.

4.1 Introduction

The evaluation of wind loads over porous bluff bodies obtained assembling perforated plates is an important topic which is lately attracting the attention of the Computational Wind Engineering community [69, 70, 1, 72, 73]. In particular, porous surfaces are found, for example, in wind shields used to protect vehicular traffic from gusts on long span bridges, as well as external layers of porous double skin facades. Despite their almost ubiquitous presence, systematic studies regarding their modeling in scaled wind tunnel models and numerical simulations are still scarce.

Indeed, the presence of small scale pores poses serious difficulties when using both scaled physical models and numerical simulations. In fact, due to the presence of pores, the pressure taps and piping system are hard to be well-arranged in wind tunnel experiments, even when relatively simple geometries are considered [97]. As regards numerical simulations, the presence of numerous small scale pores leads to an extremely large number of cells and, thus, computational costs. We denote those as Explicit Models, *EM*, and from the practical point of view, they are substantially intractable in the majority of the cases.

In order to solve the problem, homogenization techniques can be used. In particular, assuming pores of vanishing size, the presence of the perforated plates can be modeled without explicitly modeling the pores geometry. The homogenization is usually performed taking into account the porous surfaces only by means of the force exerted on the fluid along its normal direction. This is usually referred to as the Pressure Jump approach, *PJ*. Relations between the pressure jump and the surface porosity have been proposed by [36, 77, 79]. Notice that this closely follows the approach usually followed when building reduced scale models for wind tunnel tests, for which only the drag force over the porous element is usually accounted for.

It is important to notice that the aforementioned *PJ* approach, consistently with its derivation, is adopted when the primary interest is to model the drag over immersed bodies whose surfaces are mainly normal to the flow, while application of the *PJ* approach in bluff body aerodynamics appears to be much less direct. It is in fact well-known that the flow around bluff bodies is sensitive to details and leads to complex flow arrangements even when geometrically simple bodies are considered. In order to shed light on the matter, the authors firstly considered the flow over a forward facing step [113] and, recently, investigated by means of URANS the flow around a porous 5:1 rectangular cylinder [120], whose solid counterpart has been deeply studied within the BARC project [105].

In this study, we widen the investigation on the flow around a porous 5:1 rectangular cylinder with the two-fold objective of further checking the consistency between *EM* and *PJ* based models and to characterize the flow modifications occurring due to the combined effects of porosity and attack angle. In particular, LES and URANS are firstly compared at null angle of attack considering both *EM* and *PJ* models. Then, *EM* and *PJ* URANS based models are considered for selected porosities and attack angles, so providing an evaluation of the flow organization evolution with respect to such parameters.

As it will be later further discussed, the work here presented is exclusively numerical. While proper validation against experimental results is surely of great importance, in this case the aforementioned experimental difficulties suggested to firstly attack the problem in a controlled numerical environment, which conveniently allows to isolate and control each investigated aspect, separately. While the presence of additional relevant phenomena might not be excluded by the present investigation, the authors hope that the present work will clarify the limitations of currently available approaches, foster their improvement and provide support to the set up of properly conceived experimental campaigns.

The paper is organized as follows. In Section 4.2, we summarise the state of the art highlighting difficulties and open problems. In Section 4.3, we describe the numerical models used in this work to obtain the results presented in Section 4.4. Finally, conclusions are drawn in Section 4.5.

4.2 State of the art and open problems

As already mentioned, porous surfaces are almost ubiquitous in buildings and infrastructures. In particular, the resistance of porous surfaces to the air flow has been initially studied considering the flow through screens in internal flow conditions. For example, [36] derive a quantitative relation that links the screen porosity to the pressure jump measured on the two sides of the screen, or equivalently to the drag force acting on the screen. Successive studies investigated numerous parameters which might affect such pressure difference, such as the Reynolds number, fluid compressibility and pores arrangement. For instance, the effect of the Reynolds number and the incidence of the incoming flow with respect to the screen normal has been considered in the seminal paper from [37], which proposes a relation between the surface porosity, the Reynolds number, the incidence angle and the measured pressure jump. In this case, also the damping effect operated by the grid on the incoming turbulence has been analysed and compared to previous evaluations proposed in [38], [39], [40] and [41].

In the field of external aerodynamics, the simplest and most common case in which porous surfaces are found is represented by ground mounted fences. In particular, the relationship between the drag force and porosity has been studied by [42]. In that case, a boundary layer flow is considered and the ratio between the fence height and the thickness of the boundary layer is analysed, together with the flow arrangement downstream of the porous fence. The elongation of the vortex in the wake with the increase of the fence porosity has been repetitively reported [43]. Regarding applications, simple ground mounted fences are often applied as wind shields [44, 45] and for the moderation of dust emissions [46, 47]. For instance, the velocity field and pressure distribution around a model fence of finite length upstream a dust source has been studied by [48].

A remarkable complication of the simple case mentioned above, is observed when the porous barrier is positioned above a bluff body. In this case, due to the well-known sensitivity of the flow to geometric details and the incoming flow turbulence, the overall flow arrangement can be affected by the barrier and its geometrical details, even when it is characterized by very high porosity. This is the case of wind-shields over bridge decks, which are commonly used to protect traffic against strong cross wind [49]. Lately, for instance, the effect of porous barrier on the flutter derivatives of three model bridge deck sections has been experimentally studied in [2].

As previously mentioned, the aerodynamic behaviours of bluff bodies is well-known to be extremely sensitive to geometrical details as well as the incoming flow conditions. This is due to the presence of separation bubbles whose scale is comparable to the immersed body size. The shape, organization and dynamics of those bubbles strongly depends on the stability conditions of shear layers detached from the body, often in correspondence of sharp edges. While such phenomena has been widely studied for solid bodies, structures obtained as an assemblage of porous surfaces (usually metal plates) have not been deeply studied yet. Generally speaking, it is known that the ventilation through the porous walls prevents the accumulation of vorticity, so having a favourable effect over the wind loading, in terms of both time-averaged and fluctuating components. This is the case commonly encountered in the cladding of reticular structures applied for aesthetical reasons and an emblematic example is the antenna of the UniCredit building located in Milan, Italy [1].

Porous surfaces can be also used to wrap solid structures in order to protect them from the direct action of the wind. A well-known example are shrouded cylinders [50, 51, 52, 53], which have been repetitively studied aiming at suppressing Vortex Induced Vibrations, VIV. The advantage mainly comes, analogously to the previously mentioned case, by the ventilation through the external layer which prevents the accumulation of vorticity in the proximity of the body.

Finally, in recent years, porous surfaces are becoming increasingly used as external layer of double skin facades. Numerous studies, which are outside the scope of this short review, are dedicated to assess their efficiency in enhancing comfort and decreasing energy consumption. As regards their aerodynamic behaviour, few studies have been presented at the moment [54, 14]. Among these studies, a common conclusion is that the porous external skin reduces the fluctuating pressure on the side faces and global forces [55].

As regard CFD, due to the aforementioned difficulties, homogenization techniques appears to be a more practical alternative with respect to the explicit modeling of the geometry. A common way to describe the aerodynamic effect of such porous surfaces is to consider their resistance to the flow, i.e. the pressure loss coefficient, K [56, 57]. In such context, the aforementioned relations between pressure jump and surface porosity can be adopted and for internal flows the approach usually proves satisfactory [60].

As regard external flows, fewer studies are currently available. Related, although not immediately comparable applications are the modeling of the actuator disc of wind turbines [61], which is often simulated, as a first approximation, as a porous disk with a blade-velocity dependent loss coefficient (calibrated to match the total drag over the rotor). In particular, such approach has been used in conjunction with several turbulence models by [62], which compares the velocity, turbulence intensity and shear stress in the turbine wake. It is found that the porous disk approach leads to acceptable results in the far wake but accuracy decreases just downstream the blades. Other similar applications of porous media can be found, for instance, in the reproduction of the flow over forest canopies [63, 64], for which the explicit reproduction of the geometry is extremely difficult.

Summarizing, the use of homogenized models to represent the effect of porous surfaces is still far from being well-established for external flows and especially, in the modeling of porous bluff bodies. In particular, numerous aspects would merit careful consideration. For instance, homogenized models assume vanishing pore size compared to the overall immersed body size. It is currently not clear how severe this limitation is in practice. Secondarily, empirical laws deduced for confined screens are usually valid for null or moderate attack angles. In the case of bluff bodies, the flow might be almost tangential to the porous surfaces, so that evaluating the forces acting on them would require additional research. Finally, the pressure jump approach only considers the force exchanged between the fluid and the porous surface in its normal direction, so completely disregarding shearing effects, i.e. the effect of exchanged forces lying on the porous surface plane.

Despite such limitations, the pressure jump approach is still the most convenient and widely adopted method to represent porous surfaces at a reasonable computational cost [65, 66]. In such context, its validation appears to be fundamental in order to clarify the limits of its applicability.

4.3 Numerical setup

As anticipated, we here consider a porous 5:1 rectangular cylinder, whose solid analogue has been the object of numerous investigations within the BARC project [105]. For the sake of simplicity, to allow a clearer comparison with two-dimensional models and in order to reduce computational costs, porosity is here obtained in a simplified manner with respect to the usual cases found in applications, i.e. by considering that pores are infinitely long in the direction of the rectangular cylinder axis.

We start by describing the $3D$ grid later used for LES. As shown in Fig. 4.1 (a), the domain size in $x-$, $y-$ and $z-$ directions is respectively equal to $41B$, $30B$ and B, which leads to a blockage ratio of 0.7%, while the distance between the front surface and the inlet is set to $\Lambda_x = 15B$.

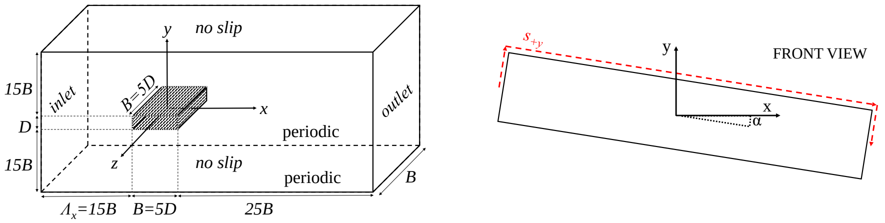

(a) (b)

Figure 4.1: Computational model: (a) the computational domain and (b) the geometry with an attack angle of α and pressure probes distribution.

Close to the rectangular cylinder, the mesh size in the $x-$ and $y-$ directions is set as $\delta_x/B = 2.5 \times 10^{-3} = \delta_y/B = 2.5 \times 10^{-3}$ while the spanwise dimension is set to $\delta_z/B = 4.0 \times 10^{-2}$. The mesh counts approximately $5.75M$ cells. A view of the resulting computational grid is shown in Fig. 4.2 (a).

A fixed velocity value, U_0, is imposed at the inlet boundary. This makes the Reynolds number based on the cylinder depth, $Re = \rho U_0 D/\nu$ =2.7×10^4, where ν is the kinematic air viscosity. Moreover, a zero pressure is imposed at the outlet boundary, while a null pressure gradient is prescribed at the inlet. A slip boundary condition is imposed at the top and bottom of the domain. For the front and back surfaces, periodic boundary conditions are adopted.

The *k-equation* model is considered [121] and the wall treatment is performed with a van Driest damping law. A centered second-order differentiation scheme is adopted for the diffusive terms, while a bounded LUST scheme is adopted for the advective terms. Time integration is performed by using the Crank-Nicolson scheme. The coupling of pressure and velocity is obtained for all simulations by using the well-known Pressure-Implicit with Splitting of Operators (PISO) algorithm.

The two-dimensional computational grid adopted for URANS is derived from that used for LES as regards the sizing in the proximity of the rectangle. In this case, due to the fact that a rotor-stator approach has been used later to study different attack angles, the mesh sizing has been kept constant within the rotor. The resulting mesh counts approximately 210 k cells. In this case the Shih's $k - \epsilon$ model is adopted with an incoming turbulence intensity of 2%. This eliminates the need to calculate the wall-distance which is a parameter of the usually adopted $k - \omega$ SST model, which would not be properly defined for porous grids and, anyway, not correctly calculated for porous walls simulated by means of a *PJ*. Analyses reported in [120] anyway show that, despite such theoretical difficulties, the obtained results are similar to those obtained using the $k - \omega$ SST model.

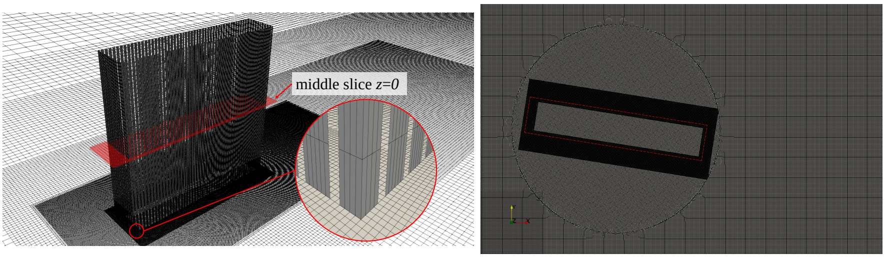

(a) (b)

Figure 4.2: The adopted computational grids: (a) 3D grid used for LES simulation and (b) 2D grid used for URANS simulations.

As regards the boundary conditions applied at the porous wall, for *EM* a slip condition is adopted. This choice is aimed at guaranteeing the comparability with *PJ* models, which are unable to provide shearing effects to the flow. This surely represents a simplification of the expected real behaviour but it is here aimed at eliminating effects which might not be correctly captured by standard *PJ* models. Notice that this is consistent with the usual simplification for which porous elements are taken into account in wind tunnel tests only reproducing their drag force. For the same reason the considered porous surface is built in order to have zero thickness, so that forces exchanged between the fluid and the grid are constraint to be in the direction normal to the grid, in agrement with the *PJ* models.

The pressure jump used for the *PJ* models is calculated relying on the formula proposed in [120], which reads

$$\Delta p = \frac{\rho U_n^2}{2} \frac{(a_1\beta + 2)(\beta - 1)}{\beta^2(a_2 - 1)}, \tag{4.1}$$

where Δp is the pressure jump, ρ is the fluid density, U_n is the local velocity normal to the surface, β is the porosity defined by the pore area divided by the total surface area, $a_1 = 0.5$ and $a_2 = -0.1$. The formula, semi-empirical in nature, proved in good agreement with experimental data presented in [35] and numerical simulations.

The open source Finite Volume software OpenFOAM is adopted to perform the simulations.

4.4 Results

In this section we present the results collected in the present campaign of numerical experiments. Firstly we proceed to the comparison of LES and URANS at null angle of attack using both *EM* and *PJ*. The effect of the pore size is also discussed. Subsequently, limiting to URANS models, we evaluate the effect of selectively modeling specific walls with *EM* and *PJ*, so obtaining hybrid models aimed at revealing which part of the model is affecting the flow organization at specific locations. Finally, the attack angle and the porosity are systematically varied.

4.4.1 LES and URANS at null angle of attack

Contours of Q-criterion for the LES cases are shown in Fig. 4.3, which is colored by the instantaneous velocity. Contrarily to the fully solid case, it appears that well-separated vortices of small size are continuously shed by the frontal corners without accumulating in separation bubbles on the sides.

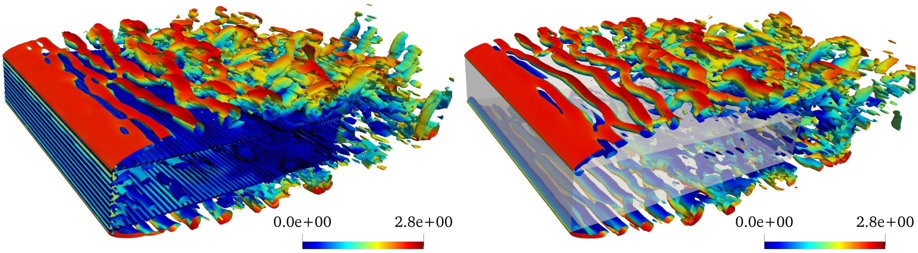

(a) *EM* (b) *PJ*

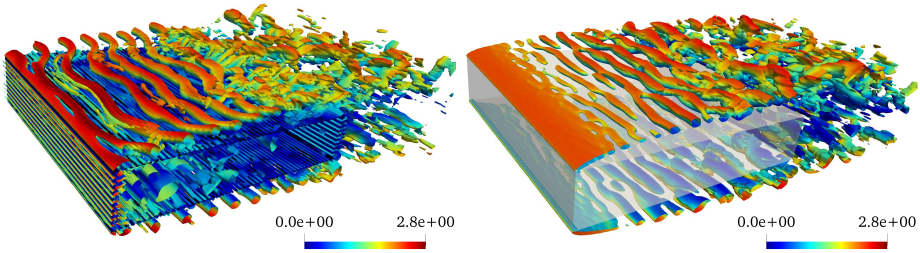

(c) *EM* (d) *PJ*

Figure 4.3: The contours of Q for the LES cases characterized by (a) and (b): a porosity of 25%, (c) and (d): a porosity of 45%, which is colored by the instantaneous velocity magnitude.

In particular, Fig. 4.3 (a) and (b) show the results obtained for 25% porosity with *EM* and *PJ* models respectively, while Fig. 4.3 (c) and (d) show results obtained for 45%. For the first case good agreement is found between *EM* and *PJ* models in terms of the shed vortices size and spacing, as well as the distance from the edge at which the shear layers detached from the leading corner roll up. The vortices, at least in the proposed simulations, show a high along-span coherence and proceed keeping a well-ordered arrangement up to approximately the middle of the horizontal rectangle side, where the two-dimensionality of the flow suddenly decreases in favour of a more chaotic three-dimensional arrangement. The point where such transition takes place seems to be located closer to the leading edge for the EM model than for PJ one. Similar considerations hold for the 45% porosity case, in which, nevertheless, the flow at the leading edge corner appears to show more differences with respect to the previous case. Here, the *EM* model predicts the rolling up of the shear layers just at the leading corner with the production of vortices of size comparable to the ones observed for the 25% porosity case, while the *PJ* shows the formation of very fine structures with limited along span dimensions. The obvious distortion of the vortices distribution observed for the 45% porosity using the *EM* model is due to the emergence of three dimensional vortical structures in the spanwise direction. Figure 4.4 reports the streamlines of the time-averaged velocity field. It can be seen that overall a good qualitative agreement is reached between *EM* and *PJ* models at different porosities, although differences in the flow organization emerge.

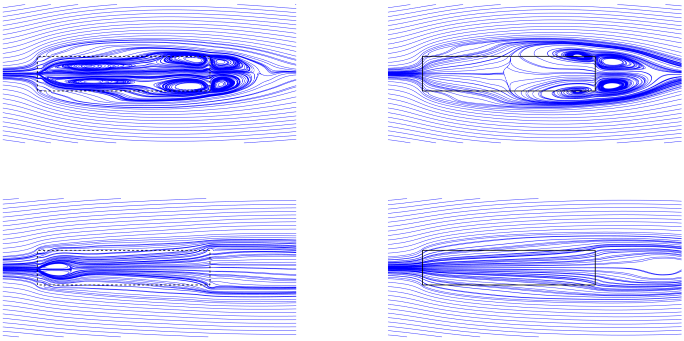

Figure 4.4: Streamlines of the time-averaged velocity field for the LES cases characterized by (a) and (b): a porosity of 25%, (c) and (d): a porosity of 45%.

In particular, for both porosities, the *EM* model shows the presence of vortical structures not predicted by the *PJ* approach. The figure also suggests that the aforementioned sudden transition from an ordered state to a chaotic three-dimensional one of the vortices shed at the leading edge, might be related to the emergence from the rectangle interior of the flow passing through the frontal face, eventually recirculated within the bubbles partially or entirely enclosed in the porous body.

For the sake of completeness, the streamlines of the time-averaged velocity field for URANS based simulations are shown in Fig. 4.5. Results appear to be qualitatively consistent with those obtained by LES, often showing the same differences there observed between EM and PJ. It shall be noticed that the explicit model here predicts for 25% porosity, an asymmetric time-averaged velocity distribution probably caused by small asymmetries in the adopted computational grid.

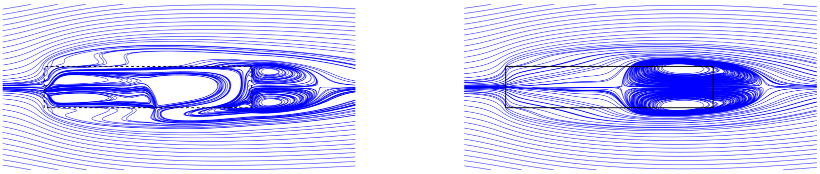

(a) *EM* (b) *PJ*

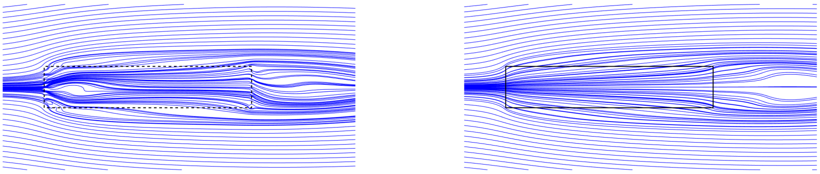

(c) *EM* (d) *PJ*

Figure 4.5: Streamlines of the time-averaged velocity field for the URANS cases characterized by (a) and (b): a porosity of 25%, (c) and (d): a porosity of 45%.

As shown in Fig. 4.6 and 4.7, the previously shown differences in the flow organization are concentrated in low velocity zones, while being the overall flow field quite similar for all tested models, especially if compared to the variability observed taking into account different porosities.

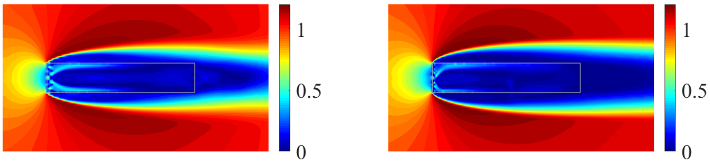

(a) LES, *EM* (b) URANS, *EM*

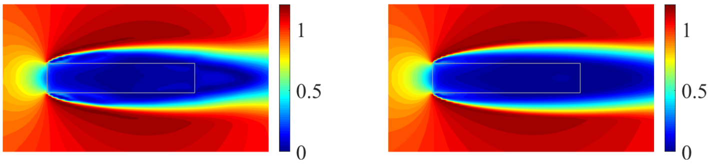

(c) LES, *PJ* (d) URANS, *PJ*

Figure 4.6: The distributions of time-averaged velocity magnitude, $\overline{U}/U_0$, for 25% porosity cases.

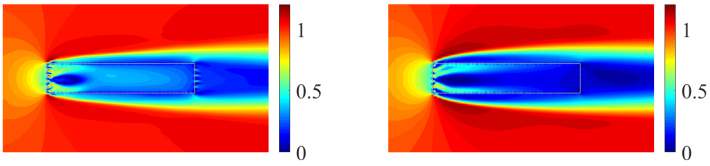

(a) LES, *EM* (b) URANS, *EM*

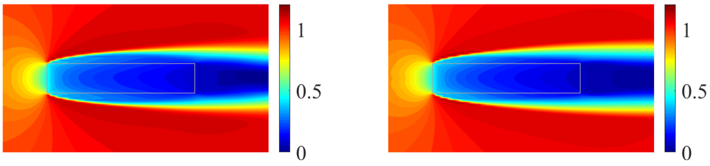

(c) LES, *PJ* (d) URANS, *PJ*

Figure 4.7: The distributions of time-averaged velocity magnitude, $\overline{U}/U_0$, for 45% porosity cases.

Finally, the pressure field obtained for 25% porosity is shown in Fig. 4.8. Here the most notable difference is that in explicit models a higher overall pressure jump is observed between the inner part, bounded by the rectangle, and the external part. As the pressure jump is determined by the velocity field at the porous surface location, this can be attributed to mismatches in the velocity field predicted by EM and PJ models or to inaccuracies of the pressure jump determination when flows highly skewed with respect to the barriers normal are present, such as along the rectangle sides.

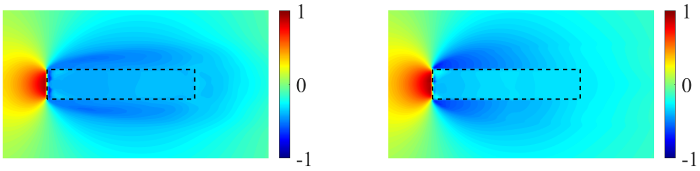

(a) LES, *EM* (b) URANS, *EM*

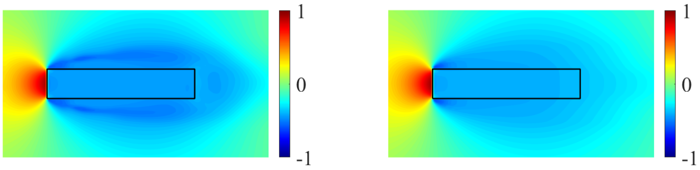

(c) LES, *PJ* (d) URANS, *PJ*

Figure 4.8: The distributions of time-averaged pressure coefficient, $\overline{C}_p$, for 25% porosity cases.

Despite the aforementioned discrepancies, the drag coefficient, C_d, measured on *EM* and *PJ* cases are in reasonable agreement, which is shown in Fig. 4.9. Here it can be noticed that only at relatively high porosities the drag force is efficiently reduced, being in other cases the drag decrease on the windward face compensated by the increase at the leeward one, see Fig. 4.9 (b) and (c).

Summarizing it has been shown that reasonable agreement can be obtained between EM and PJ models, here intending that most qualitative differences in the flow organization at different porosities can be captured, this is reflected also by a very good matching in terms of the drag variation with porosity, with larger deviations recorded only at the extreme ends of the considered porosities interval.

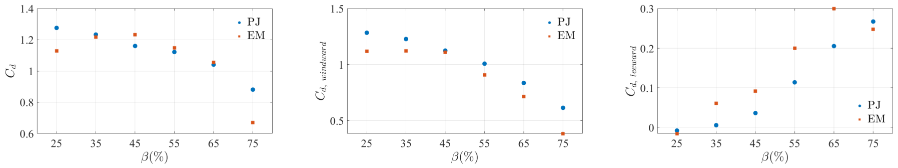

(a) (b) (c)

Figure 4.9: The drag coefficient, C_d, measured on (a): overall cylinder, (b): the windward surface and (c): the leeward surface of URANS cases.

4.4.2 Effect of pore size

Despite the good results previously presented, some obvious differences in the flow organization are recorded between EM and PJ models. Some of such differences, for instance the creation of vortical structures after the frontal face in EM models which is not seen in PJ ones, might be due to the fact that the considered pore dimensions are not vanishing with respect to the overall body size. We thus here assess the sensitivity of the obtained results to the pore size. As differences are more apparent for the 25% porosity case, only such case is here investigated for the sake of conciseness. Specifically, keeping the porosity constant, we consider geometries characterized by pore size equal to $0.05D$ and $0.025D$ for LES, while for URANS, due to their lower computational costs, we consider also $0.0125D$. It should be noted that, although different pore sizes are adopted, the number of mesh cells for each pore is set to be the same in all cases.

The time-averaged pressure coefficient, $\overline{C}_p$, measured along a path located outside the volume enclosed by the rectangle and spanned by the coordinate s_{+y} (see Fig. 4.1) is reported in Fig. 4.10. The path is located at a distance equal to $0.025D$ from the rectangle surface. The local effect of the pores is clearly observed, for instance, on the frontal face. For LES, results appear to be similar for all considered cases. For URANS, the pore size appears to affect pressure in the proximity of the corner. When considering pores of decreasing size, the low pressure measured at the corner reduces tending to the PJ value, although it is not possible to observe a clear monotonic convergence of the EM model to PJ in the whole distribution when decreasing the pore size. Nevertheless, the maximum differences appear to reduce, indicating that at least part of the previously noticed differences can be attributed to the fact that the limit of vanishing pore size might be not easily attainable and that for LES such requirement might be more easily attainable than for 2D URANS.

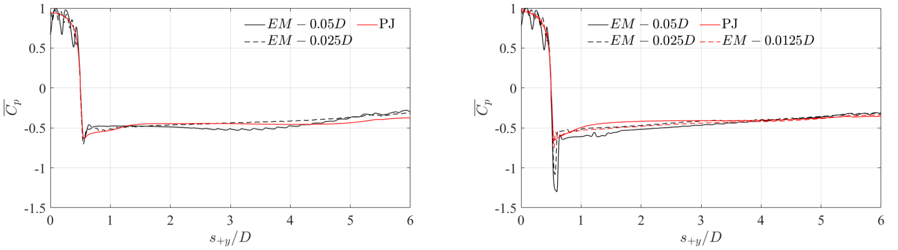

(a) (b)

Figure 4.10: The time-averaged pressure coefficient, $\overline{C}_p$, of (a): LES and (b): URANS cases when different pore sizes are adopted.

The distribution of C_p' is shown in Fig. 4.11. Results obtained for the mean pressure field are confirmed: a tendency of the EM to approach the results of the PJ approach con be appreciated, although convergence appears to be slow and not uniform for all considered locations, making very difficult to separate effects produced by the presence of pores of non-vanishing dimensions from those induced by other sources of errors.

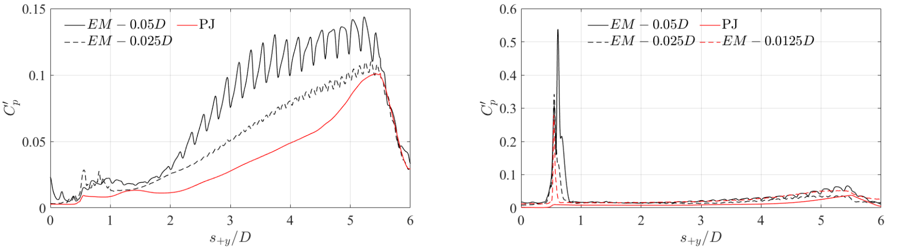

(a) (b)

Figure 4.11: The root mean square, C_p', of (a): LES and (b): URANS cases when different pore sizes are adopted.

Finally, in Tab. 4.1 we report the drag force for all analysed cases. It can be seen that predictions are similar for all models, being LES less sensitive than RANS to the ratio between the pores and the body size.

Table 4.1: The C_d of 25% porosity cases that characterized by different pore sizes.

	EM - $0.05D$	*EM* - $0.025D$	*EM* - $0.0125D$	*PJ*
LES	1.20	1.20	-	1.22
URANS	1.14	1.17	1.22	1.28

4.4.3 Hybrid *EM*/*PJ* models

In the previous section the effect of pore size was discussed. Here we selectively apply the EM and PJ modeling strategies to different surfaces within the same model, aiming at highlighting if results are particularly sensitive to the modeling approach chosen for some of the walls. Again, for the sake of conciseness, only results for 25% porosity are considered and results are obtained from URANS models.

Firstly, the distributions of $\overline{C}_p$ are shown in Fig. 4.12 and Fig. 4.13, where the *EM* and *PJ* surfaces are represented using dash and solid lines, respectively. Overall, by comparing Fig. 4.8 (b) and Fig. 4.12, it can be seen that results are particularly sensitive to the modeling strategy used for the horizontal walls for the 25% porosity case, with PJ models leading to very low pressure jumps between the inside and outside of the rectangle, contrarily to *EM* models. Secondarily, the flow appears to be sensitive to the approach used to model the frontal face. Results obtained for the 45% porosity case are reported in Fig. 4.13, confirming the previously obtained results.

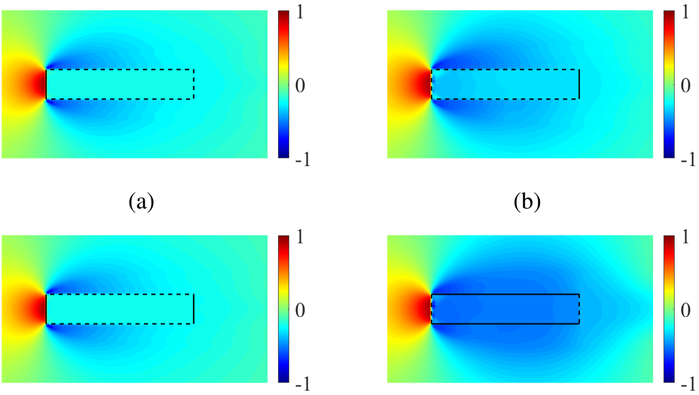

(a) (b)

(c) (d)

Figure 4.12: The distributions of $\overline{C}_p$ for the 25%-porosity cases, where the *PJ* approach is adopted for (a): windward surface, *W* (b): leeward surface, *L* (c): both the windward and leeward surfaces, *W*+*L* (d): both the upper and bottom surfaces, *U*+*B*.

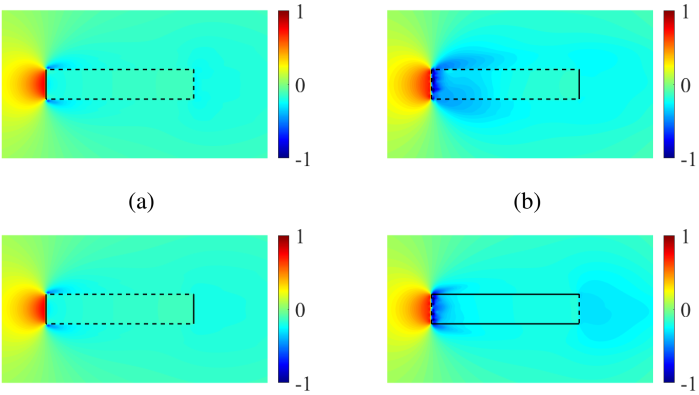

(a) (b)

(c) (d)

Figure 4.13: The distributions of $\overline{C}_p$ for the 45%-porosity cases, where the *PJ* approach is adopted for (a): windward surface, *W* (b): leeward surface, *L* (c): both the windward and leeward surfaces, *W*+*L* (d): both the upper and bottom surfaces, *U*+*B*.

For all the previously considered cases, the drag coefficient measured on the whole rectangle, its windward face and its leeward face are reported in Fig. 4.14. All the models provide similar results and discrepancies on the windward and leeward face tend to be of opposite sign, so balancing each other.

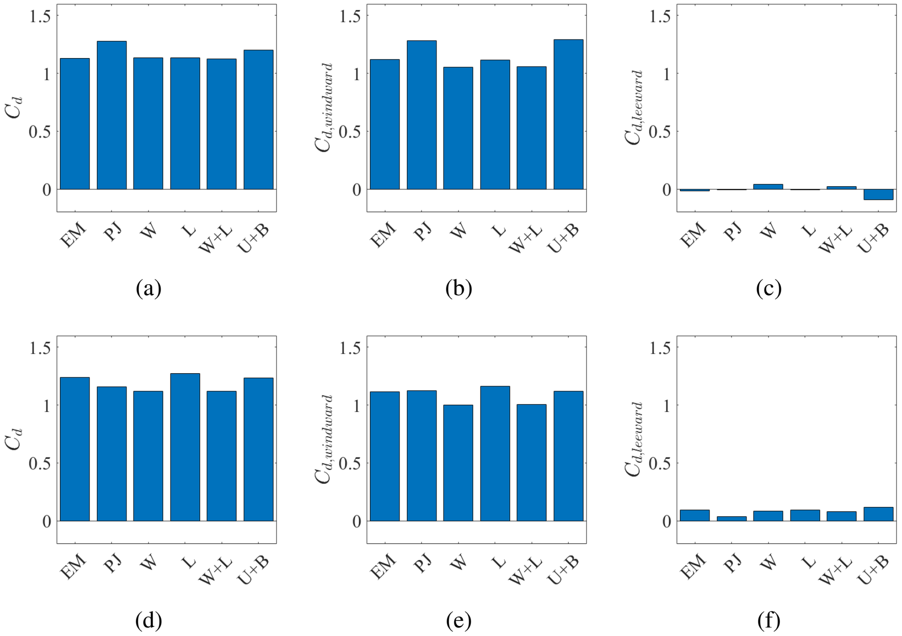

Figure 4.14: The drag coefficients, C_d, of (a) to (c): 25%-porosity cases and (d) to (f): 45%-porosity cases.

4.4.4 Effect of porosity and angle of attack

We now investigate the modifications occurring in the flow for different porosities ($\beta = 25\%, 35\%, 45\%, 55\%, 65\%, 75\%$) and attack angles ($\alpha = 3°, 6°, 9°$) by using URANS.

The distributions of instantaneous velocity magnitude, U/U_0, are shown in Fig. 4.15 for 25% porosity, while time-averaged velocity magnitude contours are reported in Fig. 4.16. It can be noticed that the instantaneous velocity distributions show some differences between *EM* and *PJ* models, especially in the shedding mechanism, with the wake being systematically shorter in *EM* models with respect to *PJ* ones. Despite such differences, the time-averaged velocity distribution shows a good matching between the two modeling strategies, being the main differences located in low-velocity zones.

(a) *EM*, $\alpha = 3^\circ$ (b) *PJ*, $\alpha = 3^\circ$

(c) *EM*, $\alpha = 6^\circ$ (d) *PJ*, $\alpha = 6^\circ$

(e) *EM*, $\alpha = 9^\circ$ (f) *PJ*, $\alpha = 9^\circ$

Figure 4.15: The contours of instantaneous velocity magnitude, U/U_0, for the 25%-porosity cases.

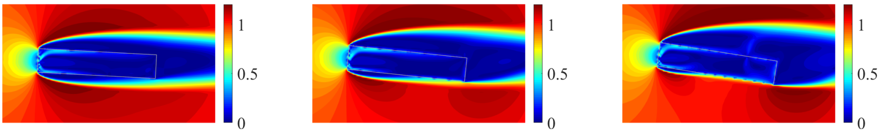

(a) *EM*, $\alpha = 3^\circ$ (b) *EM*, $\alpha = 6^\circ$ (c) *EM*, $\alpha = 9^\circ$

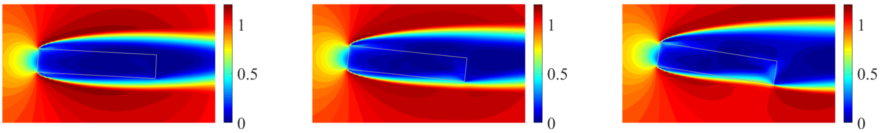

(d) *PJ*, $\alpha = 3^\circ$ (e) *PJ*, $\alpha = 6^\circ$ (f) *PJ*, $\alpha = 9^\circ$

Figure 4.16: The contours of time-averaged velocity magnitude, $\overline{U}/U_0$, for the 25%-porosity cases.

The good matching is confirmed also by the prediction of the drag coefficient, C_d. In particular, Fig. 4.17 reports a scatter plot of results obtained by both modeling strategies in terms of overall drag force as well as the contribution of the windward and leeward faces, separately. Points are generally aligned along the graph bisector, indicating a reasonable matching between *EM* and *PJ* models. It can be again seen that the errors introduced on the windward and leeward faces generally tend to be of opposite sign, so partially compensating each other.

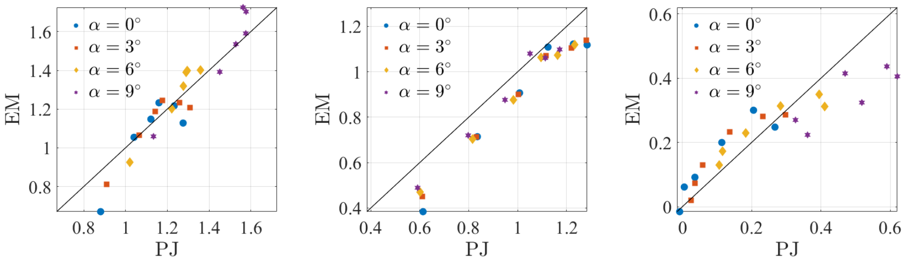

(a) C_d (b) $C_{d},\ windward$ (c) $C_{d},\ leeward$

Figure 4.17: The drag coefficients measured on (a): all surfaces, (b): windward surface, (c): leeward surface.

In order to provide a synthetic representation of the obtained results, Table 4.2 reports the differences of C_d obtained by using the *EM* and *PJ* models. Such difference is defined as

$$Diff = \frac{\sqrt{\sum\left(C_{d,\ PJ} - C_{d,\ EM}\right)^2}}{\sqrt{\sum C_{d,\ EM}^2}} \times 100\%, \tag{4.2}$$

where the $C_{d,\ PJ}$ and $C_{d,\ EM}$ respectively means the drag coefficients obtained by using the *PJ* and *EM* approaches. Differences are typically in the order of 6% and appear to be less pronounced at intermediate porosities, reaching values of approximately 30% only at very high porosities.

Table 4.2: The difference of C_d between the *EM* and *PJ* cases.

	$\alpha = 0^\circ$	$\alpha = 3^\circ$	$\alpha = 6^\circ$	$\alpha = 9^\circ$	α-Averaged
$\beta = 25\%$	9.04	8.46	2.98	7.47	6.99
$\beta = 35\%$	1.19	0.67	8.17	1.09	2.78
$\beta = 45\%$	6.54	5.80	7.77	9.03	7.29
$\beta = 55\%$	1.97	3.49	2.85	1.09	2.35
$\beta = 65\%$	1.30	0.05	1.56	4.30	1.80
$\beta = 75\%$	31.40	12.18	10.39	7.10	15.27
β-Averaged	8.57	5.11	5.62	5.02	6.08

Despite the reasonably good results obtained for the drag coefficient, a much worse agreement is found in terms of lift coefficient, C_l. In particular, Fig. 4.18 shows the variation of the lift coefficient for different incidence angles and porosities. While the adopted *EM* models lead to a clearly non-null lift, the *PJ* ones predict a null C_l for almost all cases, with appreciable values only for low porosities at high angle of attack.

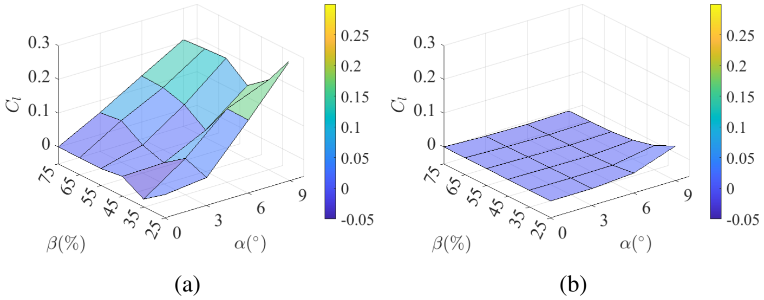

Figure 4.18: The lift coefficients measured in (a): *EM* cases and (b): *PJ* cases.

4.5 Conclusions

Following previous investigations from the authors, this paper evaluates the performance of pressure-jump based modeling for the investigating of the flow through a hollow porous 5:1 rectangular cylinder. Such evaluations are performed considering different surface porosities, pore size and attack angles, with the aim of verifying the consistency between explicit (denoted as *EM*) and pressure-jump (denoted as *PJ*) based models, as well as individuating factors which might lead to their discrepancies.

The considered cases, characterized by pores infinitely elongated in the span-wise direction (assumption needed to contain computational costs for LES and allow for the use of 2D models for URANS), shall be seen as a simplification of the geometries usually found in applications. Despite such simplifications some useful considerations can be deduced:

1. a reasonable agreement between *EM* and *PJ* models appear to be more easily attained for 3D LES than for 2D URANS. Differences appear to be mainly concentrated in the low-velocity zones of the flow field;
2. the main differences in the flow organization at varying porosities produced by *EM* models can be successfully captured by *PJ* models;

3. the limit of vanishing pore size is not easily attainable and, although differences between *EM* and *PJ* models diminished by considering pores of decreasing size, a clear overall convergence could not be established;
4. the use of the considered *PJ* model led to some discrepancies with *EM* models as regards the pressure distribution within the rectangle. It was possible to attribute it mainly to the modeling of the horizontal sides, where the flow is almost tangent to the porous surface;
5. overall drag forces measured in *EM* and *PJ* models generally appear to be in reasonable agrement, while strong disagreement was found in terms of lift forces.

The aforementioned conclusions suggest to proceed in the use of both *EM* and *PJ* models with carefulness due to different reasons. For *EM* models, problems might arise due to the dependence of the results from the particular pore distribution and mesh size, so that adopting pores bigger than those actually present on the real porous element might introduce errors, even when such pores are small compared to the overall structure. For *PJ* models the *a priori* simplification of the interaction between the fluid and the porous surface might be responsible for mismatches. In fact, we recall that standard *PJ* models do not account for shearing forces and their definition is often based on cases for which the flow is approximately normal to the porous surface, which is often not the case for porous bluff body aerodynamics.

4.6 Appendix

4.6.1 The $\overline{C}_p$ of all cases

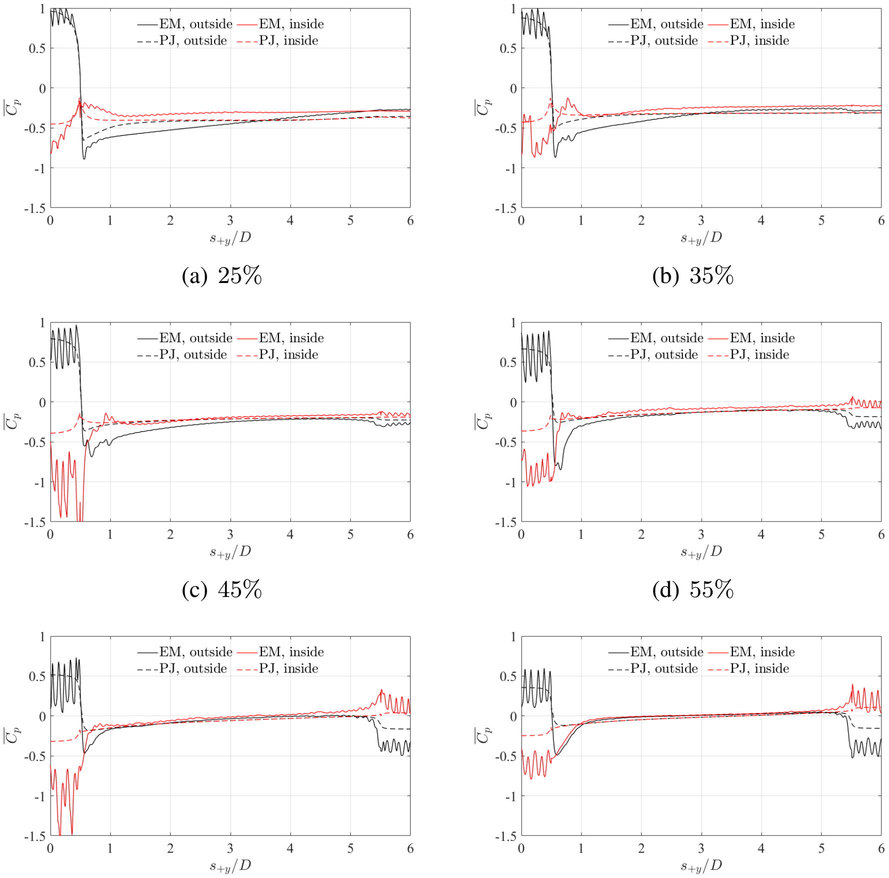

(a) 25%

(b) 35%

(c) 45%

(d) 55%

(e) 65%

(f) 75%

Figure 4.19: The time-averaged pressure coefficient, $\overline{C}_p$, along the $oustside$ s_{+y} and $inside$ s_{+y} when the angle of attack is not adopted.

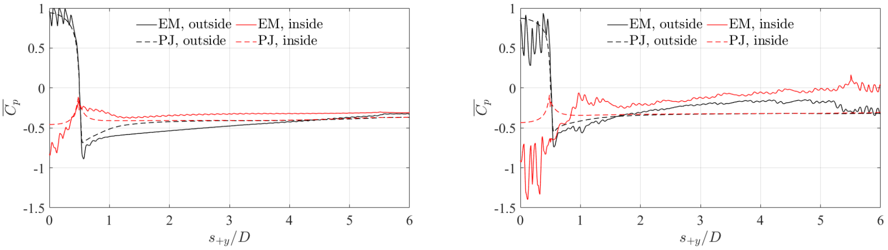

(a) 25%　(b) 35%

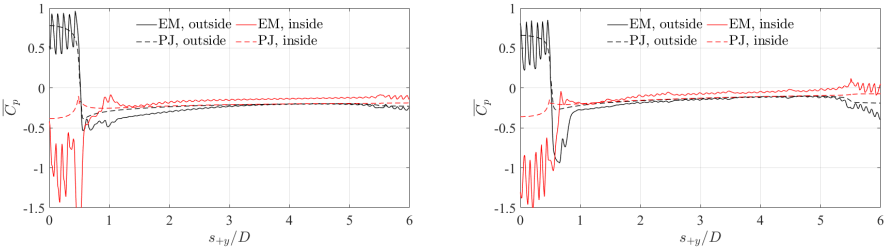

(c) 45%　(d) 55%

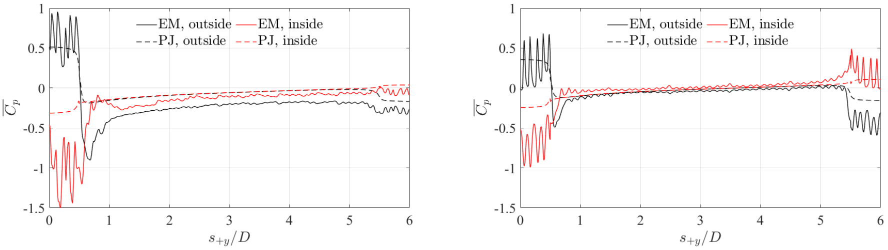

(e) 65%　(f) 75%

Figure 4.20: The time-averaged pressure coefficient, $\overline{C}_p$, along the $oustside\ s_{+y}$ and $inside\ s_{+y}$ when an attack angle of 3° is adopted.

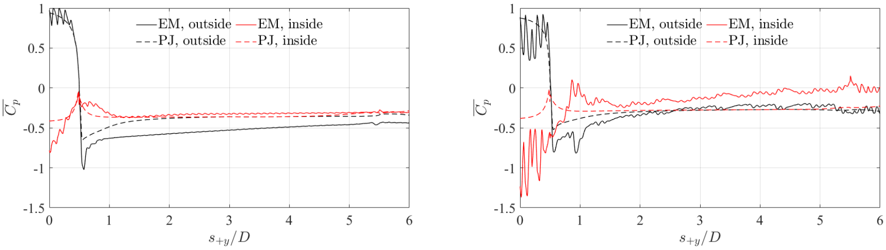

(a) 25%

(b) 35%

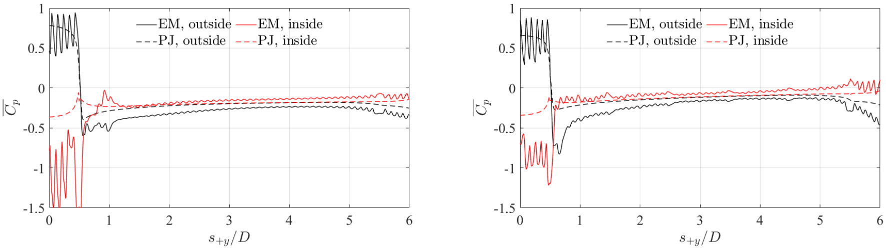

(c) 45%

(d) 55%

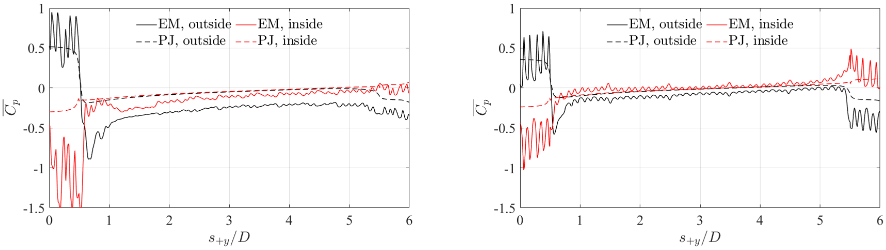

(e) 65%

(f) 75%

Figure 4.21: The time-averaged pressure coefficient, $\overline{C}_p$, along the $oustside$ s_{+y} and $inside$ s_{+y} when an attack angle of 6° is adopted.

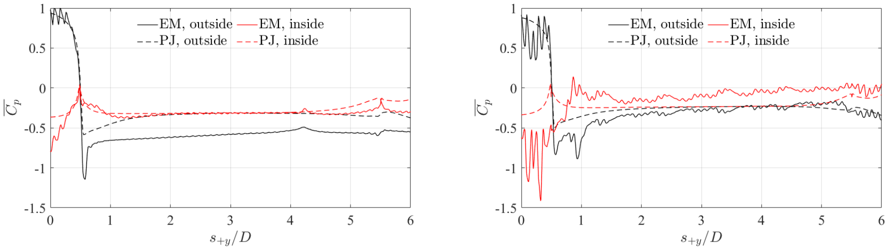

(a) 25%   (b) 35%

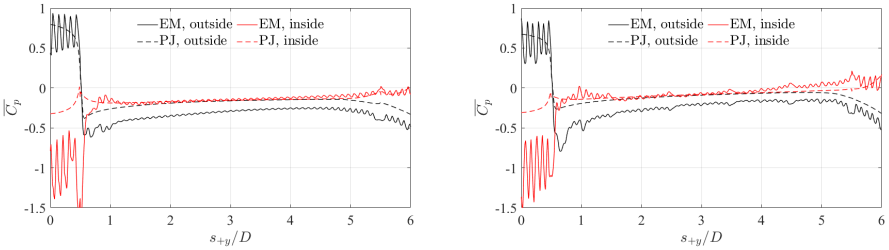

(c) 45%   (d) 55%

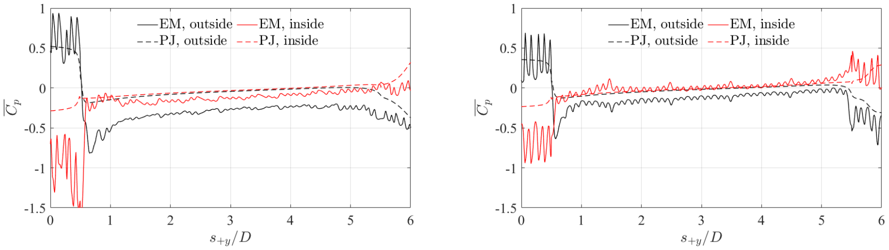

(e) 65%   (f) 75%

Figure 4.22: The time-averaged pressure coefficient, $\overline{C}_p$, along the $oustside$ s_{+y} and $inside$ s_{+y} when an attack angle of 9° is adopted.

4.6.2 The C_p' of all cases

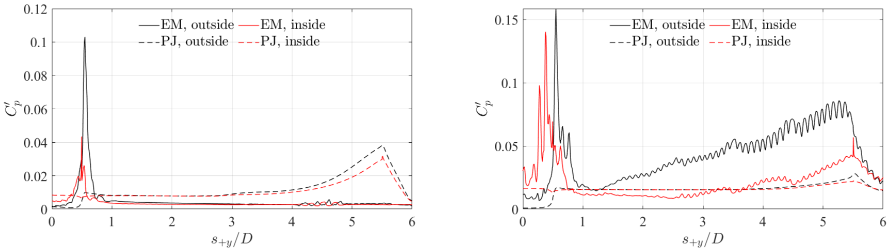

(a) 25%
(b) 35%

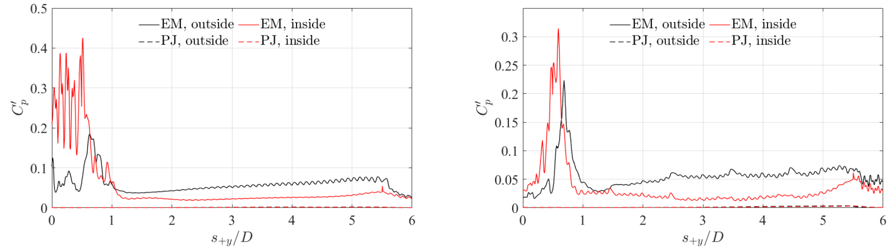

(c) 45%
(d) 55%

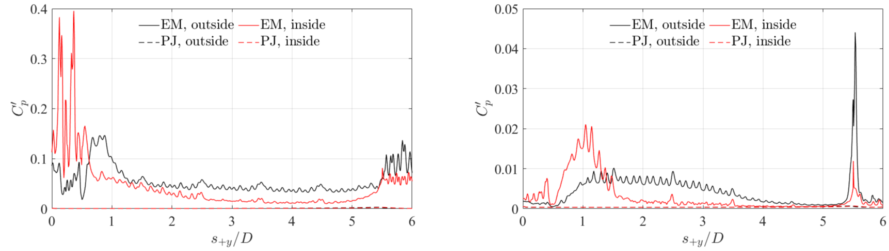

(e) 65%
(f) 75%

Figure 4.23: The root mean square, C_p', along the *oustside* s_{+y} and *inside* s_{+y} when the angle of attack is not adopted.

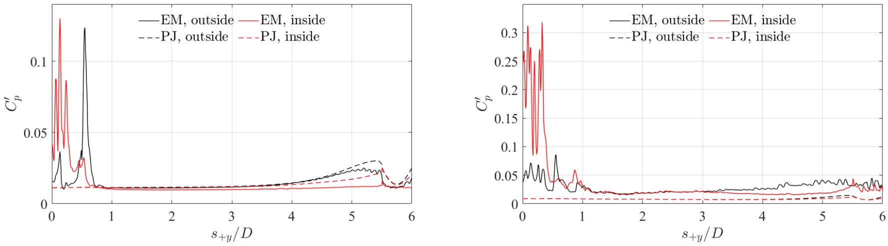

(a) 25%   (b) 35%

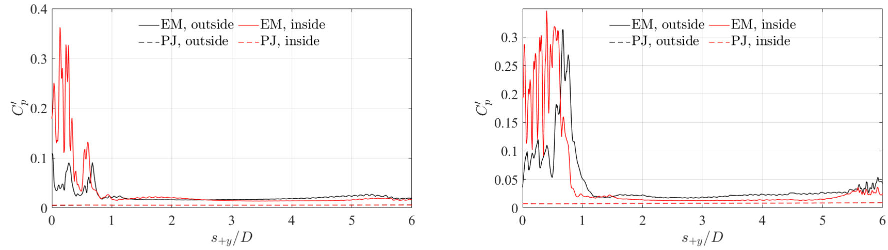

(c) 45%   (d) 55%

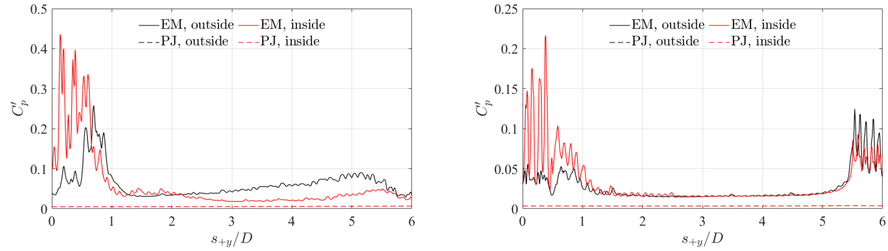

(e) 65%   (f) 75%

Figure 4.24: The root mean square, C'_p, along the $oustside\ s_{+y}$ and $inside\ s_{+y}$ when an attack angle of 3° is adopted.

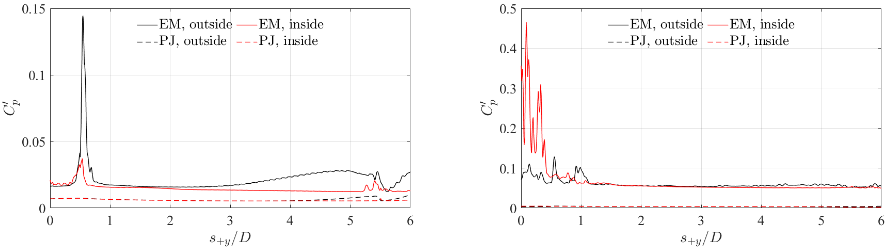

(a) 25% (b) 35%

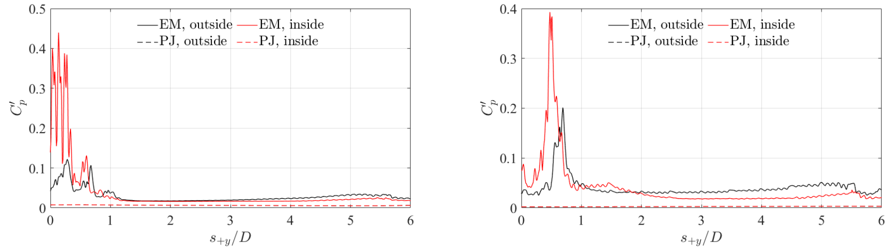

(c) 45% (d) 55%

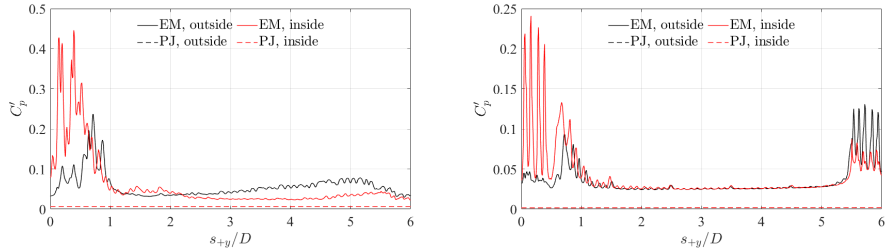

(e) 65% (f) 75%

Figure 4.25: The root mean square, C_p', along the $oustside$ s_{+y} and $inside$ s_{+y} when an attack angle of 6° is adopted.

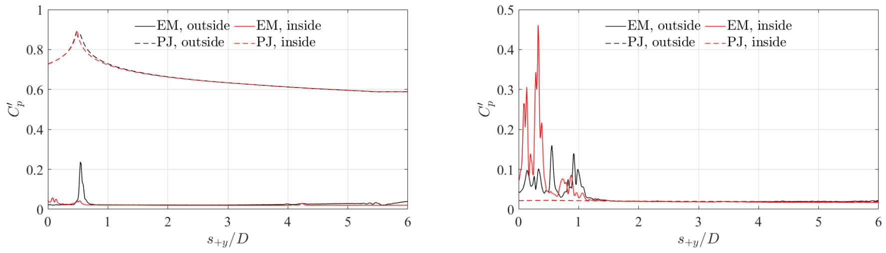

(a) 25%

(b) 35%

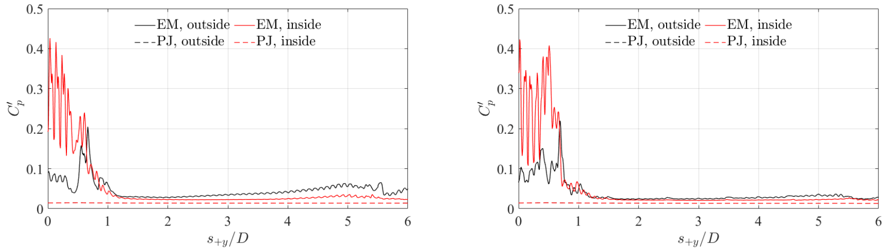

(c) 45%

(d) 55%

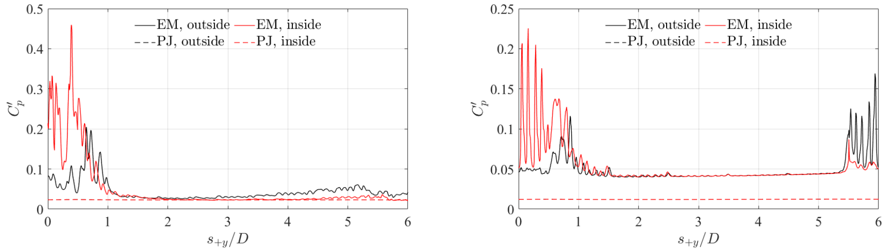

(e) 65%

(f) 75%

Figure 4.26: The root mean square, C_p', along the *oustside* s_{+y} and *inside* s_{+y} when an attack angle of 9° is adopted.

4.6.3 The aerodynamic coefficients of all cases

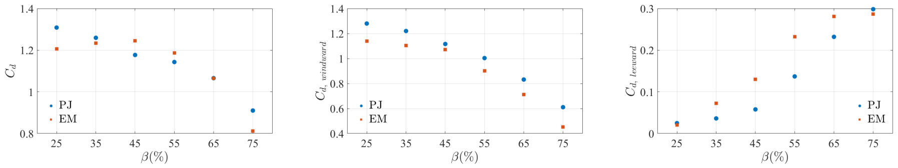

(a) (b) (c)

Figure 4.27: The drag coefficient, C_d, measured on (a): overall cylinder, (b): the windward surface and (c): the leeward surface of URANS cases when an attack angle of 3° is adopted.

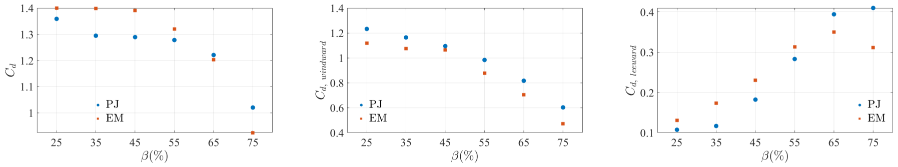

(a) (b) (c)

Figure 4.28: The drag coefficient, C_d, measured on (a): overall cylinder, (b): the windward surface and (c): the leeward surface of URANS cases when an attack angle of 6° is adopted.

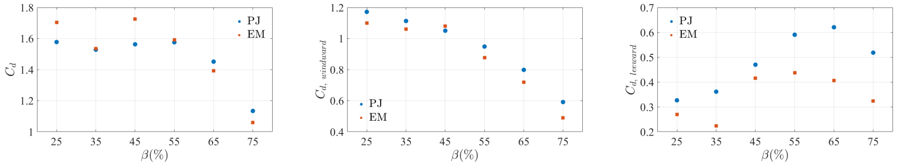

(a) (b) (c)

Figure 4.29: The drag coefficient, C_d, measured on (a): overall cylinder, (b): the windward surface and (c): the leeward surface of URANS cases when an attack angle of 9° is adopted.

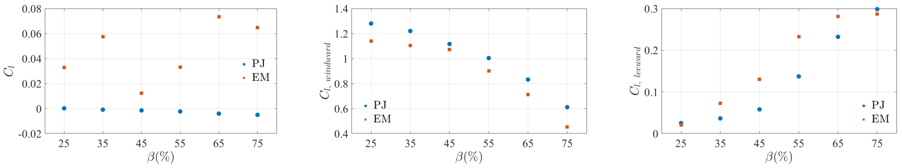

(a) (b) (c)

Figure 4.30: The lift coefficient, C_l, measured on (a): overall cylinder, (b): the windward surface and (c): the leeward surface of URANS cases when an attack angle of 3° is adopted.

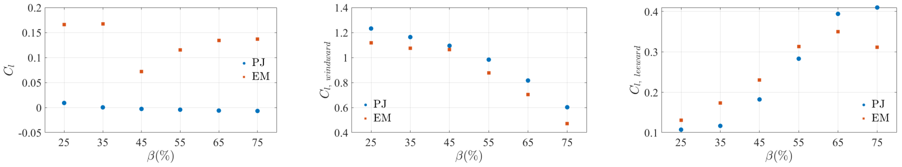

(a) (b) (c)

Figure 4.31: The lift coefficient, C_l, measured on (a): overall cylinder, (b): the windward surface and (c): the leeward surface of URANS cases when an attack angle of 6° is adopted.

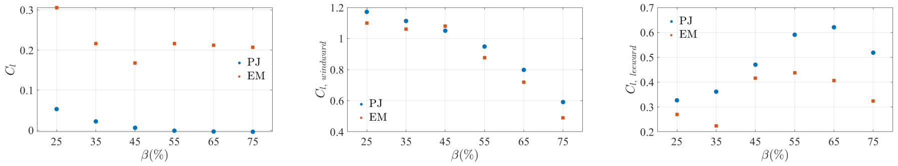

(a) (b) (c)

Figure 4.32: The lift coefficient, C_l, measured on (a): overall cylinder, (b): the windward surface and (c): the leeward surface of URANS cases when an attack angle of 9° is adopted.

Chapter 5

Simulation of wind shields and porous barriers strategies for bridge deck optimization

Wind shields and porous barriers are often positioned on bridge decks as ancillary structures. While being irrelevant from the structural point of view, it is well-known that their presence can deeply affect the deck aerodynamic performance. In particular, not only do they generally lead to an increase of the drag force, but also they modify the overall flow arrangement, so affecting all aerodynamic coefficients. In this paper, the numerical simulation of porous elements positioned on bridge sections is addressed following two approaches: in the first one, the pores are explicitly modeled, while in the second one a more convenient pressure-jump approach is adopted. In particular, the second approach has strong advantages compared to the first one, especially when simulations are used for optimization. The results obtained using these approaches are compared with each other and experimental measurements, highlighting strengths and limitations of both methodologies.

This chapter has been published as:

Simulation strategies for wind shields and porous barriers for bridge deck optimization. M. Xu, L. Patruno, Y.L. Lo, S. de Miranda, *Structures*, 40 (2022), 824-839.

5.1 Introduction

Wind shields and porous barriers are often positioned on bridge decks in order to protect vehicles from strong cross-wind [122, 45, 123]. Despite being considered ancillary structures, it is well-known that their presence can strongly affect the bridge aerodynamic performance. Several studies based on wind-tunnel experiments can be found in the literature, in which the effects of the barriers porosity and position have been studied taking into account both static and dynamic aerodynamic coefficients (see for instance [2, 124, 125]).

It must be noticed that the presence of porous barriers poses several problems from the experimental point of view. In particular, the dimensions of the pores, including all parts which allow airflow, are generally one to three orders of magnitude smaller than the overall deck dimensions. In such conditions, it is often impossible to accurately reproduce the barrier geometry, unless very large wind tunnel models are adopted. More often, the presence of the barriers is reproduced ensuring the matching of the drag coefficient of the full-scale barrier and that mounted on the model, without reproducing its geometry in detail. When such simplified barriers are obtained by means of circular sections, their size is usually so small that the Reynolds number dependency of the drag coefficient shall be considered. Other problems arise due to the substantial impossibility to measure pressure directly on the barriers, so that usually the drag force can be obtained only by balance measurements over the entire deck section.

Due to their ubiquitous presence, studies on the aerodynamics of isolated porous barriers have been repetitively presented in the literature. In particular, ground mounted configurations are experimentally analyzed by [126, 9, 35, 127]. Additionally, the reverse flow produced on the leeward side has been considered by [128] while the bleed flow is addressed in [129].

In the last decades, computational wind engineering has rapidly grown and the numerical simulation of bridge decks has been addressed since its early stages [130, 131]. Unfortunately, while numerous studies are present on bare decks, taking into account auxiliary elements and, in particular, wind shields and porous barriers is still cumbersome. In fact, explicitly modeling the small scale geometric features of such elements requires extremely fine meshes, which substantially increases the computational costs.

Actually, two modeling approaches can be adopted in the numerical simulation of porous barriers: 1) explicit modeling (*EM*) of the porous element geometry and 2) appropriately defined pressure-jumps (*PJ*), [66, 32]. The latter approach, which can be considered an homogenization technique, takes into account the presence of pores without reproducing the flow details. Analogously to the procedure followed in building reduced scale models for experimental testing, the technique is based on the reproduction of the porous element drag coefficient.

Currently, the use of pressure-jumps for modeling porous surfaces in Computational Fluid Dynamics, CFD, simulations is well-established for internal aerodynamics (e.g. flows through confined porous screens and filters) whereas regarding external flows, the pressure-jump approach has not been sufficiently and systematically investigated yet. This is particularly true for porous elements in proximity bluff-bodies such as bridge decks, the aerodynamics of which is notoriously complex and often sensitive to geometric details and incoming flow characteristics. However, for the sake of completeness, we here recall that related contributions have been presented for the CFD simulation of actuator disks [99, 100, 80] and ground-mounted porous fences [98, 65, 132, 133].

In this paper, we investigate the numerical simulation of porous elements positioned on bridge sections using the two aforementioned approaches, *EM* and *PJ*. Due to the aforementioned sensitivity of external flows around bluff-bodies to geometrical details and local flow conditions, the use of homogenization techniques for the representation of porous surfaces shall be carefully validated even if their use is already well-established for simple internal flows. Beside the computational efficiency, it should be also added that, for preliminary simulations, the *PJ* approach has the inherent advantage of allowing for varying the porous barrier height and porosity without remeshing. This leads to substantial savings in the pre-processing time when dealing with multiple configurations. This aspect of the *PJ* approach is particularly important for optimization-oriented studies, which currently represent an important application of numerical simulations.

Here we focus on two-dimensional Unsteady Reynolds-Averaged Navier-Stokes, 2D-URANS, based models and consider the experimental results reported in [2, 124, 125]. It should be noticed that, despite their well-known limitations, 2D-URANS are currently the most widely adopted numerical model typology for the study of bridge decks, especially for preliminary and optimization analyses [134]. In fact, despite their difficulties in accurately reproducing flows characterized by strong unsteadiness and the impossibility to represent three-dimensional flow features, they are often found effective in representing the time-averaged flow and its modification within small angles of attack.

In order to assess the accuracy of the two aforementioned modeling strategies, the flow field and aerodynamic coefficients predicted by the two approaches are compared with each other and with experimental results. Attention is posed in individuating and discussing critical aspects which might compromise the simulations predictive capability.

The paper is organised as follows. In Section 5.2, a brief description of the wind tunnel experiments used as a reference is reported. The adopted numerical models are described in Section 5.3. Results obtained using the two aforementioned modeling approaches are reported in Section 5.4 and, finally, conclusions are drawn in Section 5.5.

5.2 Experimental setup

In this section, the wind tunnel experiments reported by [2, 124, 125], used for numerical simulation validation purposes, are briefly described.

Wind tunnel experiments have been performed in a closed-circuit boundary-layer climatic wind tunnel with 1.9 m wide and 1.8 m high testing section. The incoming flow is uniform along the wind tunnel cross-section and the turbulence intensity is less than 2%. Within the geometries studied experimentally, we focus on the Great Belt Bridge, *GBB* and the Kao-Pin Hsi Bridge, *KPHB*. The first one has a streamlined section while the second can be considered a semi-bluff section. The considered geometries are reported in Fig. 5.1. In particular, the cross-wind dimensions (D) of the two bridge deck models are 0.04 m and 0.032 m, respectively. The other dimensions are reported in Table 5.1. The Reynolds number based on B is equal to approximately 3.0×10^5.

Regarding the geometry of the porous barriers, it should be noticed that, besides the elements characterized by triangular cross-section represented in Fig. 5.1, several vertical supports are present. As it will be later further discussed, such elements cannot be taken into account in the following analyses, which as already stated are two-dimensional. Additionally, it must be noticed that the windward (*W*) and leeward (*L*), barriers have different orientations with respect to incoming flow. Aerodynamic coefficients are defined as

$$C_d = \frac{F_D}{0.5\rho U_0^2 D}, \quad C_l = \frac{F_L}{0.5\rho U_0^2 B}, \quad C_m = \frac{M}{0.5\rho U_0^2 B^2}, \tag{5.1}$$

where ρ is the fluid density, U_0 is the incoming velocity while F_D, F_L, M are the aerodynamic drag force, lift force and pitch moment, respectively.

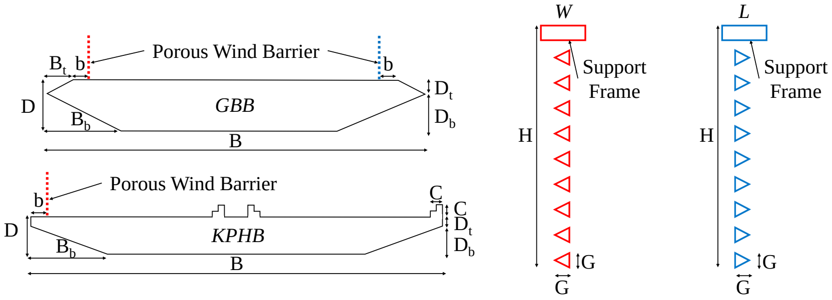

(a) (b) (c)

Figure 5.1: The models used in the wind-tunnel experiments: (a) the Great Belt Bridge, *GBB*, and the Kao-Pin Hsi Bridge, *KPHB*, (b) the windward porous barrier, *W*, and (c) the leeward porous barrier, *L*.

Table 5.1: The geometrical parameters of the considered bridge decks and porous barriers.

	B/D	H/D	G/D	D_t/D	D_b/D	b/D	B_t/D	B_b/D	C/D
GBB	7.75	1.25	0.075	0.25	0.75	0.13	0.50	1.50	-
KPHB	10.94	1.56	0.094	0.25	0.75	0.16	-	2.06	0.16

5.3 Numerical setup

In this section, the computational models and the numerical setup are firstly described. A validation of the model is then presented while the model sensitivity to various modeling choices and parameters is analysed in the Appendix, for the sake of conciseness. Then, the calibration of the pressure-jump is addressed.

5.3.1 Computational model

An overview of the adopted computational domain and the adopted reference system is shown in Figure 5.2. The domain is such that $D_x = 20B$ and $D_y = 15B$, leading to a blockage ratio equal to 0.87%. Moreover, the pressure probes are arranged along the path s, which starts from the windward corner. Figure 5.3 reports the four deck configurations considered in this study. Three of them are obtained starting from the *GBB* deck mounting the porous barriers only on the windward side, *GBB-W*, the leeward side, *GBB-L* and on both of them, *GBB-Both*. The fourth case is the *KPHB* deck with windward barrier only, denoted as *KPHB-W*. According to wind tunnel experiments reported by [2], the aerodynamic force and moment coefficients prove to be nearly constant when the Reynolds number based on B is larger than 2.0×10^5, so that 2.5×10^5 is here used.

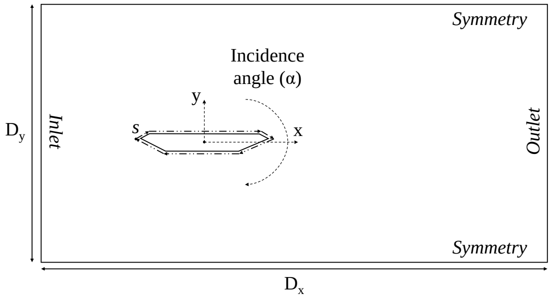

Figure 5.2: Overview of the adopted computational domain and reference system.

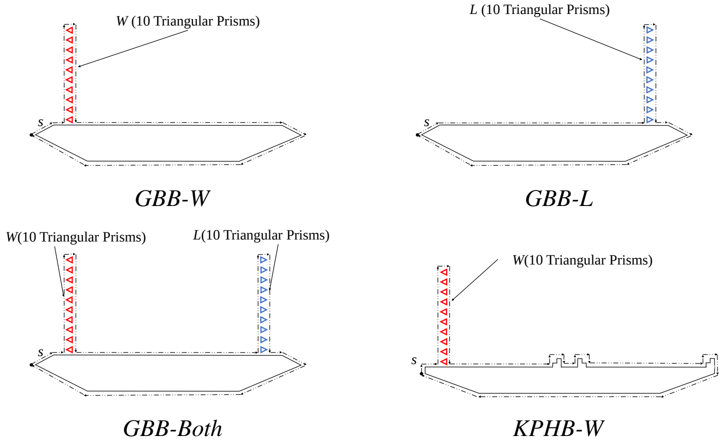

Figure 5.3: Geometry of the configurations used in the CFD analyses. The path used to represent pressure statistics can be observed.

Regarding boundary conditions, a fixed velocity, U_0, is prescribed at the inlet together with a null pressure gradient, while a pressure outlet is adopted at the outflow. The inlet turbulence intensity is set to 2%, as given in the referred experiments ([2]), while turbulent viscosity ratio is set to 2. Symmetry boundary conditions are imposed at the top and bottom of the domain while low-Reynolds number wall functions are adopted at the deck walls.

A centered, second-order differentiation scheme is adopted for the diffusive terms, while for non-linear advective terms, the Linear-Upwind Stabilised Transport (LUST) scheme is used. Time integration is performed using the Crank-Nicolson scheme with time step, dt, such that $dtU_0/B \approx 2.5 \times 10^{-4}$. The coupling of pressure and velocity is obtained for all simulations by using the well-known Pressure-Implicit with Splitting of Operators (PISO) algorithm. The open source Finite Volume software OpenFOAM 6 is adopted.

Each of the considered geometries is firstly simulated taking into account the detailed porous barrier geometry, as shown in Fig. 5.3. Then the *PJ* approach is used (i.e. the barrier is treated as a vanishing thickness baffle). The adopted meshes count approximately 180 k cells.

Many available URANS turbulence models require the calculation of wall-distance [118]. However, the use of such quantity requires reconsideration when considering porous elements, as the nature itself of the porous barrier might range from a substantially solid wall to a completely permeable element. We thus proceed using a wall-distance-free turbulence model, namely the Shih's quadratic algebraic Reynolds stress $k-\varepsilon$ model [119]. Notice that such turbulence model is not the standard $k-\varepsilon$, which often shows poor performance in the context of bluff-body aerodynamics.

5.3.2 Model validation

Before proceeding, we validate the adopted model by comparing the obtained results with experimental measurements for bare deck conditions. In particular, Fig. 5.4 shows the instantaneous velocity fields, U/U_0, of *GBB-Bare* when the incidence angle, α, is equal to $\pm 10^\circ$ and 0°.

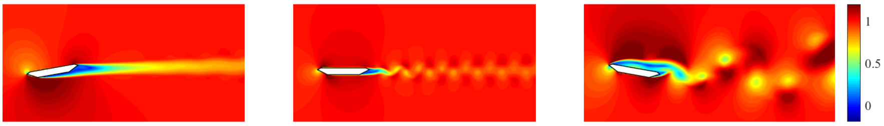

GBB-Bare, $-10°$ *GBB-Bare*, $0°$ *GBB-Bare*, $10°$

Figure 5.4: The instantaneous velocity magnitude fields, U/U_0, of the *GBB-Bare* configuration.

The corresponding aerodynamic coefficients are compared with experimental ones in Fig. 5.5. It can be seen that an overall good agreement is obtained between the numerical and the experimental predictions, being the most apparent difference a systematic under-prediction of the drag coefficient for the *KPHB-Bare* case. Despite that, results appear to be in good agreement and trends are always correctly captured.

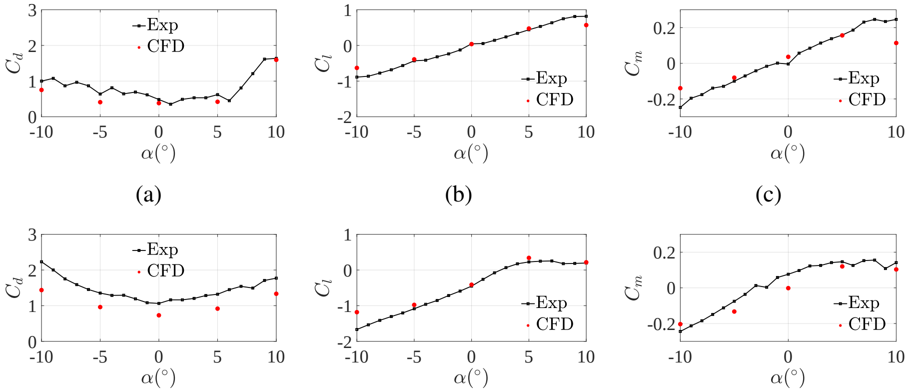

(a) (b) (c)

(d) (e) (f)

Figure 5.5: Aerodynamic force coefficients for bare deck condition: (a), (b) and (c) are C_d, C_l and C_m for *GBB-Bare*, respectively and (d), (e) and (f) are C_d, C_l and C_m for *KPHB-Bare*, respectively.

In fact, the presented validation is only partial and, indeed, insufficient for a careful validation of the model sensitivity to many choices/parameters which might affect the simulations results. There are three aspects which we considered worth further investigations in order to exclude a strong model sensitivity to the adopted modeling choices, namely:

1. simplifications introduced in the porous barriers geometry;
2. adopted turbulence model;
3. mesh sizing.

The sensitivity of the results to all such choices/parameters is reported in the Appendix, for the sake of readability. In particular, such aspects are investigated in 5.6.1, 5.6.2 and 5.6.3, respectively. Overall, as expected, some sensitivity can be observed, mainly related to local effects. Such slight dependencies proved to be much harder to be completely eliminated than for solid bridge deck sections, due to the presence of the barriers. Fortunately, this leads only to minor changes (usually in the order of 15%) in the overall forces on the deck and do not affect the observed trends. While not excluding the possibility to build slightly more accurate models increasing the computational costs, we proceed with the setups described above, keeping in mind that the main target of 2D-URNAS simulations are often preliminary and optimization studies.

5.3.3 Pressure-jump calibration

As it is well-known, the use of homogenized models in order to account for the presence of porous barriers (i.e. the *PJ* approach) requires to calibrate the loss coefficient. In the following, we detail such calibration and we highlight some of the problems and limitations which might be encountered when using such an approach.

In particular, the pressure jump, Δp, measured between the windward and leeward side of the porous barrier can be expressed for high Reynolds numbers (i.e. disregarding viscous contributions) as

$$\Delta p = \frac{1}{2}\rho U_n^2 K, \tag{5.2}$$

where U_n is the velocity normal to the porous barrier and K is the loss coefficient. Many empirical or semi-empirical laws able to predict K as a function of porosity, β, can be found in the literature [36, 78, 77, 79]. Recently, a semi-analytical law, valid in the case of porous barriers of vanishing thickness has been proposed in the author's previous work [113].

Some important aspects which shall be considered when using the *PJ* approach are listed below:

1. Δp must be equal to the drag force per unit area measured on the porous barrier, so that the loss coefficient is actually equal to the drag coefficient

per unit area;

2. when modeling the barrier geometry, after the barrier a pressure recovery zone is present, which extends downstream up to complete homogenization of the velocity distribution [113];
3. the along-wind dimension of such pressure recovery zones scales with the pore size;
4. the *PJ* approach assumes vanishing pore dimensions, so that the pressure recovery zone size vanishes and, so, it is not observed;
5. when using the *PJ* approach, it is assumed that the incidence angle of the incoming flow is equal to that of the outgoing one (i.e. the incoming flow is not deviated by the barrier).

In order to further investigate such aspects, we simulate the adopted barriers isolated from the deck, using periodic boundary conditions on the top and bottom boundaries of the domain. This configuration is considered as representative of an infinitely high barrier, as shown in Fig. 5.6. Numerical settings are the same as the ones previously described for the analysis of the decks. In order to ensure consistency between the deck simulations and these ones, the mesh was generated in a similar manner as for the barriers standing on the decks.

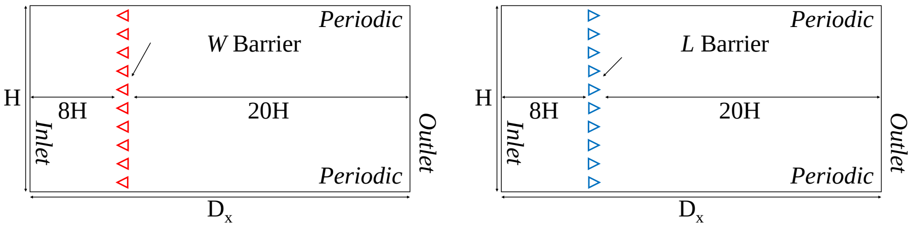

(a) (b)

Figure 5.6: Overview of the computational domain used for the simulation of the porous barriers in periodic conditions: (a) the windward, *W*, barrier and (b) the leeward, *L*, barrier.

The streamlines of the time-averaged velocity field obtained considering different inflow angles, α, are reported in Fig. 5.7. It can be easily noticed that a deflection of the flow is actually present. In particular, the *W* configuration appears to have a stabilizing effect with respect to the inflow angle, tending to produce an outgoing flow which is approximately directed along the normal to the barrier, regardless the incoming flow angle. On the other side, the *L* configuration tends to amplify the inflow angle, so leading to outgoing flows which are strongly skewed with respect to the barrier normal.

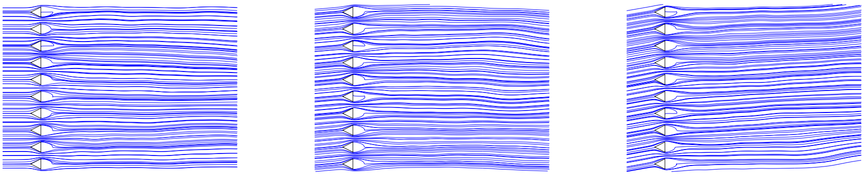

(a) *W*, $\alpha = 0^\circ$ (b) *W*, $\alpha = 5^\circ$ (c) *W*, $\alpha = 10^\circ$

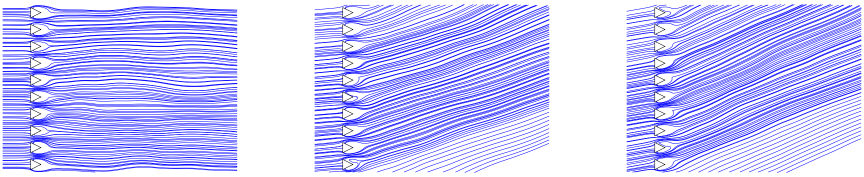

(d) *L*, $\alpha = 0^\circ$ (e) *L*, $\alpha = 5^\circ$ (f) *L*, $\alpha = 10^\circ$

Figure 5.7: Streamlines of the time-averaged velocity field around the porous barriers in periodic conditions: (a), (b) and (c) refer to the windward, *W*, barrier while (d), (e) and (f) refer to the leeward, *L*, barrier.

It should be also noticed that, as the aerodynamics of the barrier is substantially different when it is crossed in the two directions, differences in terms of drag coefficient might be also expected. The loss coefficient, K, for all analysed cases is reported in Table 5.2. It can be seen that values for the *W* and *L* configurations are actually quite similar (especially with respect to the range of variation of the K reported by [113]) and correspond to a perforated plate of vanishing thickness with $\beta = 44 - 45\%$. This allows to use the same K for both *W* and *L* barriers which, in principle, shall be separately calibrated.

Table 5.2: The drag coefficient, K, of the *W* and *L* barriers in periodic conditions. Comparison is provided with the formula reported in [113] indicated as *PJ*.

	α	*W*	*L*	*PJ*, $\beta = 44\%$	*PJ*, $\beta = 45\%$
C_d	0°	5.6456	6.1555	6.031	5.679
	5°	5.4050	6.1766	6.008	5.657
	10°	5.4685	5.9846	5.939	5.593

Although, as already stated, the flow deflection cannot be taken into account when using the *PJ* approach, a simple momentum balance in the direction parallel to the barrier (vertical direction in Fig. 5.6) shows that twice the deflection angle, $2\Delta\alpha$, is roughly equal to the lift coefficient per unit barrier area (valid for small incidence angles and deflections). Table 5.3 reports the measured lift coefficient and the deflection angle, measured directly over a representative streamline (in radians), showing good agreement between the two. This phenomenon appears to be one of the main limitations of *PJ* based simulations for bluff-body aerodynamics and surely deserves further research. Very interesting developments on such regard have been recently proposed in [135].

Table 5.3: The lift coefficient of the *W* and *L* barriers in periodic conditions and the flow deflection, $\Delta\alpha$.

	W,0°	*W*,5°	*W*,10°	*L*,0°	*L*,5°	*L*,10°
C_l	0.00	0.15	0.31	0.01	-0.44	-0.45
$2\Delta\alpha$	0.00	0.17	0.28	0.00	-0.45	-0.49

5.4 Results

In this section, we compare the results obtained by using *EM*, *PJ* and experiments. Firstly the obtained flow fields are analyzed, then global forces are considered.

5.4.1 Flow Patterns

The non-dimensional instantaneous velocity magnitude distributions, U/U_0, predicted for the *GBB-W* configuration are reported in Fig. 5.8 for various attack angles, for both *EM* and *PJ* models. The topological changes with respect to the bare deck conditions appear to be similar when comparing the two approaches, although differences in the vortex shedding mechanism can be observed.

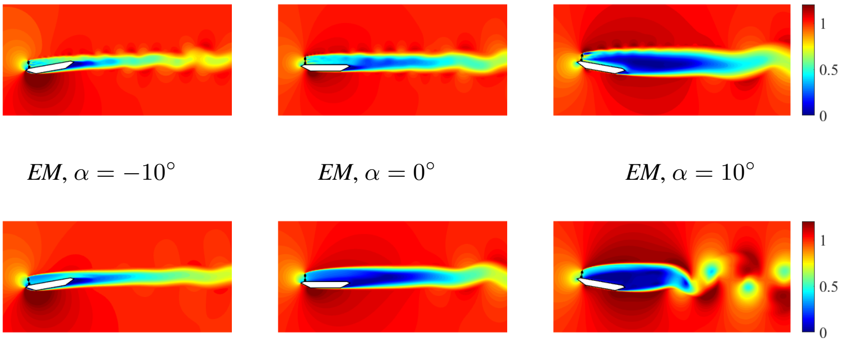

EM, $\alpha = -10°$ *EM*, $\alpha = 0°$ *EM*, $\alpha = 10°$

PJ, $\alpha = -10°$ *PJ*, $\alpha = 0°$ *PJ*, $\alpha = 10°$

Figure 5.8: The instantaneous velocity magnitude fields, U/U_0, for the *GBB-W* configuration.

Figure 5.9 shows U/U_0 for the *GBB-L* configuration. In this case, negative attack angles appear to be particularly well-predicted, while the null angle of attack leads to the most evident qualitative differences. In particular, in this case it is possible to observe an intensification of the velocity at the upper and lower ends of the porous barrier for *EM*, which is not observed in the *PJ* model.

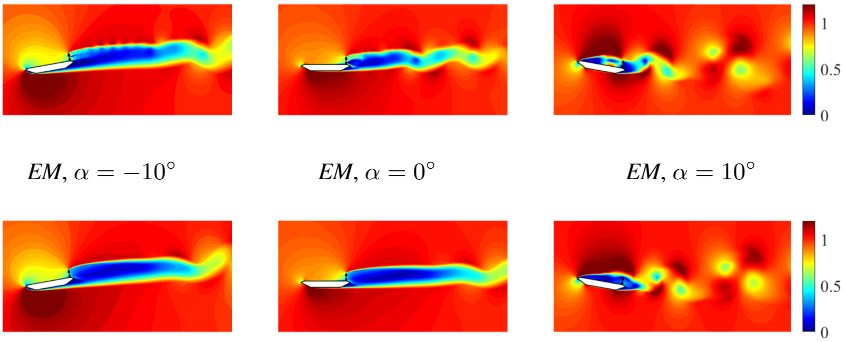

EM, $\alpha = -10^\circ$ *EM*, $\alpha = 0^\circ$ *EM*, $\alpha = 10^\circ$

PJ, $\alpha = -10^\circ$ *PJ*, $\alpha = 0^\circ$ *PJ*, $\alpha = 10^\circ$

Figure 5.9: The instantaneous velocity magnitude fields, U/U_0, for the *GBB-L* configuration.

For the sake of completeness, Fig. 5.10 reports U/U_0 for the *GBB-Both* configuration. Overall, results already presented for *GBB-W* and *GBB-L* are confirmed. The main topological changes with respect to bare deck conditions are captured but some flow details, as expected, are not reproduced. These, once amplified downstream, can lead to visible differences between *EM* and *PJ* models in the flow patterns.

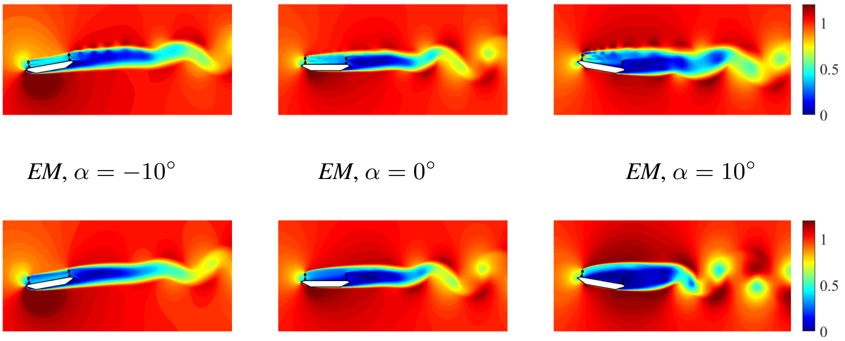

EM, $\alpha = -10^\circ$ *EM*, $\alpha = 0^\circ$ *EM*, $\alpha = 10^\circ$

PJ, $\alpha = -10^\circ$ *PJ*, $\alpha = 0^\circ$ *PJ*, $\alpha = 10^\circ$

Figure 5.10: The instantaneous velocity magnitude fields, U/U_0, for the *GBB-Both* configuration.

The instantaneous velocity fields close to the bridge decks are shown in Fig. 5.11, where the particle image velocimetry (PIV) technique is adopted in wind-tunnel experiments by [125]. For the convenience of comparison, the colormap of CFD results is set to be the same as the referred experimental work. Overall, similar flow patterns are obtained by experiments and CFD, being actually the *PJ* results sometimes in better qualitative agreement to experiments than *EM*. Such mismatches are mainly observed just downstream of the barriers, where strong bleed flows are predicted by the *EM* models, which are not observed in experiments. Considering that the barrier geometry has been explicitly modelled, this is unexpected and might be related to an excessive stability of the shear layers produced by the barrier, which do not lead to an effective mixing of the flow just downstream of it.

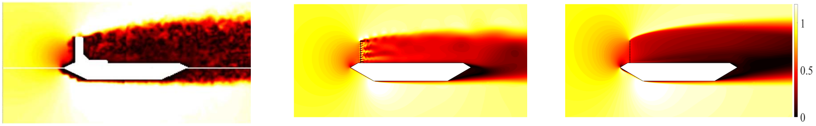

Exp, *GBB-W* *EM*, *GBB-W* *PJ*, *GBB-W*

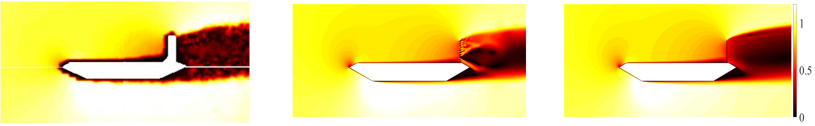

Exp, *GBB-L* *EM*, *GBB-L* *PJ*, *GBB-L*

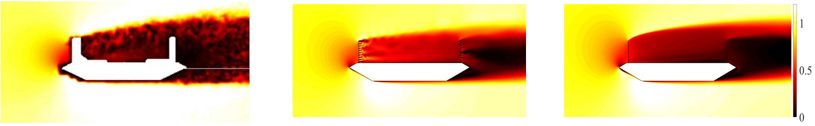

Exp, *GBB-D* *EM*, *GBB-D* *PJ*, *GBB-D*

Figure 5.11: The distributions of instantaneous velocity magnitude, U/U_0, around the bridge decks obtained by CFD and wind-tunnel experiments [125]. For the sake of comparison, the same colormap as the referred figures is used here for computed results.

To provide a clearer picture of the obtained results, Fig. 5.12 reports a close-up of the non-dimensional time-averaged velocity field for *GBB-W* at null angle of attack.

We notice the presence of a zone in which the velocity homogenizes downstream of the barrier in the *EM* model, which, as expected is not observed in *PJ* models.

This zone is also characterized by a pressure recovery and its downwind extension scales with the pore size as discussed, for instance in [113]. We also notice that a jump of the vertical velocity component is clearly observed for the *EM* model. In particular, the flow is almost horizontal downstream of the barrier, consistently with observations reported in Sec. 5.3.3. As expected, the *PJ* model does not show a jump on the vertical velocity component, i.e. the barrier does not deflect the incoming flow.

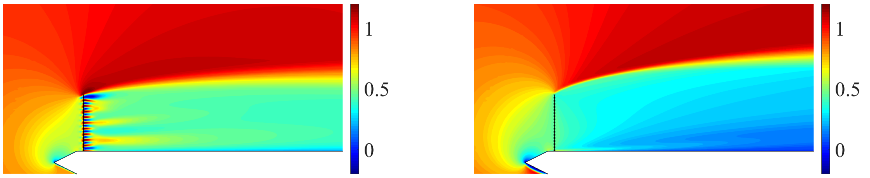

EM, $\overline{U}_x/U_0$ *PJ*, $\overline{U}_x/U_0$

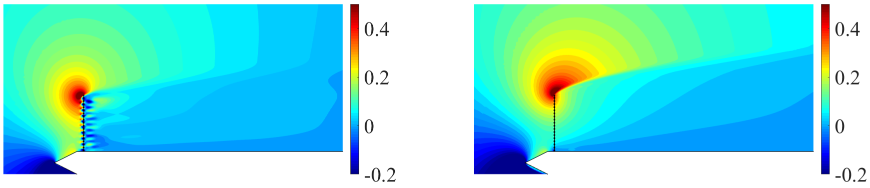

EM, $\overline{U}_y/U_0$ *PJ*, $\overline{U}_y/U_0$

Figure 5.12: Time-averaged velocity components distribution, $\overline{U}_x/U_0$ and $\overline{U}_y/U_0$, downstream of the porous barriers for the *GBB-W* at null incidence angle.

Figure 5.13 shows the streamlines of the time-averaged velocity field obtained for the *GBB-W* case. It can be seen that clear differences in the flow organization and the arrangement of recirculation zones emerge. The majority of such differences appear to be directly related to the incapability of pressure-jump based models to take into account the flow deflection induced by the presence of the barrier. This is further confirmed in Figs. 5.14 and 5.15 which represent streamlines for the *GBB-L* and *GBB-Both* configurations.

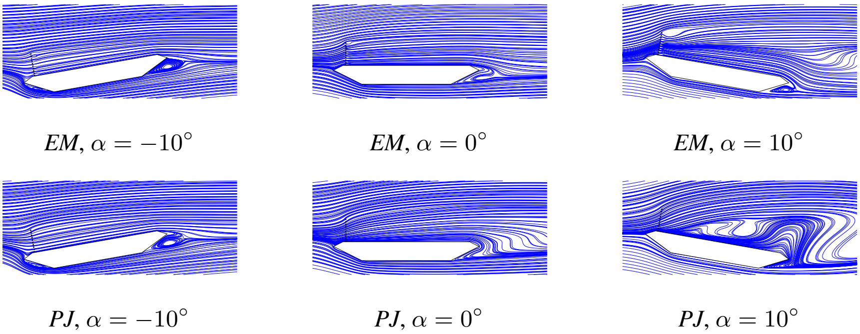

EM, $\alpha = -10^\circ$ *EM*, $\alpha = 0^\circ$ *EM*, $\alpha = 10^\circ$

PJ, $\alpha = -10^\circ$ *PJ*, $\alpha = 0^\circ$ *PJ*, $\alpha = 10^\circ$

Figure 5.13: Streamlines of the time-averaged velocity fields for the *GBB-W* configuration.

As an example let us consider the *GBB-Both* configuration at 10° reported in Fig. 5.15. Consistent with results reported in Sec. 5.3.3, the streamlines of the *EM* model deviate toward the barrier normal direction, becoming almost parallel to the deck surface. The *PJ* model is unable to predict such deflection and, thus, a different flow pattern emerges, in which a large separation is generated just after the windward barrier.

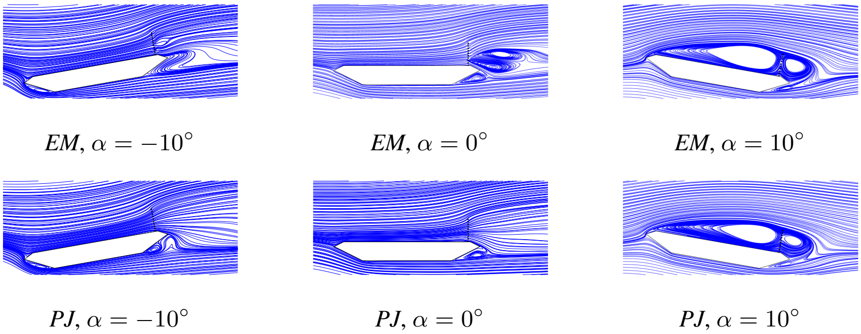

EM, $\alpha = -10^\circ$ *EM*, $\alpha = 0^\circ$ *EM*, $\alpha = 10^\circ$

PJ, $\alpha = -10^\circ$ *PJ*, $\alpha = 0^\circ$ *PJ*, $\alpha = 10^\circ$

Figure 5.14: Streamlines of the time-averaged velocity fields for the *GBB-L* configuration.

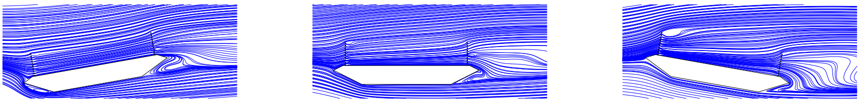

EM, $\alpha = -10^\circ$ *EM*, $\alpha = 0^\circ$ *EM*, $\alpha = 10^\circ$

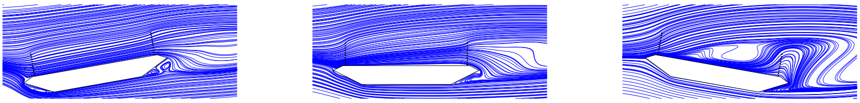

PJ, $\alpha = -10^\circ$ *PJ*, $\alpha = 0^\circ$ *PJ*, $\alpha = 10^\circ$

Figure 5.15: Streamlines of the time-averaged velocity fields for the *GBB-Both* configuration.

5.4.2 Pressure distributions and global forces

We now proceed to compare the results obtained with the *EM* and *PJ* models in terms of pressure coefficient distributions. The paths used to represent the position along the deck perimeter are reported in Fig. 5.1. In particular, Fig. 5.16 reports the time-averaged pressure coefficient, $\overline{C}_p$, distribution over the considered decks as a function of the non-dimensional coordinate s/B.

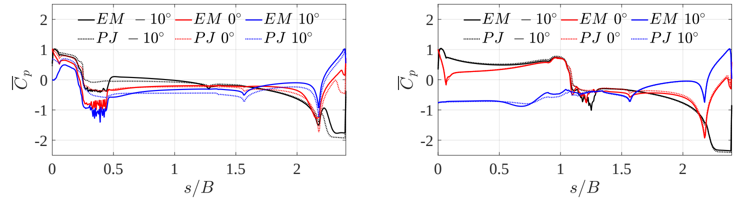

GBB-W *GBB-L*

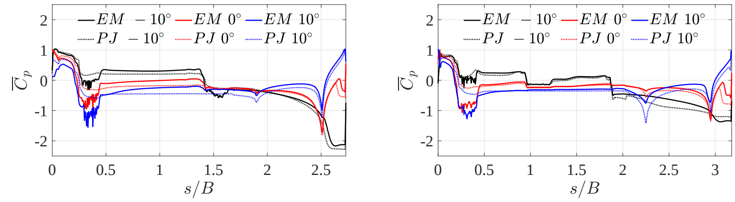

GBB-Both *KPHB-W*

Figure 5.16: Distribution of the time-averaged pressure coefficient, $\overline{C}_p$, for all the considered geometries at -10°, 0° and 10° angles of attack.

Pressure recovery zones just downstream of the barrier can be, for instance, observed at $s \approx 0.3$ in Fig. 5.16 for the *GBB-W* case for *EM*, which are not seen for *PJ*. Results obtained using *EM* and *PJ* models are in qualitative agreement but, from the quantitative point of view, slight differences are found. As expected, the *GBB-L* case is the one for which *EM* and *PJ* models show the best agreement, since the downstream barrier has a less impact on the flow field.

Figure 5.17 provides an overall picture of the obtained results in terms of global aerodynamic forces. We observe that the drag coefficient appears to be systematically underestimated by the current simulations. Further analyses, performed considering barriers with higher loss coefficients, which are not reported here for the sake of conciseness, demonstrated that such mismatches cannot be explained by inaccuracies in the considered barrier porosity: even considering solid barriers the drag force appears to be underestimated. We notice that a slight underestimation was recorded also in Sec. 5.3.2 for bare deck conditions, but the presence of the barriers surely increased the differences between experimental measurements and numerical results. The exact cause of such differences is unclear, although it should be noted that differences in the drag coefficient are often seen when comparing wind tunnel results to simulations based on 2D-URANS (however, in the authors experience, 2D-URANS more often lead to an overestimation of the drag force).

Nevertheless, the trends present in the experimental results appear to be well reproduced by the simulations. Additionally, the differences between *EM* and *PJ* models appear to be limited when compared to the mismatches with experimental measurements, so suggesting that, at least for the level of accuracy which can be obtained with 2D-URANS, *PJ* and *EM* approaches are substantially equivalent, despite being *PJ* based models much more convenient form the operative point of view.

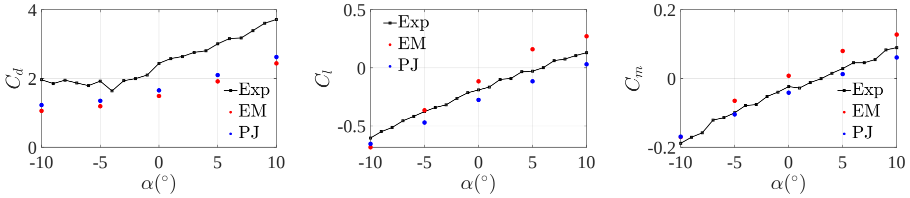

GBB-W *GBB-W* *GBB-W*

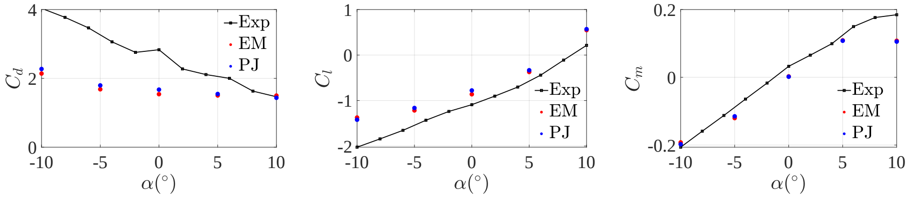

GBB-L *GBB-L* *GBB-L*

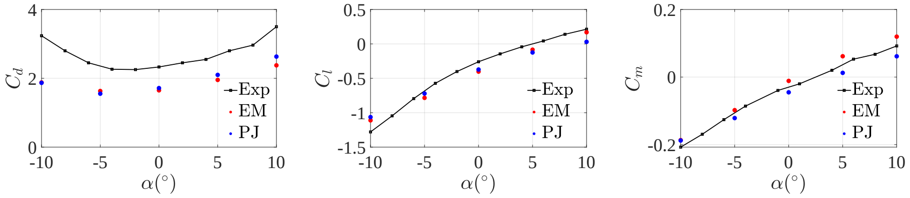

GBB-Both *GBB-Both* *GBB-Both*

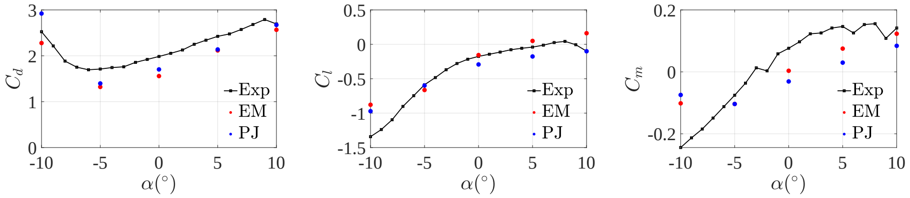

KPHB-W *KPHB-W* *KPHB-W*

Figure 5.17: The aerodynamic coefficients of the *GBB-W*, *GBB-L*, *GBB-Both* and *KPHB-W* configurations.

To provide a quantitative evaluation of such observations, the coefficient of determination, R^2, of the *EM* and *PJ* models is reported in Table 5.4. In reading such results it is worth to recall the R^2 is insensitive to shifting and scaling of the data, so that it mainly provides a measure of accuracy of the predicted trends. It can be seen that R^2 ranges from approximately 1 to 0.73 for *EM* and 0.63 for *PJ* without apparent trends, so confirming that *EM* models are only slightly better than *PJ* models in predicting the trends of the aerodynamic forces with respect to the angle of attack.

Table 5.4: The coefficient of determination, R^2, of the *EM* and *PJ* models for all analysed cases.

	GBB-W		*GBB-L*		*GBB-Both*		*KPHB-W*	
	EM	*PJ*	*EM*	*PJ*	*EM*	*PJ*	*EM*	*PJ*
C_d	0.990	0.991	0.732	0.891	0.757	0.638	0.989	0.861
C_l	0.991	0.999	0.966	0.983	0.971	0.991	0.853	0.961
C_m	0.996	0.997	0.975	0.978	0.997	0.995	0.801	0.632

Finally, Table 5.5 reports the mean errors obtained for each case for both *EM* and *PJ* models. The error is defined as

$$E = \frac{\sqrt{\sum \left(C_{Exp} - C_{CFD}\right)^2}}{\sqrt{\sum C_{Exp}^2}}, \tag{5.3}$$

where the C_{Exp} and C_{CFD} respectively represents the experimental and computed force coefficients. Again it emerges that sensitive mismatches with experimental measurements are present, but *EM* and *PJ* models are characterized by comparable accuracies.

Table 5.5: The errors between the computed and experimental force coefficients.

	GBB-W		*GBB-L*		*GBB-Both*		*KPHB-W*	
	EM	*PJ*	*EM*	*PJ*	*EM*	*PJ*	*EM*	*PJ*
C_d	0.378	0.310	0.442	0.408	0.336	0.312	0.139	0.126
C_l	0.347	0.255	0.303	0.313	0.175	0.223	0.369	0.279
C_m	0.347	0.181	0.286	0.287	0.185	0.191	0.532	0.718

5.4.3 Zero thickness porous barrier

In order to shed further light on the role played by porous barriers, the *GBB-W* configuration was simulated using the *EM* approach with a zero-thickness barrier, indicated as *EMz*. This approach represents an intermediate condition between the previously analysed *EM* and *PJ* models, as it is similar to *EM* with respect to the barrier drag production but it does not allow for a deflection of the flow, consistently with *PJ*. The obtained flow fields are shown in Fig. 5.18 and shall be compared to those reported in Fig. 5.13. The strong similarity between *PJ* and *EMz* models can be immediately observed.

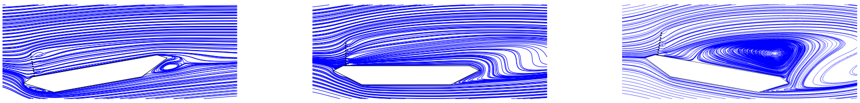

EMz, $\alpha = -10°$ *EMz*, $\alpha = 0°$ *EMz*, $\alpha = 10°$

Figure 5.18: Streamlines of the time-averaged velocity fields for the *GBB-W* configuration with a zero-thickness barrier.

The very good matching observed between *PJ* and *EMz* models is further confirmed in Fig. 5.19 and Fig. 5.20, where $\overline{C}_p$ distributions and global forces are reported at different angles of attack. This confirms the importance of considering the deflection of the flow operated by the barrier, that unfortunately cannot be considered when using standard PJ approaches, commonly available in commercial softwares.

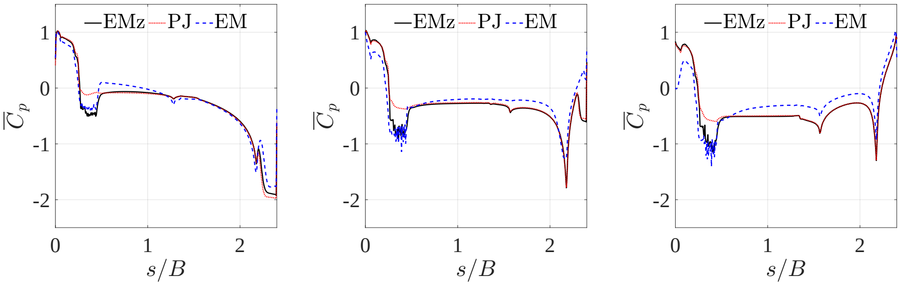

$\alpha = -10°$ $\alpha = 0°$ $\alpha = 10°$

Figure 5.19: The $\overline{C}_p$ distribution for the *GBB-W* case at different angles of attack.

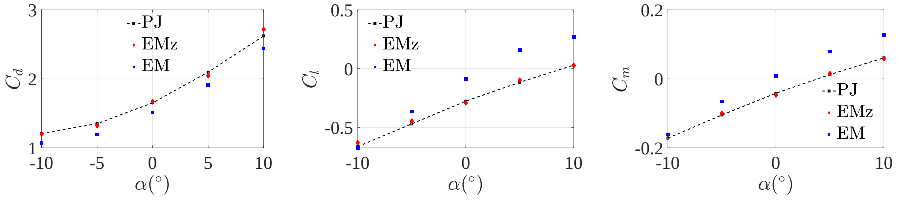

(a) (b) (c)

Figure 5.20: The aerodynamic coefficients for the *GBB-W* configuration when different modeling approaches and angles of attack are adopted: (a) C_d, (b) C_l and (c) C_m.

5.5 Conclusions

In this paper we investigated the role played by wind shields and porous barriers in the assessment of the bridge decks aerodynamic performances by means of CFD simulations. In particular, 2D-URANS models have been considered, due to their well-known good balance between accuracy and computational requirements, which currently renders them the most widely used model for bridge deck optimization in the early stages of the design development.

Firstly, we remark that the presence of the porous barriers generally led to a decrease of the accuracy of the simulations with respect to the bare deck conditions. Discrepancies may be attributed, at least partially, to mismatches in the model geometry (e.g. the impossibility to model vertical supports in 2D URANS) but this does not seem enough to explain the observed differences. Sensitivity analyses have been also used to investigate other sources of uncertainties, leading to the same conclusions. We individuate as an important limitation of PJ based models the impossibility to account for flow deflection, pointing to the need to develop *ad hoc* numerical models to represent the phenomenon. In the authors' experience, the use of Large Eddy Simulations might lead to major improvements, but for such cases preliminary evaluations suggest an increase of computational time of approximately three orders of magnitude, making them completely unsuitable for optimization purposes.

Despite some mismatches, numerical models were able to correctly reproduce most of the trends observed in experimental data when considering different barrier positions and angles of attack. Moreover, it has been shown that using homogenized models might be a convenient and viable solution with respect to explicit models for optimization purposes, since trends of the global aerodynamic forces were not substantially affected by such simplification.

5.6 Appendix

5.6.1 Sensitivity to frame geometry

As reported above, the vertical supports are disregarded in simulations as 2D-URANS are adopted. By ignoring such vertical supports the overall barrier porosity is changed by roughly 3%. Additional simulations obtained by varying the barrier porosity for PJ models, not here reported for the sake of brevity, shown very little sensitivity to such porosity differences. Additionally, for the sake of simplicity, the top railing is modelled as an additional triangular element in order to obtain an homogeneous barrier. We thus here assess the model sensibility to such geometric detail.

The instantaneous velocity fields obtained considering the real geometry instead of the simplified one (i.e. with the additional triangular element) are shown in Fig. 5.21. These can be compared to Fig. 5.8 (b) and 5.9 (b). Some differences emerge but they do not seem to lead to reproduce the PIV measurements any better.

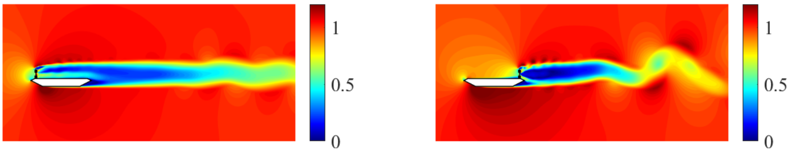

(a) (b)

Figure 5.21: The instantaneous velocity magnitude fields, U/U_0, for the geometry with the supporting frame horizontal element for: (a) *GBB-W* and (b) *GBB-L*.

Good agreements is still obtained in terms of global force coefficients, shown in Fig. 5.22. Differences between such two models for *GBB-W* and *GBB-L* are respectively 9.1% and 9.4%. While such differences are not necessarily negligible, explicitly modeling the top railing would strongly jeopardize most of the advantages obtained building a homogenized models. Without excluding the possibility to build more accurate models using mixed PJ/EM approaches, we here proceed with the simple PJ model and, for the sake of comparability, we replace the top railing with an additional triangle, so rendering the two models more fairly comparable (notice that the presence of top railing can be actually considered an artifact needed in wind-tunnel experiments). We nevertheless notice that the observed 10% differences are anyway not enough to explain some of the mismatches obtained with experimental data.

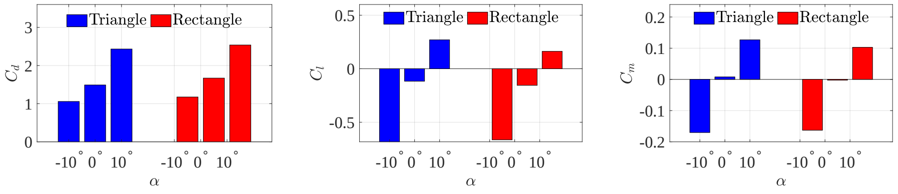

(a) *GBB-W* (b) *GBB-W* (c) *GBB-W*

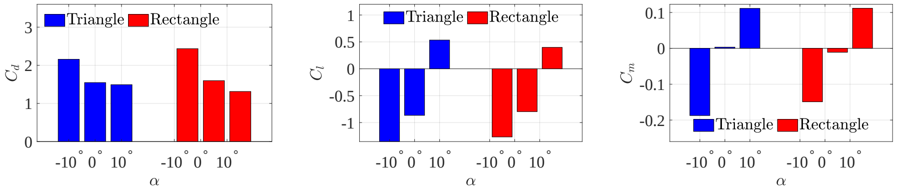

(d) *GBB-L* (e) *GBB-L* (f) *GBB-L*

Figure 5.22: Aerodynamic coefficient obtained with and without (substituting it with a triangular element) the barrier top frame: (a), (b) and (c) *GBB-W* and (d), (e), and (f) *GBB-L*.

5.6.2 Sensitivity to turbulence models

As reported in the manuscript, the Shih's quadratic algebraic Reynolds stress $k-\varepsilon$ is well-adapted to work in conjunction with *PJ* models as it is wall-distance free. Nevertheless, limiting to 2D-URANS, the $k-\omega\ SST$ model is well-known to provide good results for flows around bluff-bodies. We thus here assess the sensitivity of the results on the turbulence model using *GBB-W* and *GBB-L*.

The global aerodynamic coefficients obtained using Shih's $k-\varepsilon$ and $k-\omega\ SST$ models are shown in Fig. 5.23, where an overall good agreement can be found. In particular, the averaged difference of C_d between these turbulence models is approximately 4%.

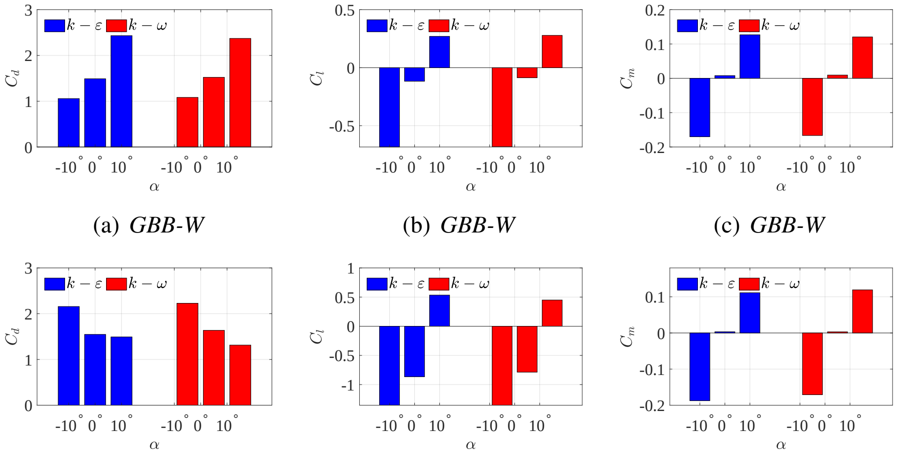

(a) *GBB-W* (b) *GBB-W* (c) *GBB-W*

(d) *GBB-L* (e) *GBB-L* (f) *GBB-L*

Figure 5.23: Aerodynamic coefficient obtained considering different turbulence models: (a), (b) and (c) *GBB-W* and (d), (e), and (f) *GBB-L*.

5.6.3 Sensitivity to the mesh

A mesh sensitivity analysis is performed on the *GBB-Bare*, *GBB-W* and *GBB-L* configurations. In particular, we firstly consider a baseline mesh characterized by along and cross-wind dimensions equal to $\delta_x/B = \delta_y/B = 8 \times 10^{-4}$ close to the considered bridge decks, just outside the boundary layers. Such mesh counts approximately 180 k cells. Two close-ups of the meshes are shown in Fig. 5.24.

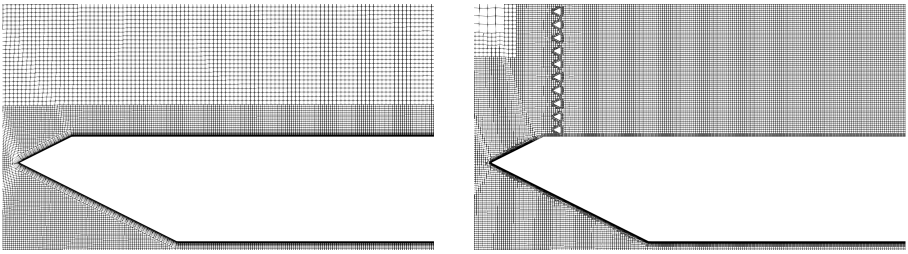

(a) (b)

Figure 5.24: Overview of the fine meshes: (a) *GBB-Bare* and (b) *GBB-W*.

Then, a finer mesh is considered. Such mesh is characterized by $\delta_x/B = \delta_y/B =$

4×10^{-4} and counts approximately 340 k cells. The time-averaged velocity magnitude distribution, $\overline{U}/U_0$, for the two mesh refinements is shown in Fig. 5.25.

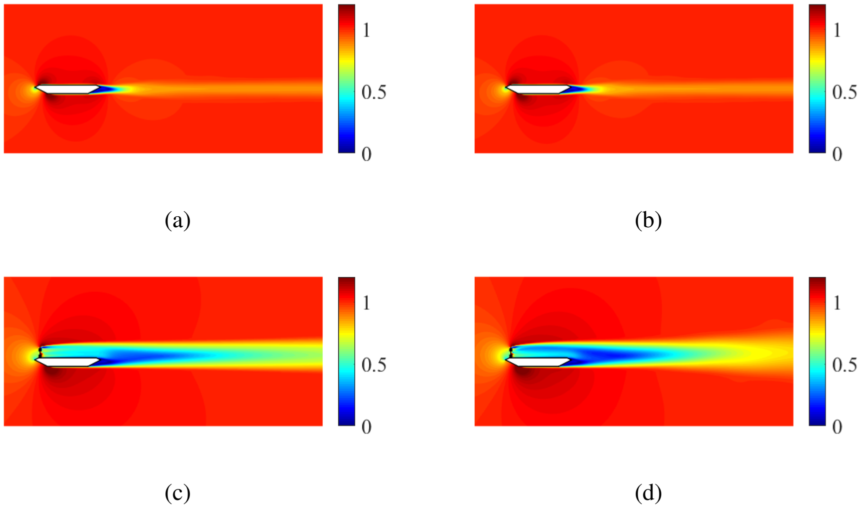

(a) (b)

(c) (d)

Figure 5.25: Time-averaged velocity field, $\overline{U}/U_0$: (a) *GBB-Bare* baseline, (b) *GBB-Bare* fine, (c) *GBB-W* baseline, (d) *GBB-W* fine.

While for *GBB-Bare* a very good agreement between the two is found, for the *GBB-W* some differences can be observed close to the barrier and in the far wake. As is discussed in [113, 120], due to the inherent multi-scale nature of the flow, a complete mesh insensitivity for cases in which the barrier geometry is modelled is extremely hard to be achieved. Indeed, it is the aim of homogenized models, such as the pressure-jump approach, to disregard some of the flow details in order to account only for the main flow features, relevant for the intended use of the analyses.

We thus proceed to compare the obtained pressure distributions. In particular, we define the pressure coefficient $C_p = \frac{\overline{p}}{0.5\rho U_0^2}$ as usual, where $\overline{p}$ denotes the time-averaged pressure. Figure 5.26 (a) and (b) report the time-averaged pressure coefficient distribution, $\overline{C}_p$, and its standard deviation, C_p', for *GBB-Bare*. The path along which the pressure statistics are sampled is shown in Fig. 5.3. It can be seen that, overall, a very good agreement is obtained.

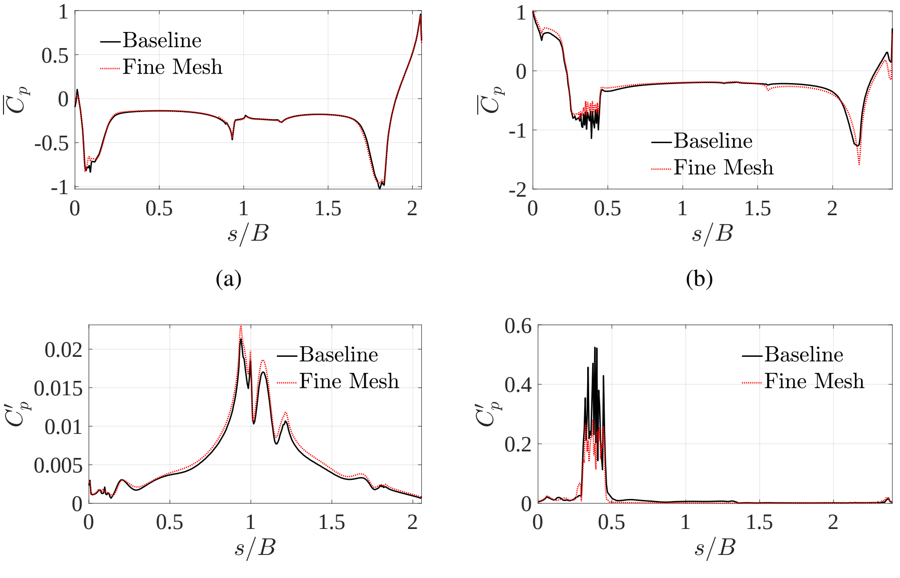

(a) (b)

(c) (d)

Figure 5.26: Pressure coefficient statistics: (a) *GBB-Bare* $\overline{C}_p$, (b) *GBB-W* $\overline{C}_p$, (c) *GBB-Bare* C'_p, (d) *GBB-W* C'_p.

When the $\overline{C}_p$ and C'_p for the *GBB-W* configuration are considered, we observe slight discrepancies, especially in the proximity of the barrier, which is shown in Fig. 5.26 (b) and (d). Such differences are related to the local unsteady behaviour of the flow over the pores, which cannot be well-captured by the baseline mesh. It should be noticed that the local flow behaviour inside the pores cannot be correctly considered neither by wind tunnel models based on the matching of the drag coefficient, nor by pressure-jump based models. Indeed, if such feature is deemed important, an accurate explicit modeling of the barrier aerodynamics appears to be the only solution for both physical models and numerical simulations, although cumbersome and impractical.

Finally, Table 5.6 reports the time-averaged force coefficients obtained for using the baseline and fine meshes for various deck configurations. We notice that one case, namely *GBB-L* at $\alpha = -10°$, shows a difference of 15% (which is anyway small with respect to the differences against experiments). Nevertheless, the overall agreement, especially in terms of drag coefficients, appears to be very good. We thus conclude that while adopting finer meshes might lead to some improvements (at a very high computational cost has thefiner mesh has been obtained by bisection in the barrier proximity), the observed differences with respect to experimental data cannot be attributed to mesh dependency of the results.

Table 5.6: The aerodynamic coefficients of the *GBB-Bare*, *KPHB-Bare*, *GBB-W* and *GBB-L* when different mesh resolutions are adopted. The B and F represent the case with baseline and fine mesh, respectively.

	C_d		C_l		C_m	
	B	*F*	*B*	*F*	*B*	*F*
GBB-Bare	0.382	0.390	0.038	0.029	0.036	0.036
KPHB-Bare	0.585	0.580	-0.466	-0.456	-0.002	-0.003
GBB-W, $\alpha = -10°$	1.058	1.134	-0.683	-0.667	-0.170	-0.166
GBB-L, $\alpha = -10°$	2.157	2.489	-1.353	-1.320	-0.187	-0.175
GBB-W, $\alpha = 0°$	1.490	1.523	-0.117	-0.162	0.008	-0.005
GBB-L, $\alpha = 0°$	1.547	1.561	-0.866	-0.873	0.003	0.002
GBB-W, $\alpha = 10°$	2.433	2.403	0.270	0.203	0.127	0.109
GBB-L, $\alpha = 10°$	1.492	1.340	0.534	0.524	0.111	0.108

5.6.4 The instantaneous velocity fields of all cases

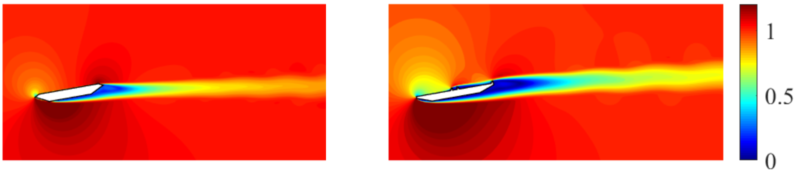

GBB Bare, -10° *KPHB Bare*, -10°

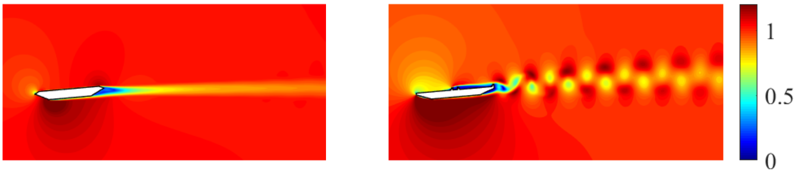

GBB Bare, -5° *KPHB Bare*, -5°

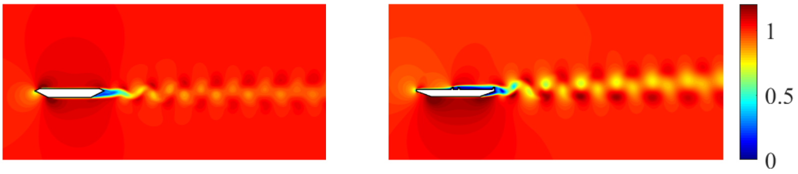

GBB Bare, 0° *KPHB Bare*, 0°

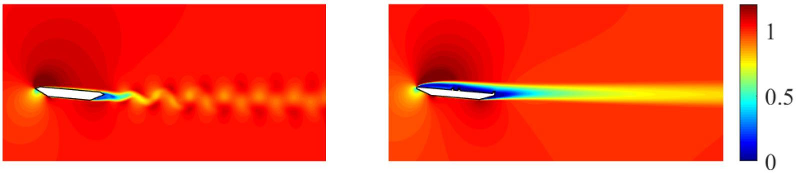

GBB Bare, 5° *KPHB Bare*, 5°

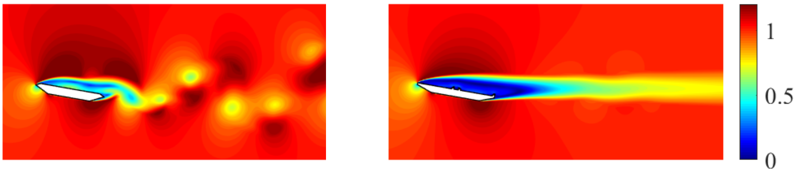

GBB Bare, 10° *KPHB Bare*, 10°

Figure 5.27: The instantaneous velocity fields, U/U_0, of the *GBB Bare* and *KPHB Bare*.

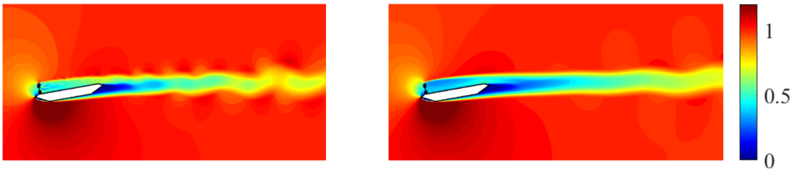

(a) *GB*, $\alpha = -10^\circ$ (b) *HB*, $\alpha = -10^\circ$

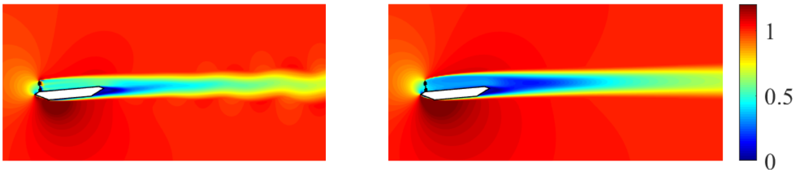

(c) *GB*, $\alpha = -5^\circ$ (d) *HB*, $\alpha = -5^\circ$

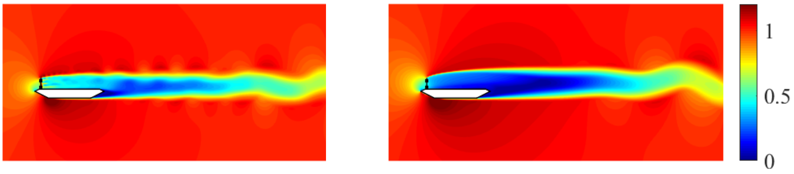

(e) *GB*, $\alpha = 0^\circ$ (f) *HB*, $\alpha = 0^\circ$

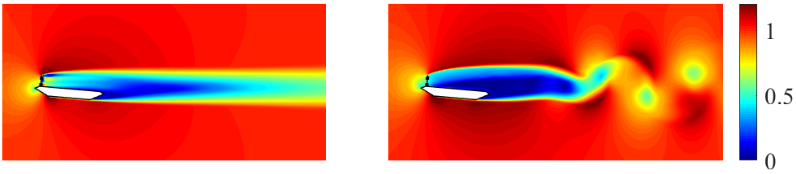

(g) *GB*, $\alpha = 5^\circ$ (h) *HB*, $\alpha = 5^\circ$

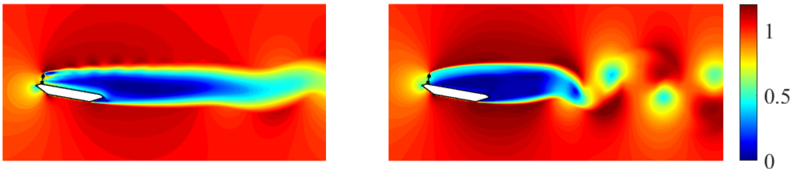

(i) *GB*, $\alpha = 10^\circ$ (j) *HB*, $\alpha = 10^\circ$

Figure 5.28: The instantaneous velocity fields, U/U_0, of the *GBB WW* when different incidence angles are adopted.

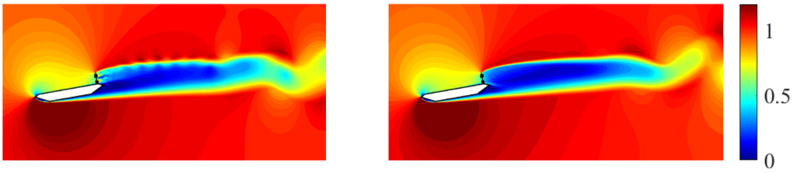

(a) *GB*, $\alpha = -10^{\circ}$ (b) *HB*, $\alpha = -10^{\circ}$

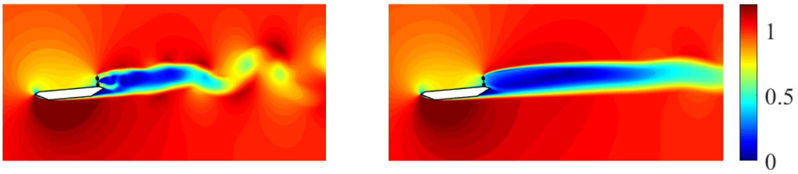

(c) *GB*, $\alpha = -5^{\circ}$ (d) *HB*, $\alpha = -5^{\circ}$

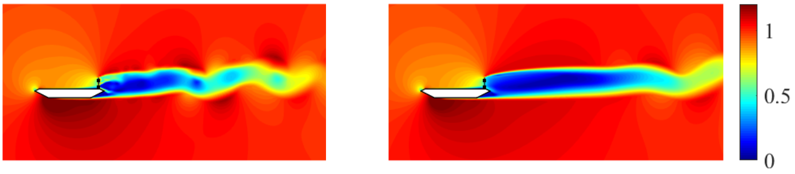

(e) *GB*, $\alpha = 0^{\circ}$ (f) *HB*, $\alpha = 0^{\circ}$

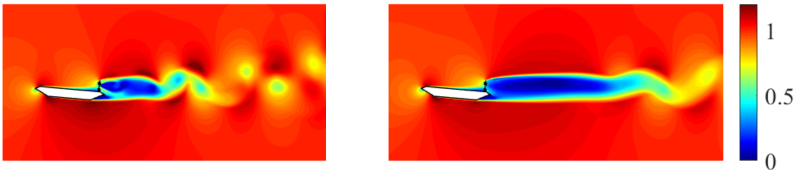

(g) *GB*, $\alpha = 5^{\circ}$ (h) *HB*, $\alpha = 5^{\circ}$

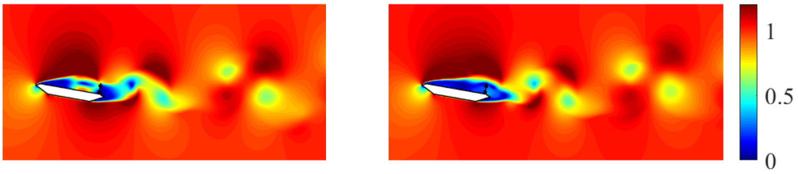

(i) *GB*, $\alpha = 10^{\circ}$ (j) *HB*, $\alpha = 10^{\circ}$

Figure 5.29: The instantaneous velocity fields, U/U_0, of the *GBB LW* when different incidence angles are adopted.

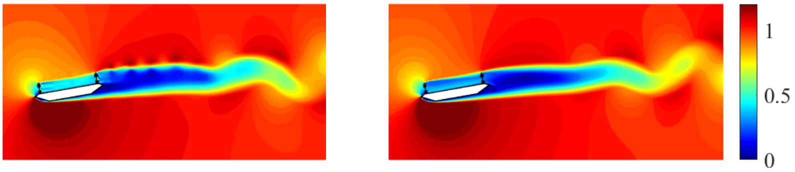

(a) *GB*, $\alpha = -10^\circ$ (b) *HB*, $\alpha = -10^\circ$

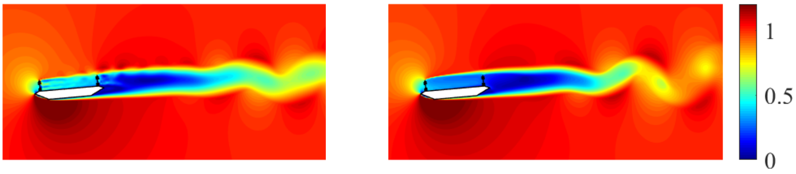

(c) *GB*, $\alpha = -5^\circ$ (d) *HB*, $\alpha = -5^\circ$

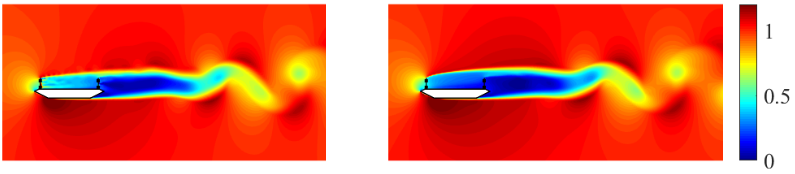

(e) *GB*, $\alpha = 0^\circ$ (f) *HB*, $\alpha = 0^\circ$

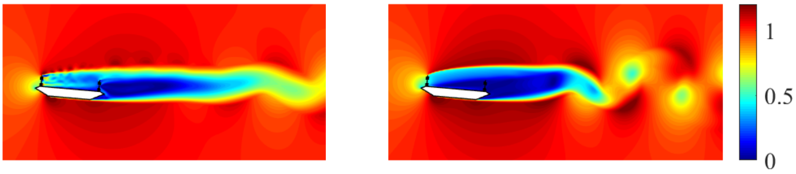

(g) *GB*, $\alpha = 5^\circ$ (h) *HB*, $\alpha = 5^\circ$

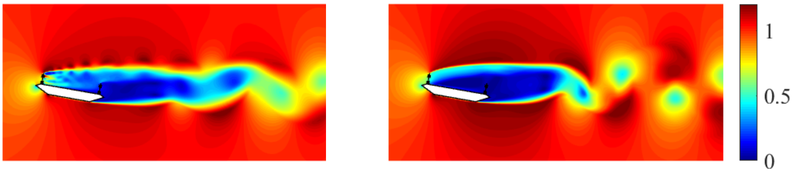

(i) *GB*, $\alpha = 10^\circ$ (j) *HB*, $\alpha = 10^\circ$

Figure 5.30: The instantaneous velocity fields, U/U_0, of the *GBB DW* when different incidence angles are adopted.

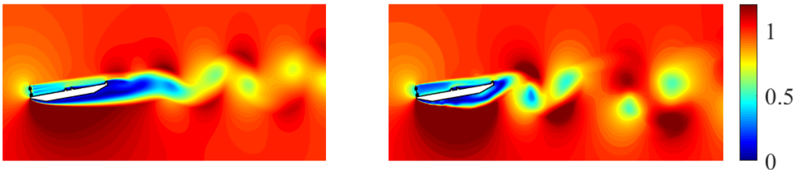

(a) *GB*, $\alpha = -10^\circ$ (b) *HB*, $\alpha = -10^\circ$

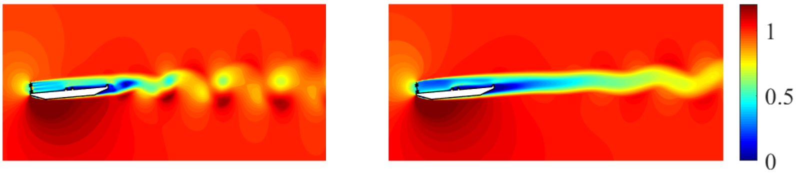

(c) *GB*, $\alpha = -5^\circ$ (d) *HB*, $\alpha = -5^\circ$

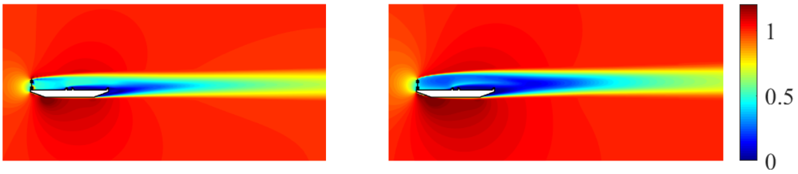

(e) *GB*, $\alpha = 0^\circ$ (f) *HB*, $\alpha = 0^\circ$

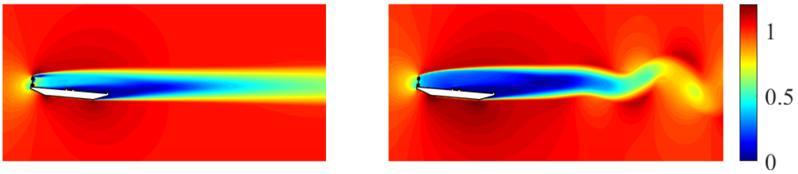

(g) *GB*, $\alpha = 5^\circ$ (h) *HB*, $\alpha = 5^\circ$

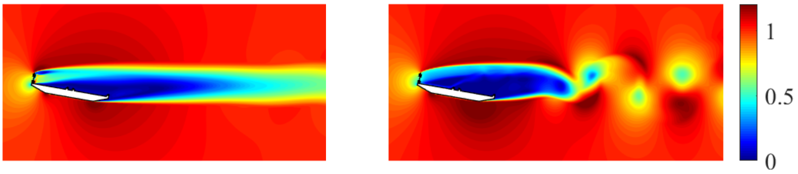

(i) *GB*, $\alpha = 10^\circ$ (j) *HB*, $\alpha = 10^\circ$

Figure 5.31: The instantaneous velocity fields, U/U_0, of the *KPHB WW* when different incidence angles are adopted. 133

5.6.5 The time-averaged velocity fields of all cases

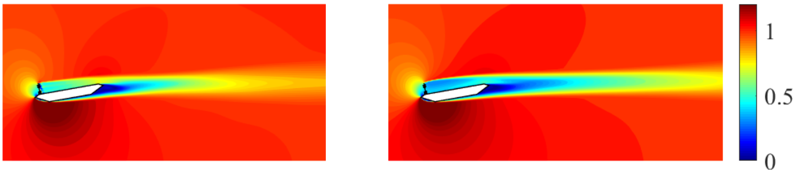

(a) *GB*, $\alpha = -10^\circ$

(b) *HB*, $\alpha = -10^\circ$

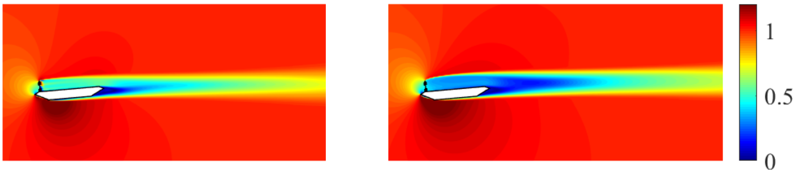

(c) *GB*, $\alpha = -5^\circ$

(d) *HB*, $\alpha = -5^\circ$

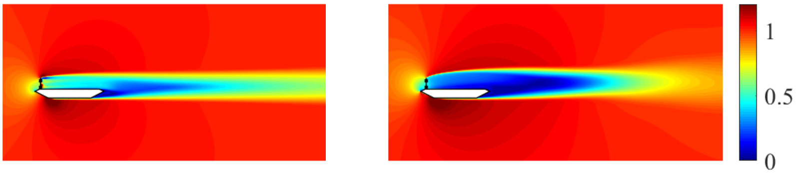

(e) *GB*, $\alpha = 0^\circ$

(f) *HB*, $\alpha = 0^\circ$

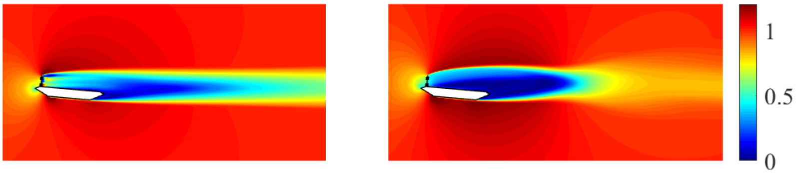

(g) *GB*, $\alpha = 5^\circ$

(h) *HB*, $\alpha = 5^\circ$

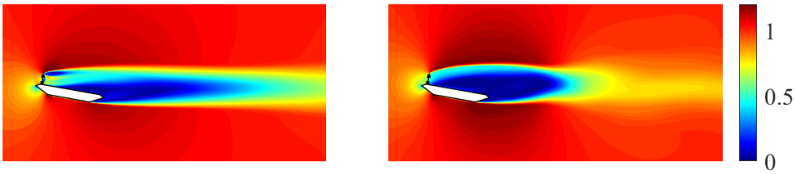

(i) *GB*, $\alpha = 10^\circ$

(j) *HB*, $\alpha = 10^\circ$

Figure 5.32: The time-averaged velocity fields, $\overline{U}/U_0$, of the *GBB WW* when different incidence angles are adopted.

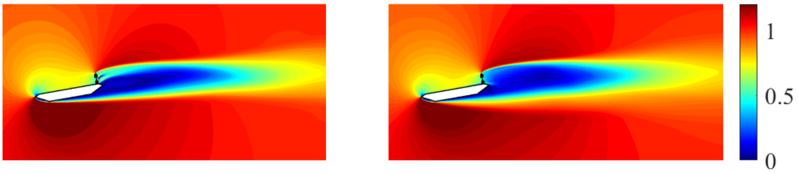

(a) *GB*, $\alpha = -10^\circ$ (b) *HB*, $\alpha = -10^\circ$

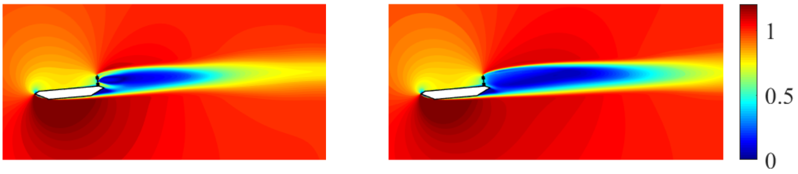

(c) *GB*, $\alpha = -5^\circ$ (d) *HB*, $\alpha = -5^\circ$

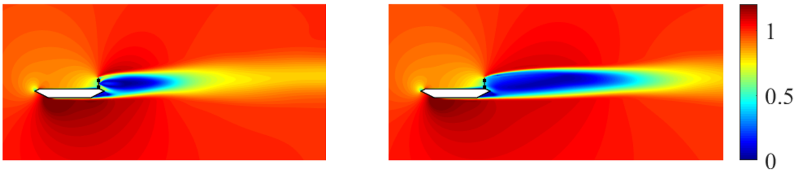

(e) *GB*, $\alpha = 0^\circ$ (f) *HB*, $\alpha = 0^\circ$

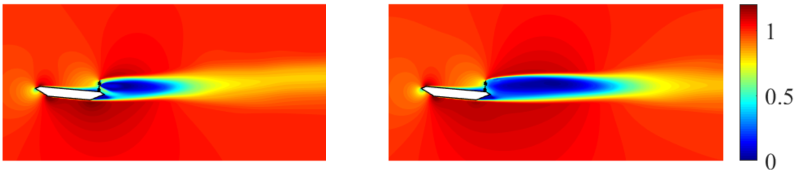

(g) *GB*, $\alpha = 5^\circ$ (h) *HB*, $\alpha = 5^\circ$

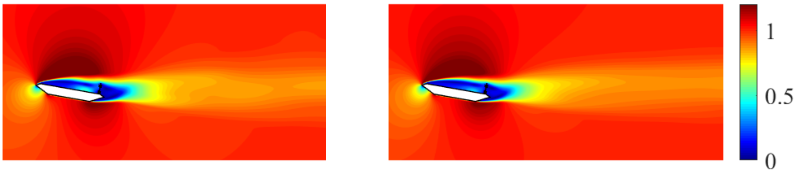

(i) *GB*, $\alpha = 10^\circ$ (j) *HB*, $\alpha = 10^\circ$

Figure 5.33: The time-averaged velocity fields, $\overline{U}/U_0$, of the *GBB LW* when different incidence angles are adopted.

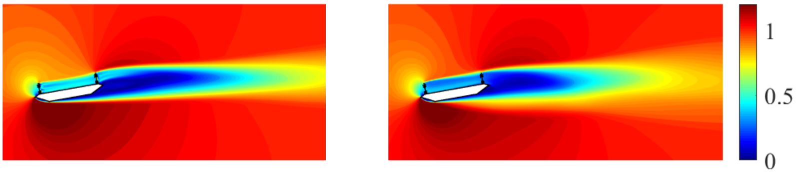

(a) *GB*, $\alpha = -10^\circ$ (b) *HB*, $\alpha = -10^\circ$

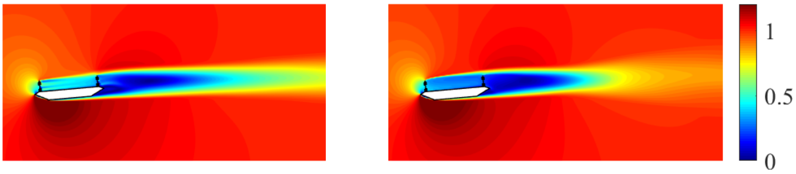

(c) *GB*, $\alpha = -5^\circ$ (d) *HB*, $\alpha = -5^\circ$

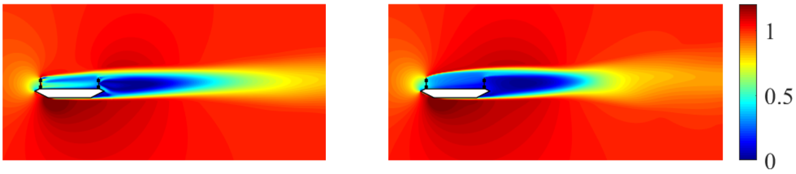

(e) *GB*, $\alpha = 0^\circ$ (f) *HB*, $\alpha = 0^\circ$

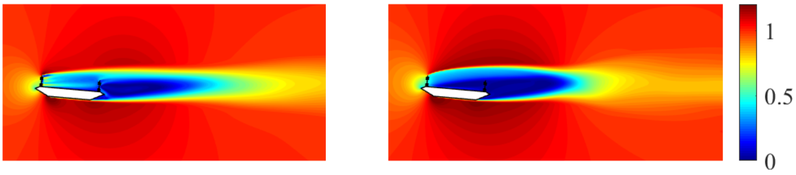

(g) *GB*, $\alpha = 5^\circ$ (h) *HB*, $\alpha = 5^\circ$

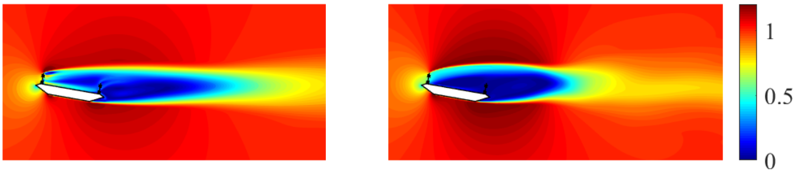

(i) *GB*, $\alpha = 10^\circ$ (j) *HB*, $\alpha = 10^\circ$

Figure 5.34: The time-averaged velocity fields, $\overline{U}/U_0$, of the *GBB DW* when different incidence angles are adopted.136

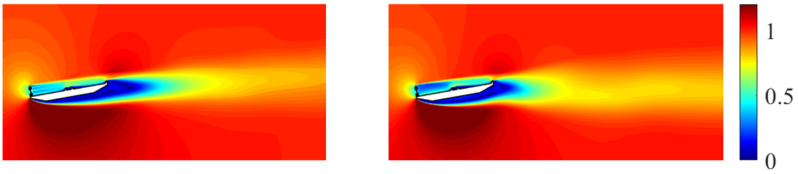

(a) *GB*, $\alpha = -10^\circ$

(b) *HB*, $\alpha = -10^\circ$

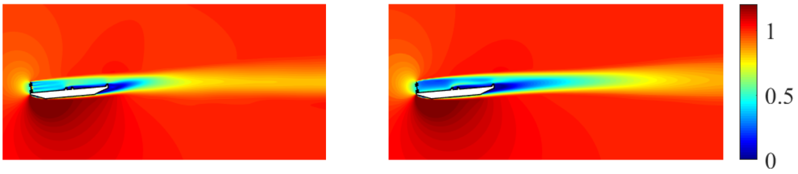

(c) *GB*, $\alpha = -5^\circ$

(d) *HB*, $\alpha = -5^\circ$

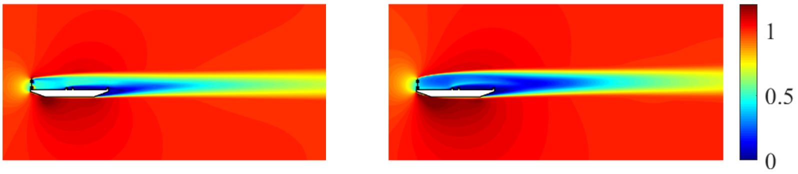

(e) *GB*, $\alpha = 0^\circ$

(f) *HB*, $\alpha = 0^\circ$

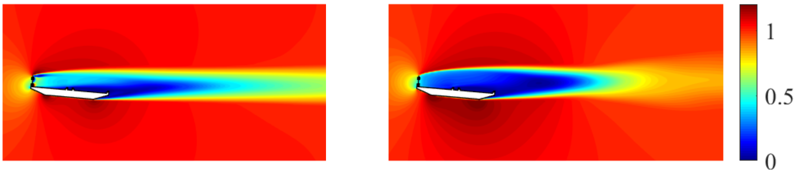

(g) *GB*, $\alpha = 5^\circ$

(h) *HB*, $\alpha = 5^\circ$

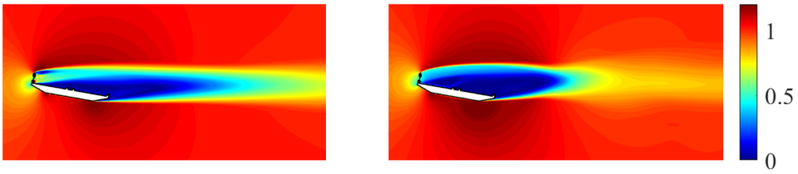

(i) *GB*, $\alpha = 10^\circ$

(j) *HB*, $\alpha = 10^\circ$

Figure 5.35: The time-averaged velocity fields, $\overline{U}/U_0$, of the *KPHB WW* when different incidence angles are adopted.137

5.6.6 The time-averaged streamlines of all cases

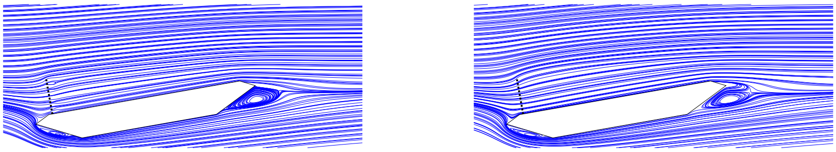

(a) *GB*, $\alpha = -10^\circ$ (b) *HB*, $\alpha = -10^\circ$

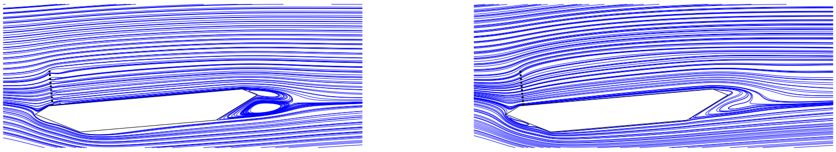

(c) *GB*, $\alpha = -5^\circ$ (d) *HB*, $\alpha = -5^\circ$

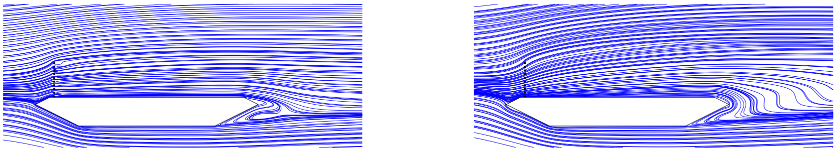

(e) *GB*, $\alpha = 0^\circ$ (f) *HB*, $\alpha = 0^\circ$

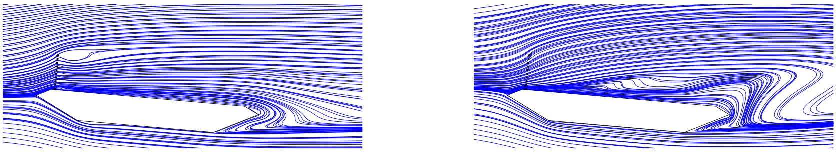

(g) *GB*, $\alpha = 5^\circ$ (h) *HB*, $\alpha = 5^\circ$

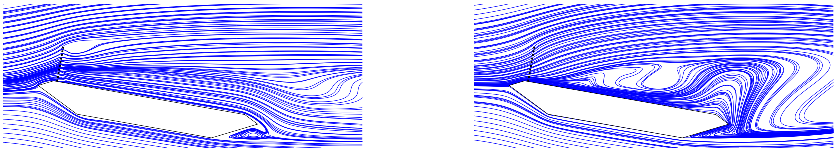

(i) *GB*, $\alpha = 10^\circ$ (j) *HB*, $\alpha = 10^\circ$

Figure 5.36: The time-averaged velocity streamlines of the *GBB WW* when different incidence angles are adopted.

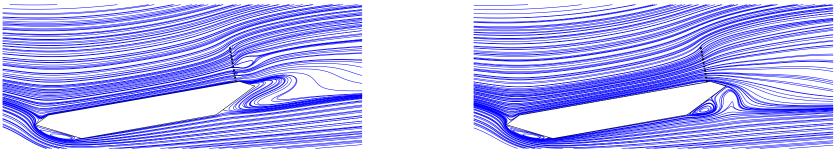

(a) *GB*, $\alpha = -10^\circ$ (b) *HB*, $\alpha = -10^\circ$

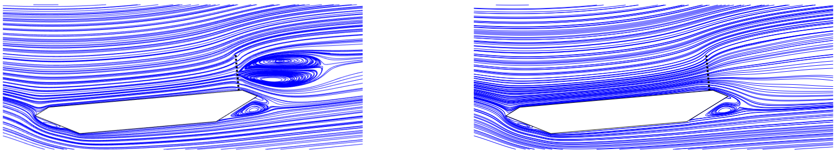

(c) *GB*, $\alpha = -5^\circ$ (d) *HB*, $\alpha = -5^\circ$

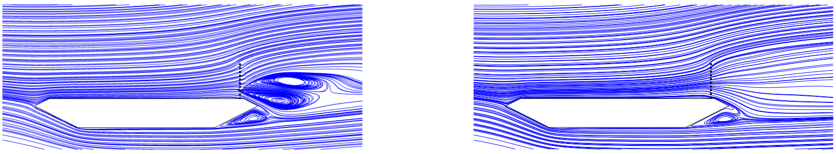

(e) *GB*, $\alpha = 0^\circ$ (f) *HB*, $\alpha = 0^\circ$

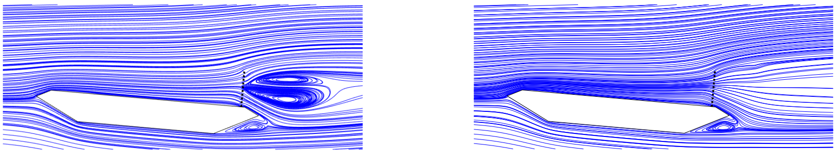

(g) *GB*, $\alpha = 5^\circ$ (h) *HB*, $\alpha = 5^\circ$

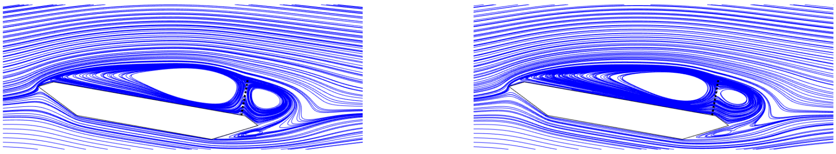

(i) *GB*, $\alpha = 10^\circ$ (j) *HB*, $\alpha = 10^\circ$

Figure 5.37: The time-averaged velocity streamlines of the *GBB LW* when different incidence angles are adopted.

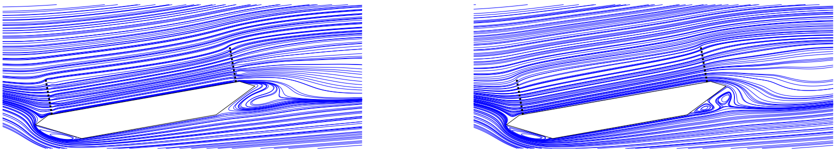

(a) *GB*, $\alpha = -10^{\circ}$ (b) *HB*, $\alpha = -10^{\circ}$

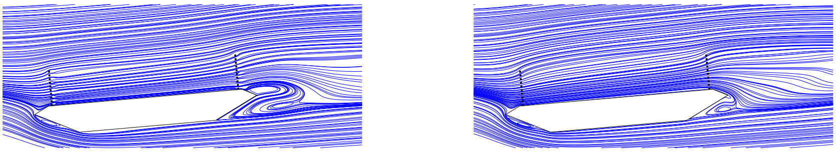

(c) *GB*, $\alpha = -5^{\circ}$ (d) *HB*, $\alpha = -5^{\circ}$

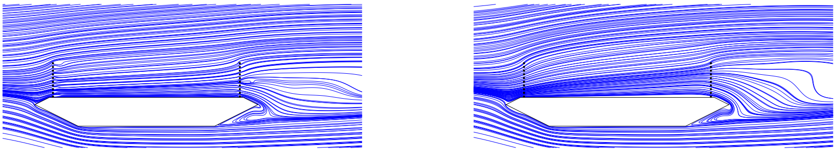

(e) *GB*, $\alpha = 0^{\circ}$ (f) *HB*, $\alpha = 0^{\circ}$

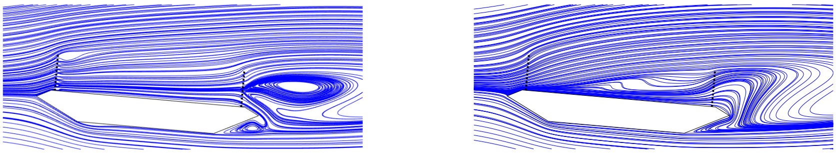

(g) *GB*, $\alpha = 5^{\circ}$ (h) *HB*, $\alpha = 5^{\circ}$

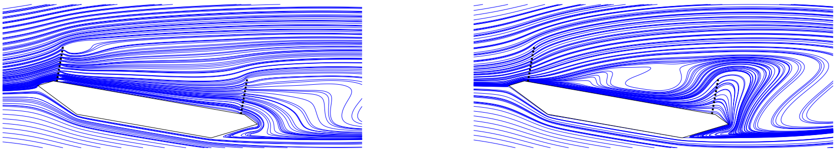

(i) *GB*, $\alpha = 10^{\circ}$ (j) *HB*, $\alpha = 10^{\circ}$

Figure 5.38: The time-averaged velocity streamlines of the *GBB DW* when different incidence angles are adopted.

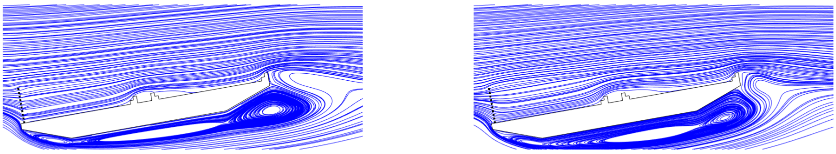

(a) *GB*, $\alpha = -10^\circ$ (b) *HB*, $\alpha = -10^\circ$

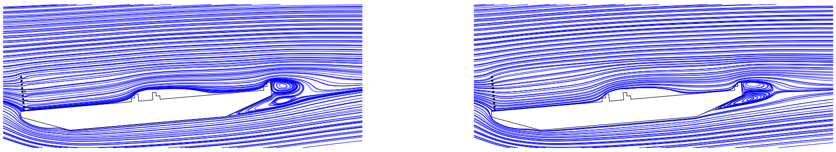

(c) *GB*, $\alpha = -5^\circ$ (d) *HB*, $\alpha = -5^\circ$

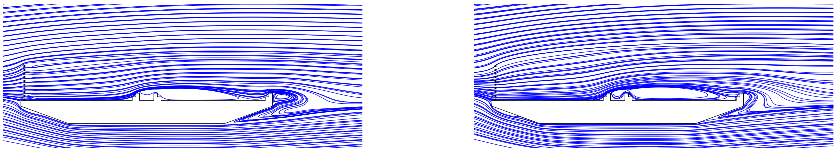

(e) *GB*, $\alpha = 0^\circ$ (f) *HB*, $\alpha = 0^\circ$

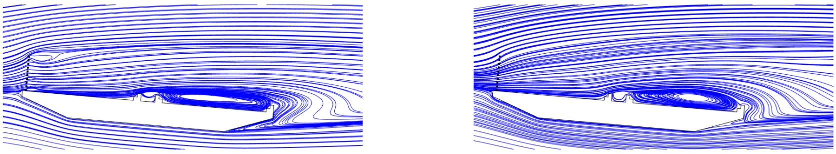

(g) *GB*, $\alpha = 5^\circ$ (h) *HB*, $\alpha = 5^\circ$

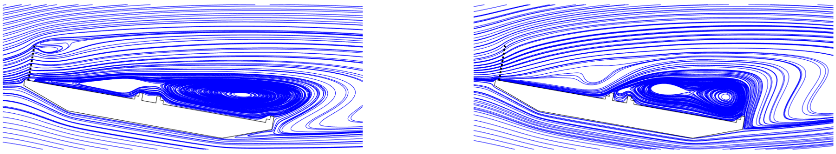

(i) *GB*, $\alpha = 10^\circ$ (j) *HB*, $\alpha = 10^\circ$

Figure 5.39: The time-averaged velocity streamlines of the *KPHB WW* when different incidence angles are adopted.

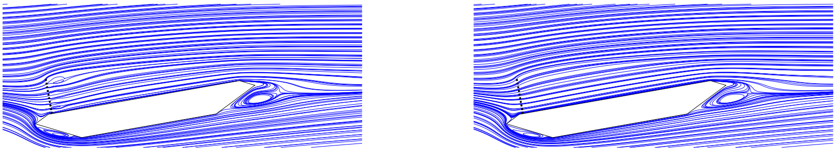

(a) *PB*, $\alpha = -10^\circ$ (b) *HB*, $\alpha = -10^\circ$

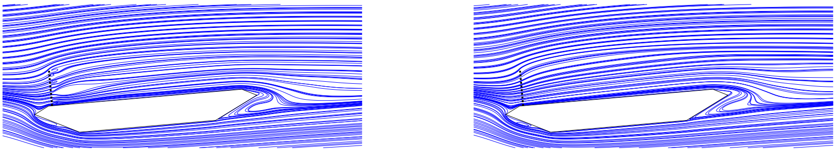

(c) *PB*, $\alpha = -5^\circ$ (d) *HB*, $\alpha = -5^\circ$

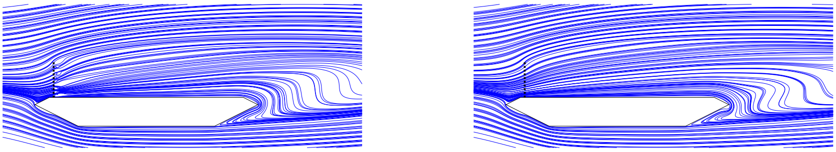

(e) *PB*, $\alpha = 0^\circ$ (f) *HB*, $\alpha = 0^\circ$

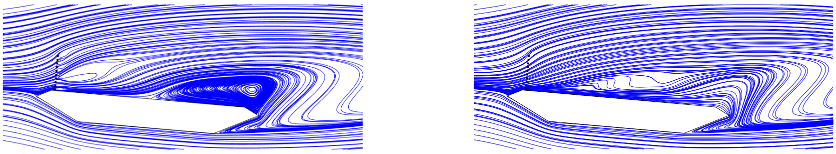

(g) *PB*, $\alpha = 5^\circ$ (h) *HB*, $\alpha = 5^\circ$

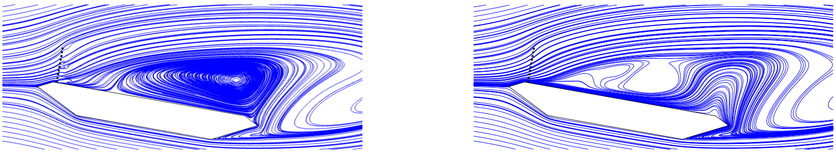

(i) *PB*, $\alpha = 10^\circ$ (j) *HB*, $\alpha = 10^\circ$

Figure 5.40: The time-averaged velocity streamlines of the *GBB WW* when the zero-thickness barrier is adopted.

Chapter 6

Large-eddy simulations and wind-tunnel experiments of a porous rectangular prism with solid roof

Following the previous investigations, this chapter compares the Large-Eddy Simulations (LES) and wind-tunnel experiments on a ground mounted porous rectangular prism, which is composed by porous side surfaces and solid roof. In particular, the porous surfaces are modeled by the aforementioned explicit modeling and pressure-jump approaches in LES. Moreover, both the smooth and turbulent inflow is considered by removing or using several roughness blocks.

6.1 Introduction

In the previous chapters it has been elucidated that differences can be generally expected between pressure-jump, *PJ*, based simulations and explicit models of the porous surface geometry, *EM*. Such differences were observed mainly comparing numerical results obtained following the aforementioned modeling strategies. Experimental results from the literature have been used in the case of bridge decks, but it was possible only to rely on global forces and some PIV measurement. Additionally, the previously considered cases where all characterized by rather simple geometries and smooth inflow conditions.

In this chapter, we proceed at comparing wind tunnel tests and numerical simulations on a ground mounted porous prism, which has appositely built and experimentally studied at Tamkang University, and which can be considered a prototype, although extremely simplified, of a body obtained by the assemblage of porous surfaces, exposed to both, smooth and turbulent wind. The considered model, which has an approximately cubic shape, has a solid roof and four exterior porous walls. The model has been conceived and build in order to allow the measurement of pressure on both sides of the composing surfaces, so allowing for a more detailed description of the obtained results with respect to the previously presented cases. This has been obtained by 3D printing the model and embedding the piping system within the wall thickness, in order to avoid to disturb the flow with the pressure taps piping system.

In particular, in Section 6.2, the setup of the wind-tunnel experiments is briefly introduced. Then, the proposed numerical simulations are described in Section 6.3. The presentation, comparison and analysis of the results are given in Section 6.4. Finally, conclusions are drawn in Section 6.5.

6.2 Experimental setup

The experiments are carried out in a conventional suction-type boundary layer wind tunnel at the Wind Engineering Research Center, Tamkang University. The section of this wind tunnel is $12.0\ m$ long, $2.2\ m$ wide and $1.8\ m$ high.

As already stated we here consider both smooth and turbulent inflow conditions. For the sake of simplicity, both such inflows have been chosen in order to be easily reproducible in the numerical simulations without recurring to synthetic flows. Consequently, fully developed atmospheric boundary layer conditions are not considered. In particular, in order to obtain an impinging smooth flow in ground mounted conditions, the model is placed on wooden planks placed at an height from the wind tunnel floor sufficient to avoid its boundary layer. To decrease as much as possible the turbulence impinging on the model, the windward edge of the planks have been sharpened and the planks painted to render them as smooth as possible. An overview of the model is shown in Fig. 6.1. Velocity measurements performed without posing the model on the planks confirmed that at the model location a flat profile is obtained characterized by a turbulence intensity of approximately 1%. Starting from such conditions, turbulence is introduced adding two rows of roughness blocks upstream the model. The velocity of inflow is set to be $10.0\ m/s$.

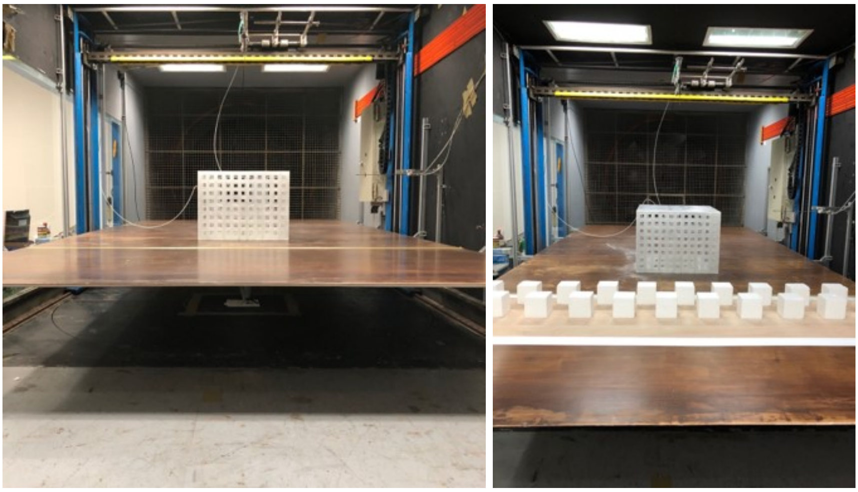

(a) (b)

Figure 6.1: The wind-tunnel experiments of porous prism immersed in (a): smooth inflow and (b) turbulent inflow.

The geometric details of the adopted porous body are shown in Fig. 6.2. The roof, *Surface E*, is fully solid, while the other surfaces, *Surface A - D*, are permeable. As shown in Fig. 6.2 (a), the length and height of each side surface are set to $D = 0.46\ m$ and $H = 0.345\ m$, respectively.

In order to clearly describe the arrangement of pores, a part of *Surface A* is shown in Fig. 6.2 (b), which corresponds to the dash rectangle zone of Fig. 6.2 (a). On each permeable surface, the square pores are evenly distributed: 11 in each line and 8 in each column. Both the length and distance of these pores equal to $d = \frac{1}{23}D$. The distance between pores and surface edges is also set as d. Consequently, the porosity, β, of each permeable surface equals to 22%. Moreover, the thickness, t, of each surface equals to $\frac{1}{115}D$, which is also the thickness of the side porous walls. With this setup, the thickness such that $t = 0.25d$.

The pressure probes are illustrated in Fig. 6.2 (a) as dots, which are equally distributed on both inside and outside of each surface. In such context, 16 probes are arranged on both side of each surface.

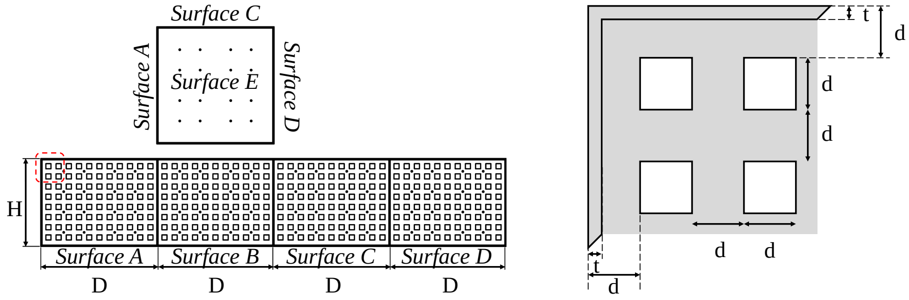

(a) (b)

Figure 6.2: The expanded view of (a): the adopted porous prism and (b): the top corner of *Surface A*. The squares and dots respectively represent the pores and pressure probes.

6.3 Numerical setup

In this section, the computational models and the numerical setup are firstly reported. Then, the wind profiles at the immersed body location obtained in the numerical simulations are compared to the experimental ones.

6.3.1 Computational model

The size of computational domain and model are shown in Fig. 6.3. No scaling of lengths is adopted, so that the sizes of the computational domain and roughness blocks are respectively set as $L = 12.0\ m$, $B = 2.2\ m$, $G = 1.8\ m$ and $b = 0.05\ m$.

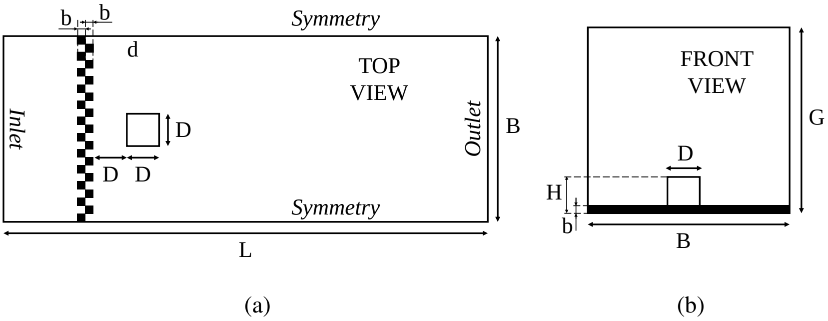

(a)

(b)

Figure 6.3: The computational domain and model (a): top view and (b) front view.

The mesh adopted for the *EM* cases is shown in Fig. 6.4. Close to the surfaces, the mesh size in each direction is set as $\delta_x/d = \delta_y/d = \delta_z/d = 0.25$. Consequently, the thickness and side length of each pore is respectively represented by 1 and 4 cells. This mesh resolution is also adopted for the roughness blocks. In such a way, the mesh counts approximately 6.5 M cells. The mesh adopted for the *PJ* cases is obtained in a similar way.

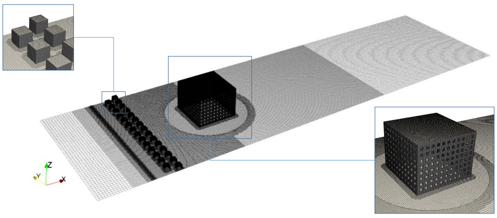

Figure 6.4: The mesh of the *EM* cases when using roughness blocks.

The pressure probes arranged in CFD are illustrated in Fig. 6.5 (a). For a clear description, the pressure taps in wind-tunnel experiment are also shown in Fig. 6.5 (b). Besides the setup used in experiments, more probes are adopted in simulations for detail measurement. Moreover, in both CFD and experiments, the pressure taps are ordered in four horizontal paths and four vertical paths, where two of them are shown in Fig. 6.5. The horizontal path located at the immersed body bottom, *H1*, is illustrated as black arrows on each surface, which starts at the junction of *Surface A* and *Surface D*. The paths are consequently named as *H2*, *H3* and *H4*. The vertical path, *V1*, is illustrated as blue arrows, and the other paths are consequently named as *V2*, *V3* and *V4*.

It should be noticed that the pressure probes are positioned right on the respective surfaces, while the gap mentioned in Chapter 3 is not adopted, for the sake of comparability with the experimental results of the *EM* model.

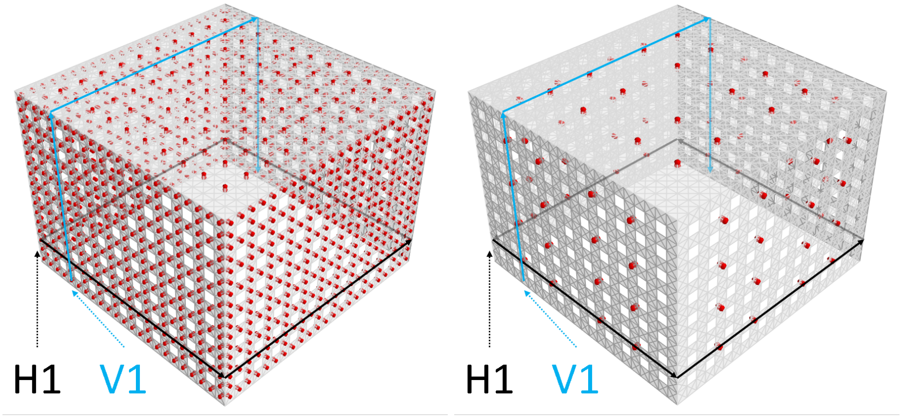

(a)

(b)

Figure 6.5: The arrangements of pressure probes for (a): CFD and (b): experiments. The horizontal path, *H1*, and vertical path, *V1*, on each surface are respectively illustrated as black and blue arrows.

Since the size of numerical domain is equal to that of the wind tunnel without scaling, the same inflow velocity, U_0, of the experiment is applied at the inlet boundary. The Reynolds number based on the immersed body length is $Re = \frac{\rho U_0 D}{\mu} = 3.7 \times 10^5$. A zero pressure is imposed at the outlet boundary, while a null pressure gradient is prescribed at the inlet. Symmetry boundary conditions are imposed at the top, bottom, front and back surfaces of the domain. The roughness blocks are defined as wall boundaries.

With respect to the porous prism, for *EM* cases, wall boundary is adopted for external and internal surfaces, while symmetry condition is used for pores, due to the low resolution there adopted. For *PJ* cases, the pressure jumps are calculated relying on the formula previously derived [120], which reads

$$\Delta p = \frac{\rho U_n^2}{2} \frac{(a_1 \beta + 2)(\beta - 1)}{\beta^2 (a_2 - 1)}, \tag{6.1}$$

where Δp is the pressure jump, ρ is the fluid density, U_n is the local velocity normal to the surface, β is the porosity defined by the pore area divided by the total surface area, $a_1 = 0.5$ and $a_2 = -0.1$. Moreover, it should be noticed that the solid roof (*Surface E*) is explicitly modeled in both *EM* and *PJ* cases and set as wall boundary.

A centered second-order differentiation scheme is adopted for the diffusive terms, while a centered-upwind blended differencing scheme (LUST) is adopted for the advective terms to preserve boundedness with reasonable accuracy. Time integration is performed by using the Crank-Nicolson scheme. The coupling of pressure and velocity is obtained for all simulations by using the well known Pressure-Implicit with Splitting of Operators (PISO) algorithm. The one-Equation model is considered, where the wall treatment is performed with van Driest damping law.

The open source Finite Volume software OpenFOAM is adopted to perform the simulations.

6.3.2 Inflow profiles

Before proceeding, the profiles measured in the numerical simulations at the building location for the time-averaged velocity, $\overline{U}$, turbulence intensity, $I_i, i = u, v, w$, and integral time scale, T, are compared to those observed in experiments. As shown in Fig. 6.6 some differences between the wind profiles measured in the experiments and numerical simulations can be observed, but overall a reasonable agreement is found up to the roof hight, $z/H = 1$.

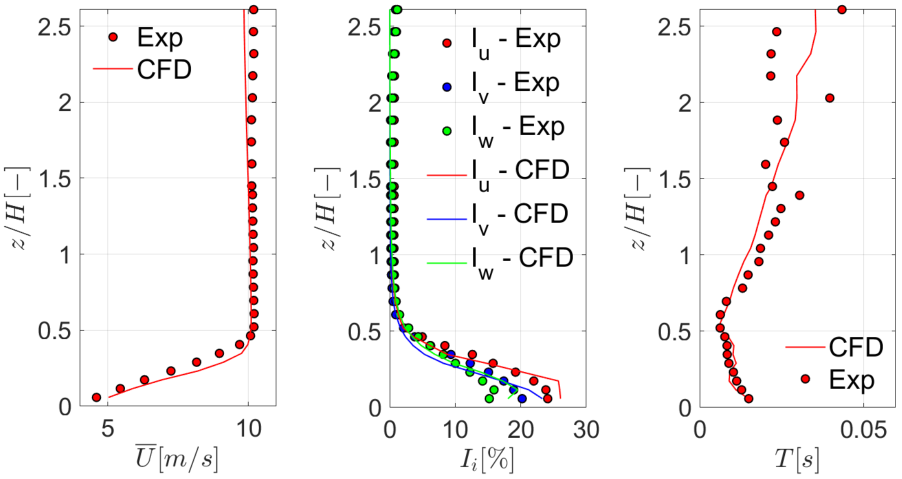

(a) (b) (c)

Figure 6.6: The profiles at the immersed body location of (a): time-averaged velocity, $\overline{U}$, (b): turbulence intensity, I_i, and (c): integral time scale, T for the numerical simulations and wind tunnel experiments.

6.4 Results

In this section, we analyze the results obtained by using *EM*, *PJ* and wind-tunnel experiments. Firstly, the flow patterns obtained by using *EM* and *PJ* approaches are qualitatively compared. Then, quantitative comparisons between experiments and CFD are provided.

6.4.1 Flow patterns

The contours of Q for the porous prism are shown in Fig. 6.7, which are colored by the instantaneous velocity magnitude. In smooth inflow conditions, for both *EM* and *PJ* cases, in the very first part of the shear layer, the flow appears to be laminar for all cases. Downstream to this laminar zone, the shear layer grows and breaks down to turbulence.

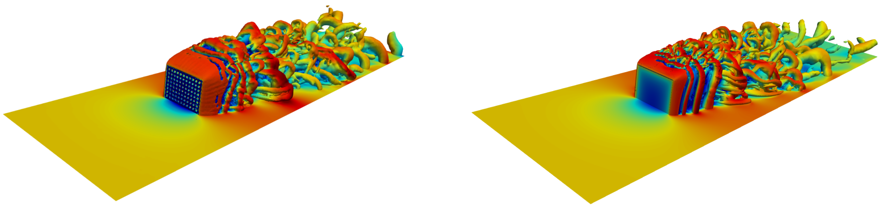

(a) *EM*, Smooth inflow (b) *PJ*, Smooth inflow

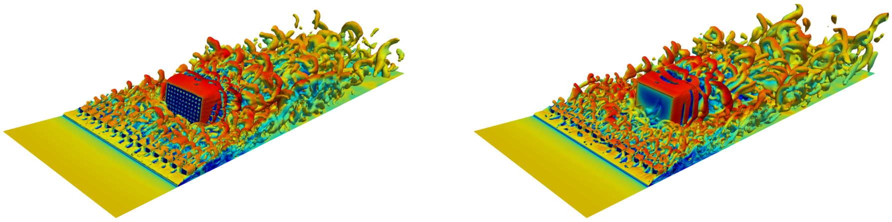

(c) *EM*, Turbulent inflow (d) *PJ*, Turbulent inflow

Figure 6.7: The contours of computed Q, which are colored by the instantaneous velocity.

Then, the fields of instantaneous velocity magnitude, made non-dimensional with the reference inflow velocity, U/U_0, at XY slice are shown in Fig. 6.8. Several differences of internal flow can be found between *EM* and *PJ* cases, which are probably mainly caused by the pores distribution on *Surface A*. Considering that the influence of each pore cannot be reproduced by using pressure jumps, the bleed flows inside *PJ* cases are not observed. Such differences appear to be less noticeable when the body is immersed in a turbulent flow. Comparable patterns can be also found in the wake flow downstream of the *Surface C*.

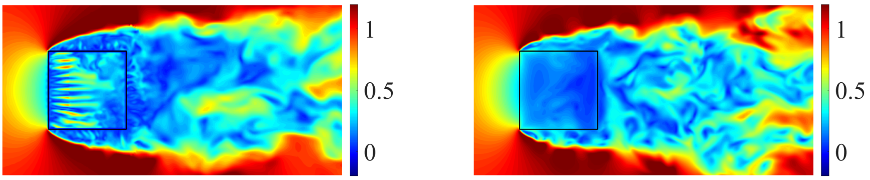

(a) *EM*, Smooth inflow

(b) *PJ*, Smooth inflow

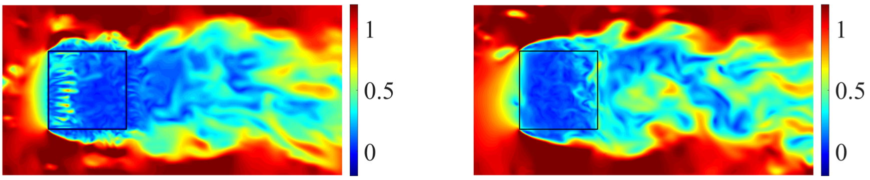

(c) *EM*, Turbulent inflow

(d) *PJ*, Turbulent inflow

Figure 6.8: The distributions of instantaneous velocity, U/U_0, for *EM* and *PJ* cases at the XY slice with $z = 0.5H$.

Similarly to Fig. 6.8 (which reports the instantaneous non-dimensional velocity magnitude distribution) the time-averaged non-dimensional velocity magnitude distribution is shown in Fig. 6.9. For both *EM* and *PJ* cases, comparable overall flow patterns are predicted, being for instance, the shape of the wake zone comparable in *EM* and *PJ* models. We also notice that the wake zone shortens in turbulent inflow conditions with respect to smooth inflow conditions in a comparable why when using the two approaches. Despite such similarities, we clearly observe, coherently with observations in the previous chapters, that the bleed flow through the pores creates structures which extend far downstream the porous surfaces. In such zones, high and low velocity areas corresponding to the pores and the solid parts of the barriers, alternate, and their mixing, due to momentum conservation, leads to a pressure recovery as already discussed in previous chapters. Such structures are to be considered of vanishing dimensions for the *PJ* models, which appears as a crude approximation in the present case. Using turbulent inflow conditions seems to reduce such affect which, nevertheless can be clearly observed in all cases.

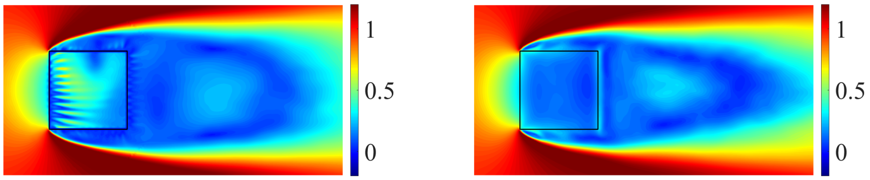

(a) *EM*, Smooth inflow (b) *PJ*, Smooth inflow

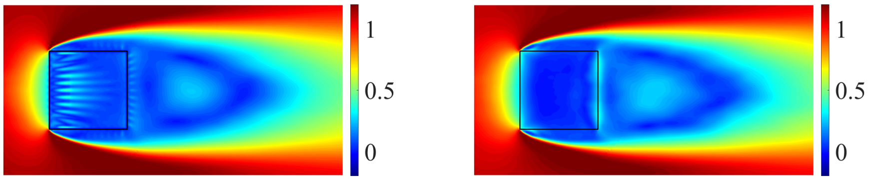

(c) *EM*, Turbulent inflow (d) *PJ*, Turbulent inflow

Figure 6.9: The distributions of time-averaged velocity, $\overline{U}/U_0$, for *EM* and *PJ* cases at the XY slice with $z = 0.5H$.

The aforementioned results can be clearly seen also in Fig. 6.10, which reports non-dimensional time averaged relative velocity magnitude an a XZ plane.

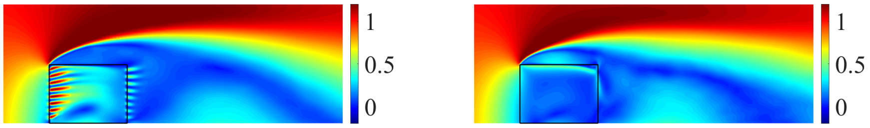

(a) *EM*, Smooth inflow (b) *PJ*, Smooth inflow

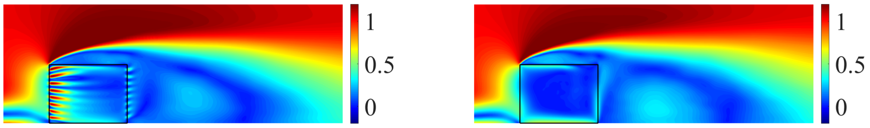

(c) *EM*, Turbulent inflow (d) *PJ*, Turbulent inflow

Figure 6.10: The distributions of time-averaged velocity, $\overline{U}/U_0$, for *EM* and *PJ* cases at the XZ slice with $y = 0$.

Finally, the time-averaged streamlines for *EM* and *PJ* cases are shown in Fig. 6.11. Although the internal flow patterns in *EM* and *PJ* cases are still different, the location and size of the main vortex in wake flow are well reproduced by *PJ*. Similarly to the bleed flows through the windward *Surface A*, these differences caused by solid corners are also less noticeable when the body is immersed in turbulent flow.

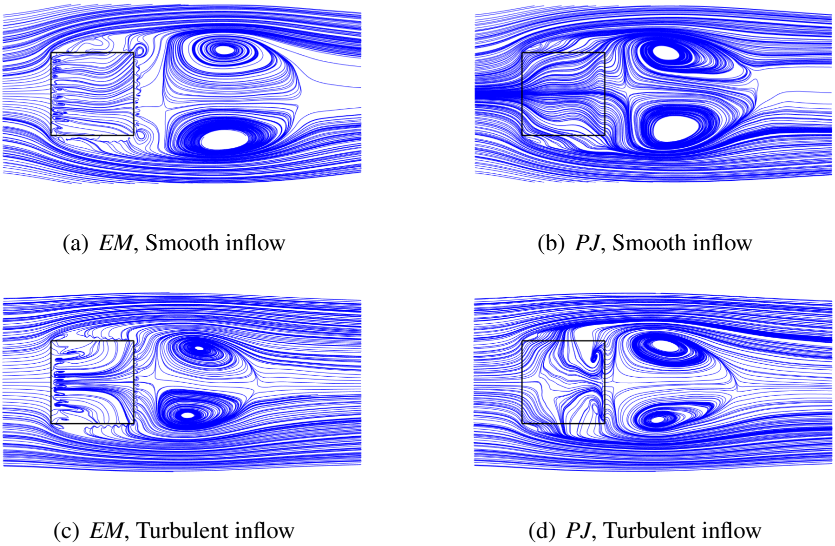
(a) *EM*, Smooth inflow

(b) *PJ*, Smooth inflow

(c) *EM*, Turbulent inflow

(d) *PJ*, Turbulent inflow

Figure 6.11: The time-averaged streamlines for *EM* and *PJ* cases at the XY slice with $z = 0.5H$.

6.4.2 Pressure coefficient

Figures 6.12 and 6.13 illustrate the time-averaged pressure distribution along the previously mentioned paths, inside and outside. Overall, reasonable agreement can be found at the windward surface, but deviations are apparent on other cases for both *EM* and *PJ*. In some circumstances, like at the inside path in correspondence of the $SurfaceA$, the *EM* model is clearly closer to measurements due to known difficulties, i.e. the presence of the aforementioned pressure reconvert zones, which in the previous cases led to the offsetting of the probing paths form the surfaces. Nevertheless, in other cases, differences appear to be more difficult to be explained and directly linked to the shortcomings of the modeling approaches.

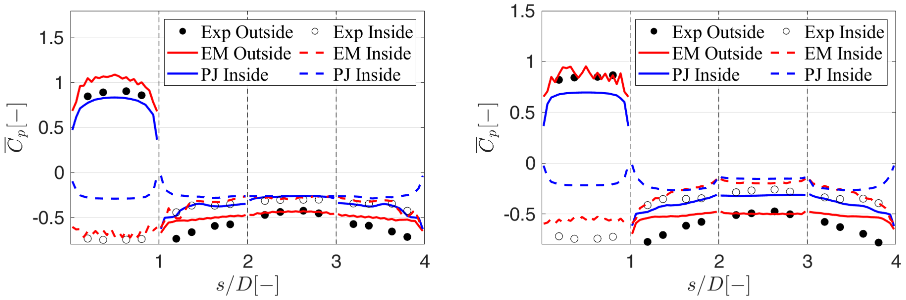

(a) *H1* (b) *H4*

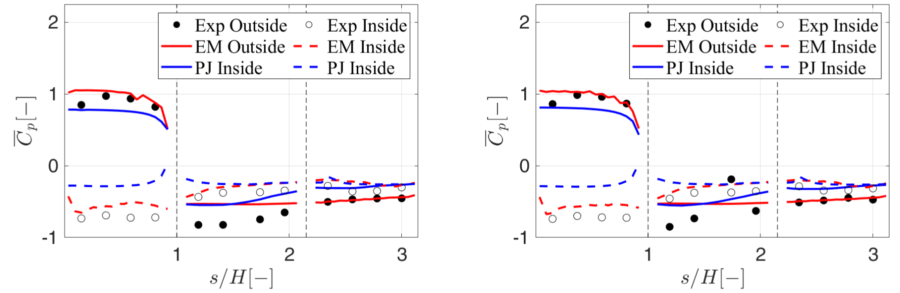

(c) *V1* (d) *V4*

Figure 6.12: The $\overline{C}_p$ along horizontal and vertical paths in smooth inflow conditions.

With reference to Fig. 6.13, some ameliorants can be seen when considering turbulent inflow conditions, but overall previously obtained results are mainly confirmed. Further results are reported in the Appendix for the sake of readability.

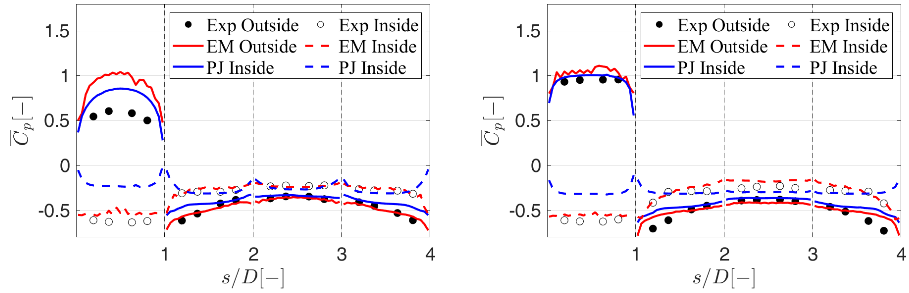

(a) *H1* (b) *H4*

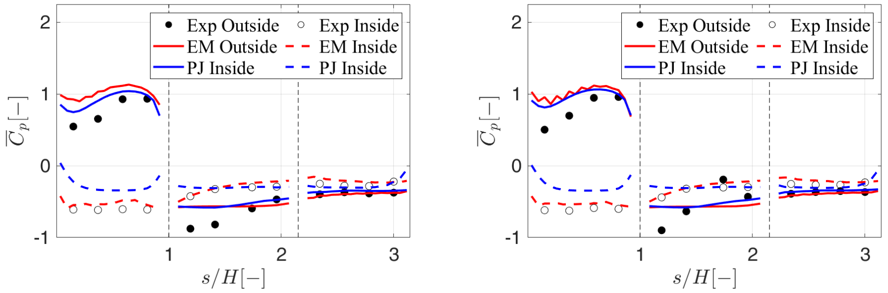

(c) *V1* (d) *V4*

Figure 6.13: The $\overline{C}_p$ along horizontal and vertical paths in turbulent inflow conditions.

The computed results of $\overline{C}_p$ against the experimental ones are reported in Fig. 6.14, where the overestimation of numerical results are usually found. Further results, for the sake of readability, are reported in the Appendix.

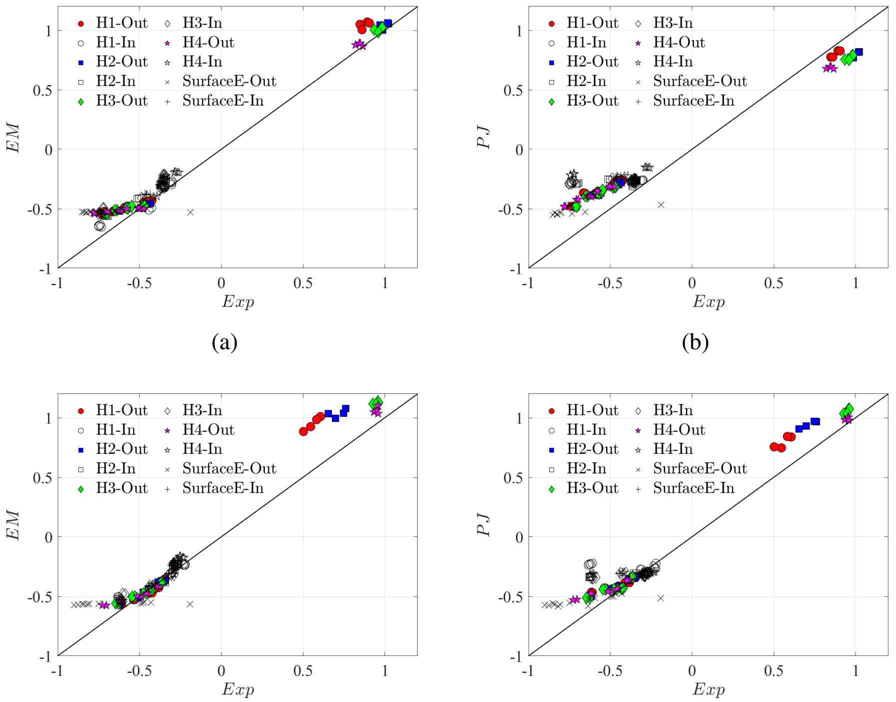

(a) (b)

(c) (d)

Figure 6.14: The correlations of $\overline{C}_p$ measured in the cases with (a) and (b): smooth inflow, (c) and (d): turbulent inflow.

Figure 6.15 reports the distribution of the C_p standard deviation, C_p', for all considered cases and models. In numerous circumstances, as expected, the *EM* model seem to provide a better accuracy with respect to the *PJ* model, which often shows very low values. At least partially, this can be attributed to the unsteadiness of the flow passing through the pores, which is not expected to be simulated for *PJ* models.

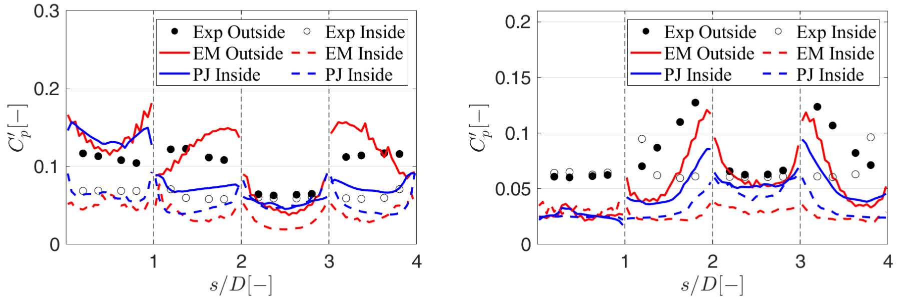

(a) *H1* (b) *H4*

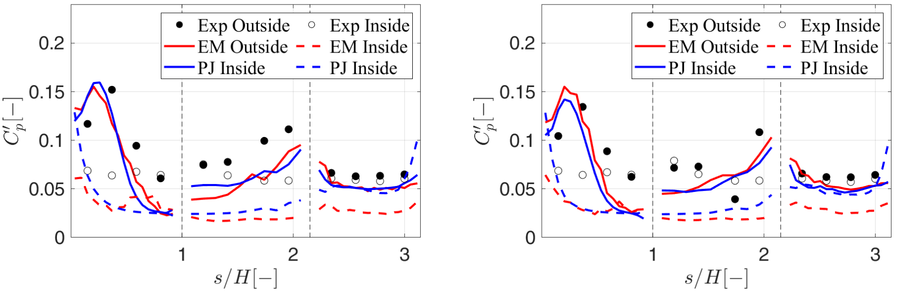

(c) *V1* (d) *V4*

Figure 6.15: The C_p' along horizontal paths for turbulent inflow conditions.

An overview of the obtained results is presented in the scatter plot reported in Fig. 6.16, where the underestimation of numerical results are observed. Further results, for the sake of readability, are also reported in the Appendix.

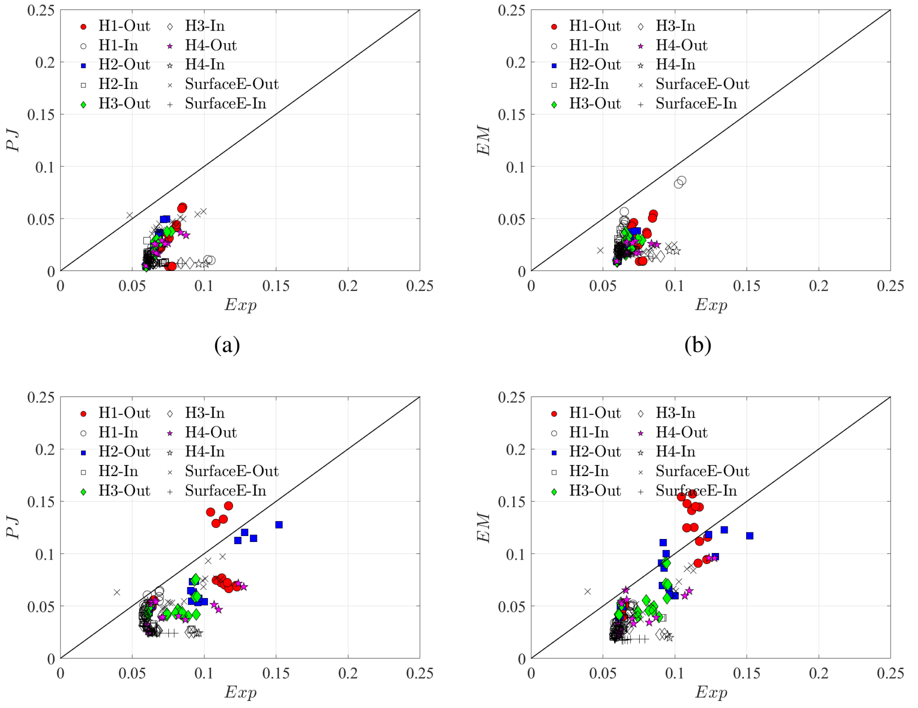

(a) (b)

(c) (d)

Figure 6.16: The correlations of C_p' measured in the cases with (a) and (b): smooth inflow, (c) and (d): turbulent inflow.

6.5 Conclusions

Following the previous investigations, this study evaluates the performance of using pressure-jump approach by investigating the flow around permeable ground mounted prism using LES. In particular, both smooth and turbulent inflow conditions are considered.

Results show that the external flow patterns between *PJ* and *EM* results are qualitatively comparable. In particular, the main time-averaged flow structures are well reproduced. Nevertheless, several differences are inevitably noticed, especially in the volume enclosed by the porous surfaces.

It appears that a slight improvement is obtained when considering turbulent inflow conditions with respect to smooth ones. This can be due to the lower sensitivity of the numerical model to the relatively coarse concretization inevitably adopted within the pores. Nevertheless, it can be conjectured that the presence of incoming turbulence favor the momentum mixing in the proximity of the barrier, shortening the downwind extent of pressure recovery zones. This would alleviate one of the inevitable differences which distinguish *EM* models form *PJ* ones.

It is finally important to notice that, the geometry of the considered case was chosen in order to allow for the building of *EM*. The hole size is here approximately one order of magnitude smaller than the overall immersed body size. After the experience gained in this research work, it is possible to conclude that, under such conditions pores can hardly by defined as vanishing in size, so that part of the problems can be probably attributed to an insufficient separation of scales. Evidently, increasing the scale separation and, so, obtaining pores which can be considered of vanishing thickness, poses very strong difficulties for both wind tunnel experiments and numerical simulations. In general, a decrease of accuracy of numerical simulations can be expected when considering porous surfaces in numerical simulations in comparison to fully solid bodies. Staying at the results considered in the present work the agreement between experimental results, explicit geometrical models and pressure jump shall be generally expected to be mainly qualitative.

6.6 Appendix

6.6.1 The $\overline{C}_p$ along all paths

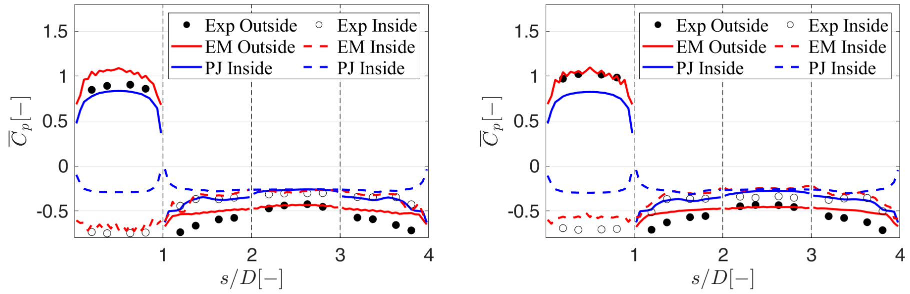

(a) *H1* (b) *H2*

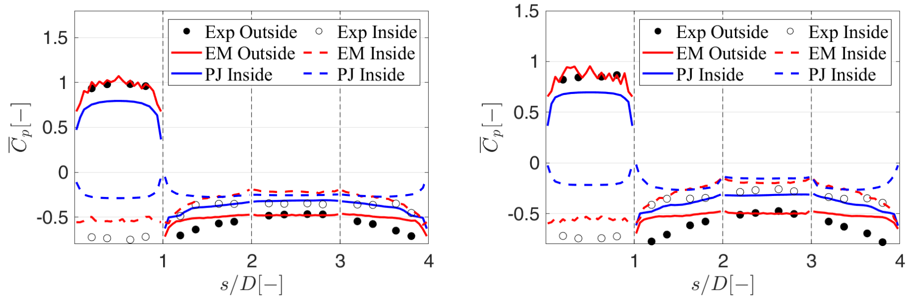

(c) *H3* (d) *H4*

Figure 6.17: The $\overline{C}_p$ along horizontal paths in smooth inflow conditions.

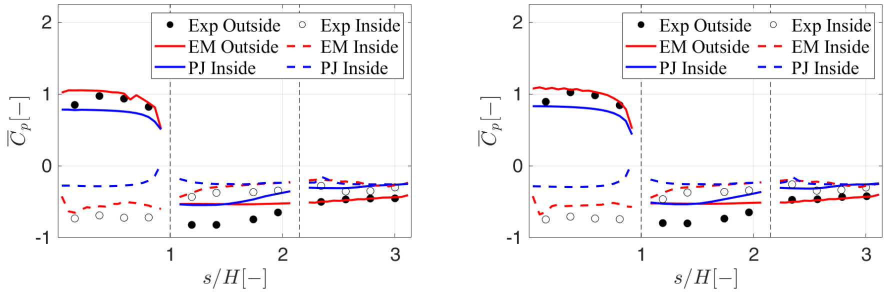

(a) *V1* (b) *V2*

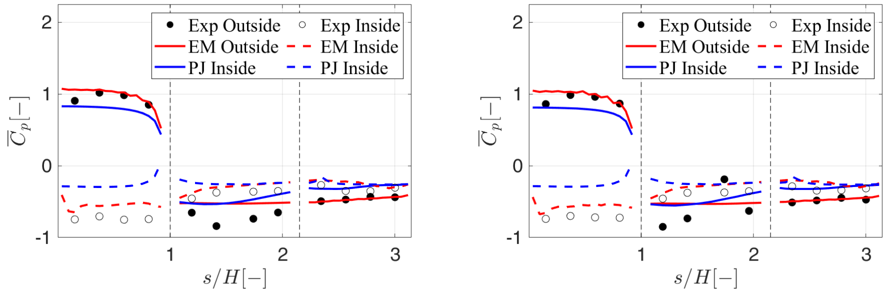

(c) *V3* (d) *V4*

Figure 6.18: The $\overline{C}_p$ along vertical paths in smooth inflow conditions.

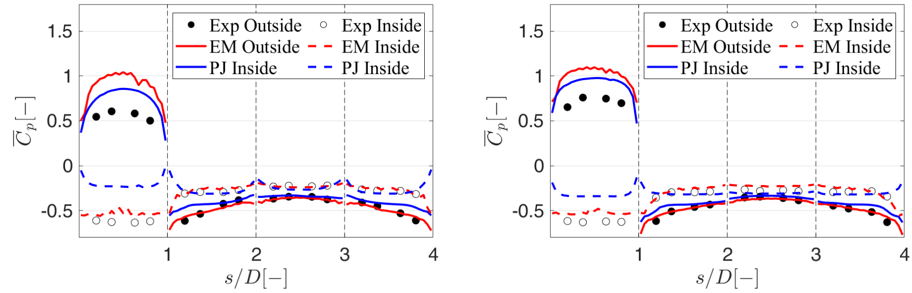

(a) *H1* (b) *H2*

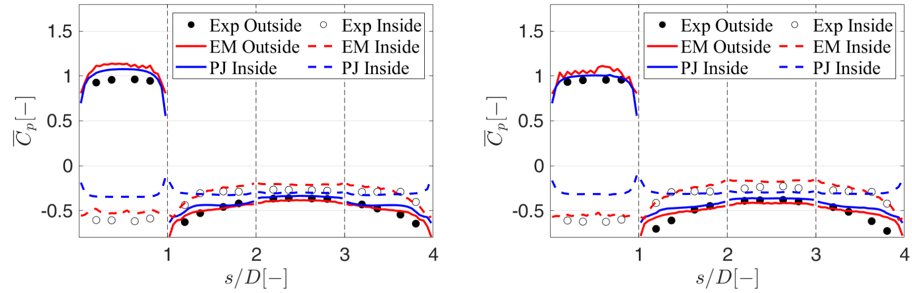

(c) *H3* (d) *H4*

Figure 6.19: The $\overline{C}_p$ along horizontal paths in turbulent inflow conditions.

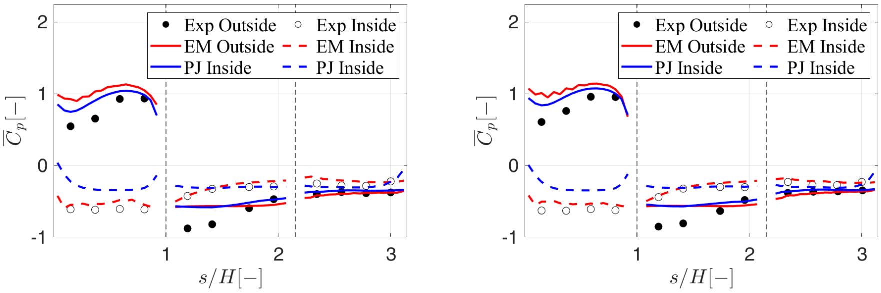

(a) *V1* (b) *V2*

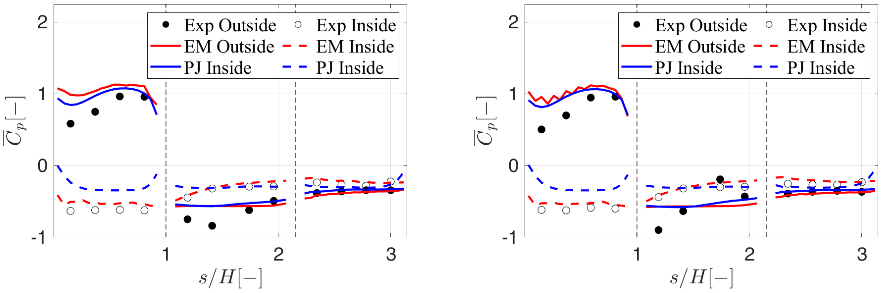

(c) *V3* (d) *V4*

Figure 6.20: The $\overline{C}_p$ along vertical paths in turbulent inflow conditions.

6.6.2 The C_p' along all paths

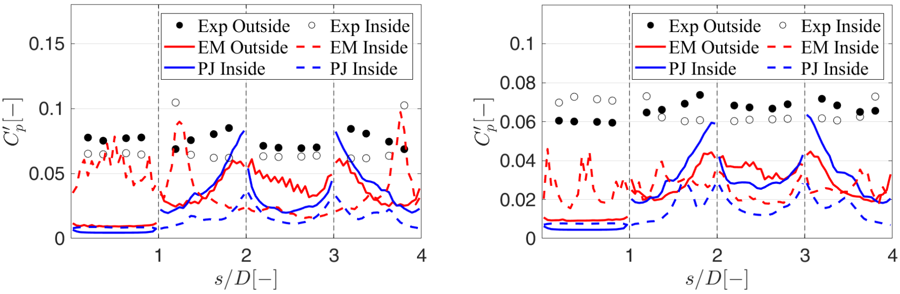

(a) *H1* (b) *H2*

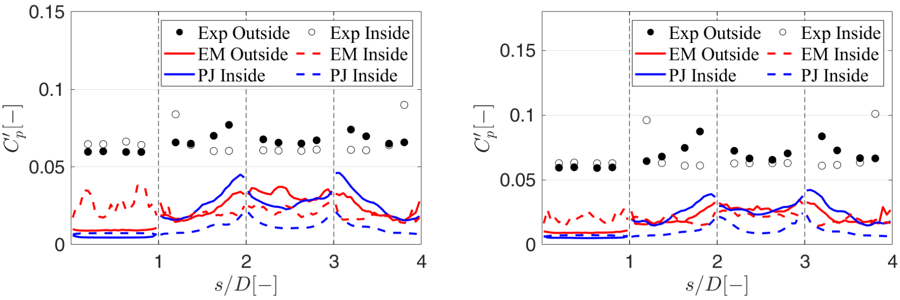

(c) *H3* (d) *H4*

Figure 6.21: The C_p' along horizontal paths in smooth inflow conditions.

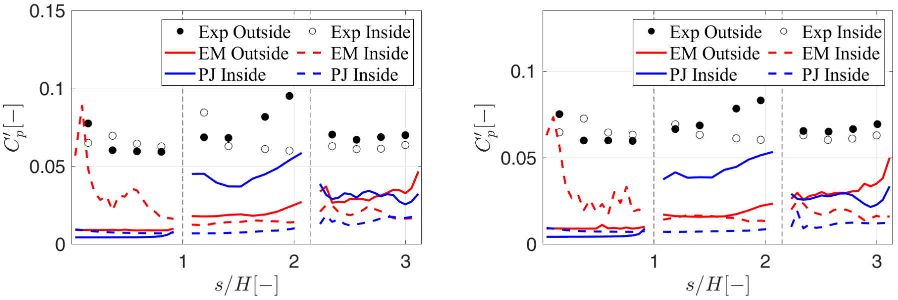

(a) *V1* (b) *V2*

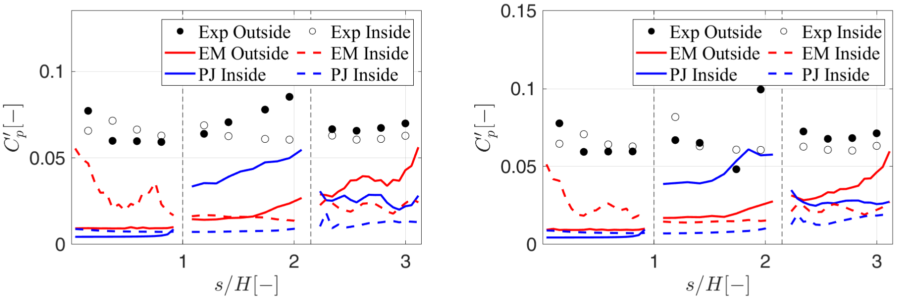

(c) *V3* (d) *V4*

Figure 6.22: The C'_p along vertical paths in smooth inflow conditions.

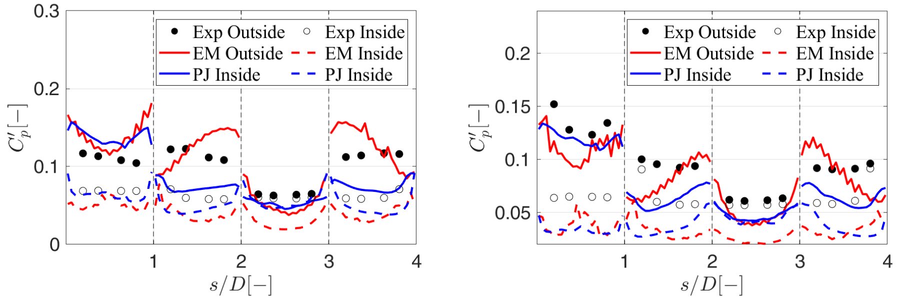

(a) *H1* (b) *H2*

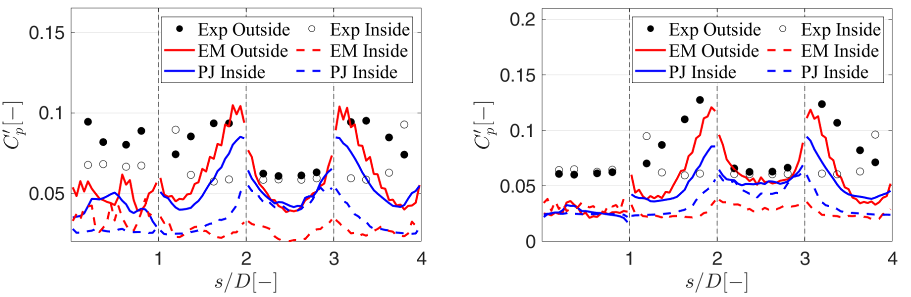

(c) *H3* (d) *H4*

Figure 6.23: The C'_p along horizontal paths in turbulent inflow conditions.

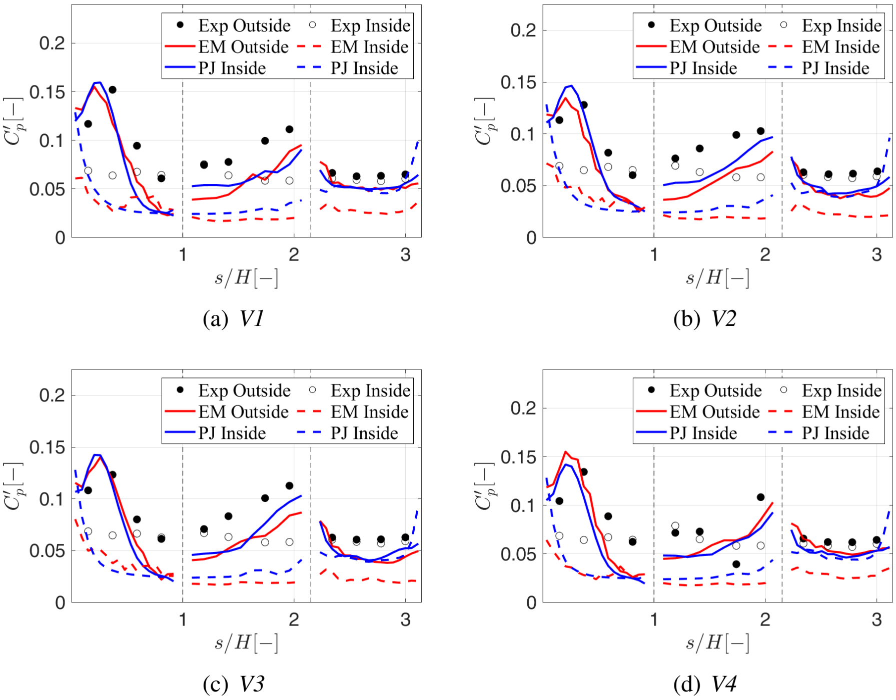

(a) *V1*

(b) *V2*

(c) *V3*

(d) *V4*

Figure 6.24: The C_p' along vertical paths in turbulent inflow conditions.

Chapter 7

Conclusions

In this thesis, the aerodynamic behavior of porous elements has been investigated, with particular emphasis on the use of pressure-jump, *PJ*, based models for their numerical simulations. The obtained results have been compared to the ones of non-homogenized models, where the porous elements are simulated in detail, i.e. the geometry of each pore is explicitly modeled, *EM*. In essence, *PJ*-based simulations represent homogenized models which allow to conveniently tackle the remarkable separation in scales existing between the macroscopic flow established around the structure and the microscopic-scale flow established within the pores. The main findings are summarized in the following.

In Chapter 2, a new model able to predict the pressure-jump based on surface porosity was proposed. The model, compared to previously available ones, provides a more physically grounded and detailed description of the elements which contribute to determine the pressure jump between the two sides of a porous surface. For instance, it allows to clarify the relations existing between local and homogenized quantities and clearly distinguishes the role played by pressure recovery zones found downstream the porous barrier. The model has been tested considering a simple thin porous barrier in confined flow conditions, showing good agreement with simulated *EM* and experimental results for all considered porosities (16% to 69%). The dependency of the pressure jump on the attack angle has been also considered, observing that simple formulations already present in the literature provided very good match with *EM* numerical models.

Based on such results, the pressure-jump approach was adopted to investigate the flow through a forward facing step, composed by a porous plate normal to the inflow and a solid plate parallel to the inflow. For such a simple case, reasonably good agreements between the *PJ* and the *EM* models were obtained, especially for the time-averaged results. Notably, flow details such as the pressure recovery downstream the porous barrier cannot be reproduced using *PJ* models. Such aspect, although being expected, requires to be carefully considered when comparing the aforementioned detailed models (in which the flow through the pores is simulated) to homogenized ones. Considering the flow unsteady behavior, we obtained a trend consistent with expectations: the agreement between *PJ* and *EM* becomes more satisfying when adopting a larger number of pores. Differences appear to be concentrated in the proximity of the porous barriers, as expected, but they do not appear to be there limited. Overall, it appeared extremely hard to clearly assess a form of the *PJ* results to *EM* as the pore size decreased. Rather, a qualitative similarity between the two model predictions was found.

In Chapter 3, a shape classically taken as a benchmark in the field of bluff-body aerodynamics has been considered: the 5:1 rectangular cylinder. Differently from other contributions found in the literature, here the immersed body was considered to be composed of porous surfaces, to radically affect its aerodynamic behavior. In this case, three main factor were considered: the surface porosity, the attack angle and the adopted turbulence model. The case is investigated relying on 2D-URANS. Results showed that global forces were in reasonable quantitative agreement for all the considered cases. Despite some sensitivity to the adopted turbulence model, differences appeared to be mainly related to local effects, which, once amplified downstream, might affect the global flow arrangement. In this case, the effects of the corners were also investigated and the possibility to adopt mixed *PJ*/*EM* models was considered.

In Chapter 4, the porous 5:1 rectangular cylinder was again considered with further comparisons between 2D-URANS and 3D-LES simulations. Again the agreement between the two simulations strategies depends on numerous factors, especially the details of pore arrangement when their number of holes is not extremely high. Indeed, such high number of pore shall not only make sure that pores are small compared to the overall immersed body size, but it is also required that the structures created downstream the pores are effectively small. Numerical simulations seem to indicate that this second requirement might be tighter than the first one, so rendering the theoretical limit of vanishing pore size extremely difficult to be reached. In fact, the local results obtained using *PJ*-based simulations should be always carefully considered, while the global drag coefficients appear to be in good agreement between the two models, at least in the limits of the proposed porosities (25% to 75%) and attack angles (0° to 9°).

In Chapter 5, the presence of porous barriers positioned as secondary structures on a bridge deck was analyzed using *PJ* and *EM* models and compared with available experimental results. Again, numerical models were able to correctly reproduce the trends observed in experimental data when considering different barrier positions and angles of attack. Differences between the two modeling approaches remained but, overall, *PJ* results were found to be adequate for computationally intense tasks such as the deck shape and wind shield optimization, for which the use of *PJ* models would lead to remarkable advantages due to their reduced computational cost and the possibility to vary the barrier height and porosity without re-meshing. This is also justified by the fact that the difference between the two numerical models were small if compared to those with experimental data in some cases. It was also shown that, in case of real barriers of non-vanishing thickness, one important aspect which might need consideration if the deflection operated by the barrier by means of shearing stresses (stresses exchanged in the barrier plane), which cannot be considered using standard *PJ* approaches.

Finally, in Chapter 6, a ground mounted parallelepiped with porous side walls and solid flat roof is considered using different inflow conditions, including atmospheric boundary layer flows. In this case a set of wind-tunnel experiments has been performed, showing great challenges also from the experimental point of view due to the presence of the pores. The case, although simplified, might be useful in order to open the way to the numerical simulation of porous cladding, often used in the construction of double skin facades. The experimental tests have been reproduced by LES, showing again that a qualitative agreement between *PJ* and *EM* models can be obtained, but that an accurate reproduction of the flow appears to be difficult with both modeling strategies.

Summarizing, the presented work investigated the aerodynamics of porous elements using *PJ* and *EM* approaches, together with the aim of evaluating the performance of *PJ* models. Results indicate that the two modeling strategies are usually found to be in good agreement, although a proper convergence of *EM* to *PJ* for vanishing pore size could not be observed. The comparison with the few available experimental data indicated several deviations of both *PJ* and *EM* models from the recorded data, but overall trends appear to be respected. It can be thus concluded that attention shall be paid in both *PJ* and *EM* as the presence of porous elements generally tend to decrease the accuracy of numerical simulations with respects to results obtained for solid bodies. Nevertheless, the use of *PJ* and, more generally, homogenized models, appears to be the only viable solution for the numerical simulation of porous surfaces, and their performance already appears to be suitable for applications in which a qualitative prediction of the main flow features trends is of interest.

References

[1] M Belloli, L Rosa, and A Zasso. Wind loads and vortex shedding analysis on the effects of the porosity on a high slender tower. *Journal of Wind Engineering and Industrial Aerodynamics*, 126:75–86, 2014.

[2] A Buljac, H Kozmar, S Pospíšil, and M Macháček. Aerodynamic and aeroelastic characteristics of typical bridge decks equipped with wind barriers at the windward bridge-deck edge. *Engineering Structures*, 137:310–322, 2017.

[3] G. Pomaranzi, N. Daniotti, P. Schito, L. Rosa, and A. Zasso. Experimental assessment of the effects of a porous double skin façade system on cladding loads. *Journal of Wind Engineering and Industrial Aerodynamics*, 196:104019, 2020.

[4] PJ Richards and M Robinson. Wind loads on porous structures. *Journal of Wind Engineering and Industrial Aerodynamics*, 83(1-3):455–465, 1999.

[5] SF Hoerner. Fluid-dynamic drag. *Hoerner fluid dynamics*, 1965.

[6] HJ Gerhardt and F Janser. Wind loads on wind permeable facades. *Journal of Wind Engineering and Industrial Aerodynamics*, 53(1-2):37–48, 1994.

[7] A Giannoulis, T Stathopoulos, D Briassoulis, and A Mistriotis. Wind loading on vertical panels with different permeabilities. *Journal of wind engineering and industrial aerodynamics*, 107:1–16, 2012.

[8] JK Raine and DC Stevenson. Wind protection by model fences in a simulated atmospheric boundary layer. *Journal of Wind Engineering and Industrial Aerodynamics*, 2(2):159–180, 1977.

[9] M Perera. Shelter behind two-dimensional solid and porous fences. *Journal of Wind Engineering and Industrial Aerodynamics*, 8(1-2):93–104, 1981.

[10] KG Ranga Raju, RJ Garde, SK Singh, and Singh N. Experimental study on characteristics of flow past porous fences. *Journal of Wind Engineering and Industrial Aerodynamics*, 29:155–163, 1988.

[11] AJG Papesch. Wind tunnel test to optimize barrier spacing and porosity to reduce wind damage in horticultural shelter systems. *Journal of Wind Engineering and Industrial Aerodynamics*, 44(1-3):2631–2642, 1992.

[12] IP Castro. Wake characteristics of two-dimensional perforated plates normal to an air-stream. *Journal of Fluid Mechanics*, 46:599–609, 1971.

[13] SJ Lee and BK Hyoung. Laboratory measurements of velocity and turbulence field behind porous fences. *Journal of Wind Engineering and Industrial Aerodynamics*, 80:311–326, 1999.

[14] YL Lo, YT Wu, CL Fu, and YC Yu. Wind load reduction effects on inner buildings by exterior porous façades. *Building and Environment*, 183:107148, 2020.

[15] B Blocken. 50 years of computational wind engineering: past, present and future. *Journal of Wind Engineering and Industrial Aerodynamics*, 129:69–102, 2014.

[16] PN Okolo, K Zhao, J Kennedy, and GJ Bennett. Numerical assessment of flow control capabilities of three dimensional woven wire mesh screens. *European Journal of Mechanics-B/Fluids*, 76:259–271, 2019.

[17] M Teitel. Using computational fluid dynamics simulations to determine pressure drops on woven screens. *Biosystems engineering*, 105(2):172–179, 2010.

[18] K Anirudh and S Dhinakaran. On the onset of vortex shedding past a two-dimensional porous square cylinder. *Journal of Wind Engineering and Industrial Aerodynamics*, 179:200–214, 2018.

[19] H Naito and K Fukagata. Numerical simulation of flow around a circular cylinder having porous surface. *Physics of Fluids*, 24:117102, 2012.

[20] MS Valipour, S Rashidi, M Bovand, and R Masoodi. Numerical modeling of flow around and through a porous cylinder with diamond cross section. *European Journal of Mechanics - B/Fluids*, 46:74–81, 2014.

[21] P Yu, Y Zeng, TS Lee, HX Bai, and HT Low. Wake structure for flow past and through a porous square cylinder. *International Journal of Heat and Fluid Flow*, 31:141–153, 2010.

[22] P Yu, Y Zeng, TS Lee, XB Chen, and HT Low. Steady flow around and through a permeable circular cylinder. *Computers & Fluids*, 42(1):1–12, 2011.

[23] P Yu, Y Zeng, TS Lee, XB Chen, and HT Low. Numerical simulation on steady flow around and through a porous sphere. *International journal of heat and fluid flow*, 36:142–152, 2012.

[24] VG Guerra, R BeÁttega, JAS Gonceálves, and JR Coury. Pressure drop and liquid distribution in a venturi scrubber: experimental data and cfd simulation. *Industrial & Engineering Chemistry Research*, 51(23):8049–8060, 2012.

[25] M Teitel, D Dvorkin, Y Haim, J Tanny, and I Seginer. Comparison of measured and simulated flow through screens: Effects of screen inclination and porosity. *Biosystems engineering*, 104(3):404–416, 2009.

[26] V Vassiliev, S Irmisch, M Claridge, and DP Richardson. Experimental and numerical investigation of the impact of swirl on the performance of industrial gas turbines exhaust diffusers. In *Turbo Expo: Power for Land, Sea, and Air*, volume 36894, pages 19–29, 2003.

[27] F Moukalled, L Mangani, and M Darwish. *The finite volume method in computational fluid dynamics*, volume 6. Springer, 2016.

[28] FR Menter. Influence of freestream values on k-omega turbulence model predictions. *AIAA journal*, 30(6):1657–1659, 1992.

[29] J Smagorinsky. General circulation experiments with the primitive equations: I. the basic experiment. *Monthly weather review*, 91(3):99–164, 1963.

[30] T-H Shih, WW Liou, A Shabbir, Z Yang, and J Zhu. A new k-epsilon eddy viscosity model for high reynolds number turbulent flows: Model development and validation. Technical report, 1994.

[31] T Maruyama. Large eddy simulation of turbulent flow around a windbreak. *Journal of Wind Engineering and Industrial Aerodynamics*, 96:1998–2006, 2008.

[32] C Ooi, PH Chiu, V Raghavan, S Wan, and HJ Poh. Porous media representation of louvers in building simulations for natural ventilation. *Journal of Building Performance Simulation*, 12(4):494–503, 2019.

[33] A Feichtner, E Mackay, G Tabor, PR Thies, and L Johanning. Comparison of macro-scale porosity implementations for cfd modelling of wave interaction with thin porous structures. *Journal of Marine Science and Engineering*, 9(2):150, 2021.

[34] J Rubinstein and S Torquato. Flow in random porous media: mathematical formulation, variational principles, and rigorous bounds. *Journal of Fluid Mechanics*, 206:25–46, 1989.

[35] D Allori, G Bartoli, and C Mannini. Wind tunnel tests on macro-porous structural elements: A scaling procedure. *Journal of Wind Engineering and Industrial Aerodynamics*, 123:291–299, 2013.

[36] B Eckert and F Pfluger. The resistance coefficient of commercial round wire grids. 1942.

[37] GB Schubauer, WG Spangenberg, and PS Klebanoff. Aeodynamic characteristics of damping screens. Technical report, NATIONAL AERONAUTICS AND SPACE ADMINISTRATION WASHINGTON DC, 1950.

[38] L Prandtl. Attaining a steady air stream in wind tunnels. 1933.

[39] HL Dryden and GB Schubauer. The use of damping screens for the reduction of wind-tunnel turbulence. *Journal of the Aeronautical Sciences*, 14(4):221–228, 1947.

[40] GI Taylor, GK Batchelor, HL Dryden, and GB Schubauer. The effect of wire gauze on small disturbances in a uniform stream. *The Quarterly Journal of Mechanics and Applied Mathematics*, 2(1):1–29, 1949.

[41] AR Collar. The effect of a gauze on the velocity distribution in a uniform duct. r. & m. no. 1867. *British ARC*, 1939.

[42] KG Ranga Raju, RJ Garde, SK Singh, and N Singh. Experimental study on characteristics of flow past porous fences. *Journal of Wind Engineering and Industrial Aerodynamics*, 29(1-3):155–163, 1988.

[43] FM Fang and DY Wang. On the flow around a vertical porous fence. *Journal of wind engineering and industrial aerodynamics*, 67:415–424, 1997.

[44] F Cheli, F Ripamonti, E Sabbioni, and G Tomasini. Wind tunnel tests on heavy road vehicles: cross wind induced loads—part 2. *Journal of Wind Engineering and Industrial Aerodynamics*, 99(10):1011–1024, 2011.

[45] CR Chu, CY Chang, CJ Huang, TR Wu, CY Wang, and MY Liu. Windbreak protection for road vehicles against crosswind. *Journal of Wind Engineering and Industrial Aerodynamics*, 116:61–69, 2013.

[46] KK Bofah and KG Al-Hinai. Field tests of porous fences in the regime of sand-laden wind. *Journal of Wind Engineering and Industrial Aerodynamics*, 23:309–319, 1986.

[47] L Bruno, D Fransos, and AL Giudice. Solid barriers for windblown sand mitigation: Aerodynamic behavior and conceptual design guidelines. *Journal of Wind Engineering and Industrial Aerodynamics*, 173:79–90, 2018.

[48] CW Park and SJ Lee. Experimental study on surface pressure and flow structure around a triangular prism located behind a porous fence. *Journal of wind engineering and industrial aerodynamics*, 91(1-2):165–184, 2003.

[49] H Kozmar, L Procino, A Borsani, and G Bartoli. Optimizing height and porosity of roadway wind barriers for viaducts and bridges. *Engineering Structures*, 81:49–61, 2014.

[50] P Price. Suppression of the fluid-induced vibration of circular cylinders. *Journal of the Engineering Mechanics Division*, 82(3):1030–1, 1956.

[51] DE Walshe and LR Wooton. Preventing wind-induced oscillations of structures of circular section. *Proceedings of the Institution of Civil Engineers*, 47(1):1–24, 1970.

[52] RAM Galbraith. Aspects of the flow in the immediate vicinity of a porous shroud. *Journal of Wind Engineering and Industrial Aerodynamics*, 8(3):251–258, 1981.

[53] HY Wong and A Kokkalis. A comparative study of three aerodynamic devices for suppressing vortex-induced oscillation. *Journal of Wind Engineering and Industrial Aerodynamics*, 10(1):21–29, 1982.

[54] G Pomaranzi, N Daniotti, P Schito, L Rosa, and A Zasso. Experimental assessment of the effects of a porous double skin façade system on cladding loads. *Journal of Wind Engineering and Industrial Aerodynamics*, 196:104019, 2020.

[55] G Hu, S Hassanli, KCS Kwok, and KT Tse. Wind-induced responses of a tall building with a double-skin façade system. *Journal of Wind Engineering and Industrial Aerodynamics*, 168:91–100, 2017.

[56] AFG Jacobs. The normal-force coefficient of a thin closed fence. *Boundary-layer meteorology*, 32(4):329–335, 1985.

[57] FH Kemper and M Feldmann. Wind load assumptions for permeable cladding elements considering the installation context. *Journal of Wind Engineering and Industrial Aerodynamics*, 184:277–288, 2019.

[58] G Ehrhardt. Flow measurements for wire gauzes. *Int. Chem. Eng*, 23(3):455–465, 1983.

[59] C Chen. *Dispersion and coalescence in static mixers.* Technical University of Nova Scotia, 1997.

[60] F Azizi and AM Al Taweel. Hydrodynamics of liquid flow through screens and screen-type static mixers. *Chemical engineering communications*, 198(5):726–742, 2011.

[61] D Sturge, D Sobotta, R Howell, A While, and J Lou. A hybrid actuator disc–full rotor cfd methodology for modelling the effects of wind turbine wake interactions on performance. *Renewable energy*, 80:525–537, 2015.

[62] D Cabezón, E Migoya, and A Crespo. Comparison of turbulence models for the computational fluid dynamics simulation of wind turbine wakes in the atmospheric boundary layer. *Wind Energy*, 14(7):909–921, 2011.

[63] RH Shaw and U Schumann. Large-eddy simulation of turbulent flow above and within a forest. *Boundary-Layer Meteorology*, 61(1):47–64, 1992.

[64] B Dalpé and C Masson. Numerical study of fully developed turbulent flow within and above a dense forest. *Wind Energy: An International Journal for Progress and Applications in Wind Power Conversion Technology*, 11(5):503–515, 2008.

[65] SJ Lee and HC Lim. A numerical study on flow around a triangular prism located behind a porous fence. *Fluid dynamics research*, 28(3):209, 2001.

[66] LM Huang, HC Chan, and JT Lee. A numerical study on flow around nonuniform porous fences. *Journal of Applied Mathematics*, 2012, 2012.

[67] K Kleissl and CT Georgakis. Aerodynamic control of bridge cables through shape modification: A preliminary study. *Journal of Wind Engineering and Industrial Aerodynamics*, 27:1006–1020, 2011.

[68] M Fang, F and DY Wang. On the flow around a vertical porous fence. *Journal of Wind Engineering and Industrial Aerodynamics*, 67-68:415–424, 1997.

[69] TR Alridge, BS Piper, and JCR Hunt. The drag coefficient of finite-aspect-ratio perforated circular cylinders. *Journal of Wind Engineering and Industrial Aerodynamics*, 3:251–257, 1978.

[70] RA Galbraith. Flow pattern around a shrouded cylinder at $re = 5\text{x}10^3$. *Journal of Wind Engineering and Industrial Aerodynamics*, 6:227–242, 1980.

[71] RA Galbraith. Aspects of the flow in the immediate vicinity of a porous shroud. *Journal of Wind Engineering and Industrial Aerodynamics*, 8:251–258, 1981.

[72] T Durhasan, MM Aksoy, E. Pinar, GM Ozkanc, H Akilli, and B Sahin. Vortex street suppression of a circular cylinder using perforated semi-circular fairing in shallow water. *Journal of Wind Engineering and Industrial Aerodynamics*, 79:101–110, 2016.

[73] T Durhasan, E Pinar, GM Ozkanc, H Akilli, and B Sahin. The effect of shroud on vortex shedding mechanism of cylinder. *Journal of Wind Engineering and Industrial Aerodynamics*, 84:51–61, 2019.

[74] MP Soberaa, CR Kleijn, and HEA Van den Akker. Subcritical flow past a circular cylinder surrounded by a porous layer. *Physics of Fluids*, 18:038106, 2006.

[75] CH Bruneau and I Mortazavi. Passive control of the flow around a square cylinder using porous media. *Numerical Methods in Fluids*, 46:415–433, 2004.

[76] S Bhattacharyya and AK Singh. Reduction in drag and vortex shedding frequency through porous sheath around a circular cylinder. *Numerical Methods in Fluids*, 65:683–698, 2011.

[77] KEG Wieghardt. On the resistance of screens. *The Aeronautical Quarterly*, 4(2):186–192, 1953.

[78] GI Taylor. The aerodynamics of porous sheets. *Aeronautical Reseach Council, Reports and Memoranda*, 2237:163–176, 1944.

[79] WJD Annand. The resistance to air flow of wire gauzes. *The Aeronautical Journal*, 57(507):141–146, 1953.

[80] F Azizi. On the pressure drop of fluids through woven screen meshes. *Chemical Engineering Science*, 207:464–478, 2019.

[81] IE Idelchik. Handbook of hydraulic resistance. *Washington*, 1986.

[82] RD Blevins. Applied fluid dynamics handbook. *New York, Van Nostrand Reinhold Co., 1984, 568 p.*, 1984.

[83] DS Miller. Internal flow systems. Technical report, 1978.

[84] JJ Janse van Rensburg. *Advanced modelling of porous screens in aerodynamic diffusers using variable resistance factors*. PhD thesis, 2014.

[85] LFG Simmons. Measurements of the aerodynamics forces acting on porous screens. *Aeronautical research Council, Reports and Memoranda*, 2276:1–20, 1945.

[86] SF Hoerner. Fluid-dynamic drag. theoretical, experimental and statistical information, 1958.

[87] J Groth and AV Johansson. Turbulence reduction by screens. *Journal of Fluid Mechanics*, 197:139–155, 1988.

[88] RS Wakeland and RM Keolian. Measurements of resistance of individual square-mesh screens to oscillating flow at low and intermediate reynolds numbers. *J. Fluids Eng.*, 125(5):851–862, 2003.

[89] E Brundrett. Prediction of pressure drop for incompressible flow through screens. *Journal of Fluids Engineering*, 115(2):239–242, 1993.

[90] Jens HM Kurian, TF. Grid-generated turbulence revisited. *Fluid dynamics research*, 41(2):021403, 2009.

[91] BJ Bailey, JI Montero, AP Parra, JPR, E Baeza, and R Kamaruddin. Airflow resistance of greenhouse ventilators with and without insect screens. *Biosystems Engineering*, 86(2):217–229, 2003.

[92] PE Roach. The generation of nearly isotropic turbulence by means of grids. *International Journal of Heat and Fluid Flow*, 8(2):82–92, 1987.

[93] L Bruno, MV Salvetti, and F Ricciardelli. Benchmark on the aerodynamics of a rectangular 5: 1 cylinder: an overview after the first four years of activity. *Journal of Wind Engineering and Industrial Aerodynamics*, 126:87–106, 2014.

[94] GB Schubauer, WG Spangenberg, and PS Klebanoff. Aerodynamic characteristics of damping screens. 1950.

[95] GM Richardson. A permeable windbreak: its micro-environment and its effect on structural loads. *Journal of agricultural engineering research*, 38(1):65–76, 1987.

[96] EM Laws and JL Livesey. Flow through screens. *Annual Review of Fluid Mechanics*, 10(1):247–266, 1978.

[97] K Kosutova, T van Hooff, C Vanderwel, B Blocken, and J Hensen. Cross-ventilation in a generic isolated building equipped with louvers: Wind-tunnel experiments and cfd simulations. *Building and Environment*, 154:263–280, 2019.

[98] AR Packwood. Flow through porous fences in thick boundary layers: comparisons between laboratory and numerical experiments. *Journal of Wind Engineering and Industrial Aerodynamics*, 88(1):75–90, 2000.

[99] CS Watters and C Masson. Recent advances in modeling of wind turbine wake vortical structure using a differential actuator disk theory. In *Journal of Physics: Conference Series*, volume 75, page 012037, 2007.

[100] PE Réthoré and NN Sørensen. A discrete force allocation algorithm for modelling wind turbines in computational fluid dynamics. *Wind Energy*, 15(7):915–926, 2012.

[101] PE Réthoré, P van der Laan, N Troldborg, F Zahle, and NN Sørensen. Verification and validation of an actuator disc model. *Wind Energy*, 17(6):919–937, 2014.

[102] A Feichtner, E Mackay, G Tabor, PR Thies, L Johanning, and DZ Ning. Using a porous-media approach for cfd modelling of wave interaction with thin perforated structures. *Journal of Ocean Engineering and Marine Energy*, 7(1):1–23, 2021.

[103] YC Li, Y Liu, and B Teng. Porous effect parameter of thin permeable plates. *Coastal Engineering Journal*, 48(04):309–336, 2006.

[104] M del Jesus, JL Lara, and IJ Losada. Three-dimensional interaction of waves and porous coastal structures: Part i: Numerical model formulation. *Coastal Engineering*, 64:57–72, 2012.

[105] L Bruno, MV Salvetti, and F Ricciardelli. Benchmark on the aerodynamics of a rectangular 5: 1 cylinder: an overview after the first four years

of activity. *Journal of Wind Engineering and Industrial Aerodynamics*, 126:87–106, 2014.

[106] A Mariotti, L Siconolfi, and MV Salvetti. Stochastic sensitivity analysis of large-eddy simulation predictions of the flow around a 5: 1 rectangular cylinder. *European Journal of Mechanics-B/Fluids*, 62:149–165, 2017.

[107] C Mannini, AM Marra, L Pigolotti, and G Bartoli. The effects of free-stream turbulence and angle of attack on the aerodynamics of a cylinder with rectangular 5: 1 cross section. *Journal of Wind Engineering and Industrial Aerodynamics*, 161:42–58, 2017.

[108] M Ricci, L Patruno, S de Miranda, and F Ubertini. Flow field around a 5:1 rectangular cylinder using les: Influence of inflow turbulence conditions, spanwise domain size and their interaction. *Computers and Fluids*, 149:181–193, 2017.

[109] B Wu, SP Li, K Li, and LL Zhang. Numerical and experimental studies on the aerodynamics of a 5: 1 rectangular cylinder at angles of attack. *Journal of Wind Engineering and Industrial Aerodynamics*, 199:104097, 2020.

[110] A Mariotti, MV Salvetti, PS Omrani, and JAS Witteveen. Stochastic analysis of the impact of freestream conditions on the aerodynamics of a rectangular 5: 1 cylinder. *Computers & Fluids*, 136:170–192, 2016.

[111] B Rocchio, A Mariotti, and MV Salvetti. Flow around a 5: 1 rectangular cylinder: Effects of upstream-edge rounding. *Journal of Wind Engineering and Industrial Aerodynamics*, 204:104237, 2020.

[112] RA Pinker and MV Herbert. Pressure loss associated with compressible flow through square-mesh wire gauzes. *Journal of Mechanical Engineering Science*, 9(1):11–23, 1967.

[113] M Xu, Luca P, YL Lo, and S de Miranda. On the use of the pressure jump approach for the simulation of separated external flows around porous structures: A forward facing step. *Journal of Wind Engineering and Industrial Aerodynamics*, 207:104377, 2020.

[114] FR Menter, M Kuntz, and R Langtry. Ten years of industrial experience with the sst turbulence model. *Turbulence, heat and mass transfer*, 4(1):625–632, 2003.

[115] D Sun, JS Owen, and NG Wright. Application of the k–ω turbulence model for a wind-induced vibration study of 2d bluff bodies. *Journal of Wind Engineering and Industrial Aerodynamics*, 97(2):77–87, 2009.

[116] C Mannini, A Šoda, and G Schewe. Unsteady rans modelling of flow past a rectangular cylinder: Investigation of reynolds number effects. *Computers & fluids*, 39(9):1609–1624, 2010.

[117] L Patruno, M Ricci, S De Miranda, and F Ubertini. Numerical simulation of a 5: 1 rectangular cylinder at non-null angles of attack. *Journal of Wind Engineering and Industrial Aerodynamics*, 151:146–157, 2016.

[118] FR Menter. Two-equation eddy-viscosity turbulence models for engineering applications. *AIAA journal*, 32(8):1598–1605, 1994.

[119] TH Shih. *A realizable Reynolds stress algebraic equation model*, volume 105993. Lewis Research Center, Institute for Computational Mechanics in Propulsion, 1993.

[120] M Xu, Luca P, YL Lo, S de Miranda, and F Ubertini. On the numerical simulation of perforated bluff-bodies: a cfd study on a hollow porous 5:1 rectangular cylinder. *Submitted*, 2020.

[121] A Yoshizawa. Statistical theory for compressible turbulent shear flows, with the application to subgrid modeling. *The Physics of fluids*, 29(7):2152–2164, 1986.

[122] H Kozmar and ZB Klaić. Wind effects on man-made structures in a world with a changing climate. In *National Security and Human Health Implications of Climate Change*, pages 219–228. Springer, 2012.

[123] N Chen, YL Li, B Wang, Y Su, and HY Xiang. Effects of wind barrier on the safety of vehicles driven on bridges. *Journal of Wind Engineering and Industrial Aerodynamics*, 143:113–127, 2015.

[124] A Buljac, H Kozmar, S Pospíšil, and M Macháček. Flutter and galloping of cable-supported bridges with porous wind barriers. *Journal of Wind Engineering and Industrial Aerodynamics*, 171:304–318, 2017.

[125] A Buljac, H Kozmar, S Pospíšil, Mi Macháček, and S Kuznetsov. Effects of wind-barrier layout and wind turbulence on aerodynamic stability of cable-supported bridges. *Journal of Bridge Engineering*, 25(12):04020102, 2020.

[126] IP Castro. Wake characteristics of two-dimensional perforated plates normal to an air-stream. *Journal of Fluid Mechanics*, 46(3):599–609, 1971.

[127] M Telenta, M Batista, ME Biancolini, I Prebil, and J Duhovnik. Parametric numerical study of wind barrier shelter. *Wind and Structures*, 20(1):75–93, 2015.

[128] ZB Dong, WY Luo, GQ Qian, and HT Wang. A wind tunnel simulation of the mean velocity fields behind upright porous fences. *Agricultural and Forest Meteorology*, 146(1-2):82–93, 2007.

[129] SJ Lee and HB Kim. Laboratory measurements of velocity and turbulence field behind porous fences. *Journal of Wind Engineering and Industrial Aerodynamics*, 80(3):311–326, 1999.

[130] A Larsen and JH Walther. Aeroelastic analysis of bridge girder sections based on discrete vortex simulations. *Journal of Wind Engineering and Industrial Aerodynamics*, 67:253–265, 1997.

[131] A Larsen and JH Walther. Discrete vortex simulation of flow around five generic bridge deck sections. *Journal of Wind Engineering and Industrial Aerodynamics*, 77:591–602, 1998.

[132] T Maruyama. Large eddy simulation of turbulent flow around a windbreak. *Journal of wind engineering and industrial aerodynamics*, 96(10-11):1998–2006, 2008.

[133] M Telenta, J Duhovnik, F Kosel, and V Šajn. Numerical and experimental study of the flow through a geometrically accurate porous wind barrier model. *Journal of Wind Engineering and Industrial Aerodynamics*, 124:99–108, 2014.

[134] MC Montoya, F Nieto, S Hernández, I Kusano, AJ Álvarez, and JÁ Jurado. Cfd-based aeroelastic characterization of streamlined bridge deck cross-sections subject to shape modifications using surrogate models. *Journal of Wind Engineering and Industrial Aerodynamics*, 177:405–428, 2018.

[135] G Pomaranzi, O Bistoni, P Schito, and A Zasso. Numerical modelling of three-dimensional screens, treated as porous media. *Wind and Structures*, 33(5):409–422, 2021.

List of Figures

List of Tables